A dark matter search with DarkSide-50

Guangyong Koh

A Dissertation

Presented to the Faculty

of Princeton University

in Candidacy for the Degree

of Doctor of Philosophy

Recommended for Acceptance

by the Department of

Physics

Adviser: Peter D. Meyers

June 2018

Abstract

DarkSide-50 is a direct detection experiment searching for WIMP dark matter operated at Laboratori Nazionali del Gran Sasso, consisting of a dual-phase argon time projection chamber nested within an active neutron veto. The core detector is filled with a target of argon extracted from underground sources that is depleted in radioactive Argon-39.

This thesis details the blind analysis of 532.4 live-days of data acquired between Aug 2015 and Oct 2017. Particular attention will be paid to the analysis of the electron recoil background, which includes: estimating the rates of radioisotope decay that are responsible; modeling the scintillation response of electron recoil events in liquid argon; and developing a cut utilizing pulse-shape discrimination to control the electron recoil background.

We observe a background- and signal- free result, and report a 90% C.L. upper limit on the spin-independent WIMP-nucleon scattering cross-section of $1.1 \times 10^{-44}\,\mathrm{cm}^2$ ($3.8 \times 10^{-44}\,\mathrm{cm}^2$, $3.4 \times 10^{-43}\,\mathrm{cm}^2$) for a WIMP mass of $100\,\mathrm{GeV}/c^2$ ($1\,\mathrm{TeV}/c^2$, $10\,\mathrm{TeV}/c^2$).

Acknowledgements

The work detailed in this thesis is the product of a years-long (and ongoing) effort undertaken by the DarkSide collaboration. The list of collaborators is long, so I will not attempt to reproduce it here for fear of missing someone; readers are directed instead to the DarkSide-50 publications for the exhaustive list. DarkSide-50 was a remarkably stable instrument, both in terms of hardware and data quality, and all members of the collaboration, from the engineering to the analysis teams, deserve credit for the results presented here.

DarkSide-50 was supported by the U.S. National Science Foundation, the Italian Istituto Nazionale di Fisica Nucleare, the U.S. Department of Energy, the Russian Science Foundation, the Polish NCN, the Foundation for Polish Science, the French Institut National de Physique Nucléaire et de Physique des Particules, the UnivEarthS Labex program of Sorbonne Paris Cité, and the São Paulo Research Foundation. Science funding is important, and taxpayers from these territories made this work possible.

For the past 7 years, my adviser, Peter Meyers, has been an untiring source of guidance on analysis minutiae, organization, and professional development. His humility and demand for rigor has made me a better scientist. He is a compassionate manager and an utterly dependable colleague, and I am fortunate to have worked both for and with him.

Though I worked less closely with Frank Calaprice and Cristiano Galbiati than with Peter, they are fonts of knowledge with impeccable scientific intuition, whose feedback would often lead me down the right research path even if I wouldn't know it at the time.

Masayuki Wada and Graham Giovanetti are first-rate researchers and teachers, who were always game to engage with my questions, and sometimes rambling dis-

cussions, about the detector, the analysis, ROOT, or physics in general. They both deserve faculty jobs!

Xin Xiang played a crucial role in the development of the electron recoil background model described in this thesis, particularly for his work on modeling the Cherenkov response in the detector. The hours spent developing a model are often overlooked for the final result, and I'd like to draw attention to the painstaking work Xin put into refining the optical model, producing countless variations of the PMT geometry, and generating our massive Monte Carlo event set, in case he neglects to do so in his thesis.

Tessa Johnson and Masayuki Wada took on the thankless task of processing the raw data for analysis. Having this in their dependable hands took an immense amount of tedium off the rest of the analysis team. For that Tessa and Masa have my gratitude.

The broader analysis team—Alissa, Andrew, Brianne, Chengliang, Chris, Davide, Erin, Francesco, Hao, Luca, Maximo, Paolo, Parth, Shawn, Xinran, under the leadership of Jeff Martoff, Emilija Pantic, and Stefano Davini—was a group of intelligent and committed individuals. My work benefitted immensely from their challenging of my assumptions, and the ideas tossed out at our weekly analysis meetings.

Luca Grandi and Richard Saldanha were critical to my early grad school education. I can think of few better ways to have learned the ropes of DarkSide-50 than by working with them on the detector assembly and early data analysis.

The Princeton group's administrators, Helen Ju and Kim Dawidowski, are unsung heroes whose job was to help us do ours. They did so with a level of care and consideration for us that went above and beyond.

Yura Suvorov, Federico Ferraro, Luca Pagani, and Laura Marini were welcoming hosts during my various stays in Assergi. Assergi is a beautiful place, but it has its downsides[1]—thanks for your warm company!

One does not get to meet many new people in Princeton, so it was fortunate that I started grad school with an outstanding group of individuals. Through prelims and everything else after, these were the people I could count on for hijinks[2] and serious conversation alike. Hugs to Anne, Anthony, Ed, Kenan, Max, Peace, Sara, Shawn, and Vuk.

Apologies to my friends back home and elsewhere, who I do not catch up with as often as I should. Thanks for putting up with my sustained absence. Thanks especially to Melvin and Junming, who I can always count on in a pinch.

I met Katie Spaulding in my first year of grad school, and she has been a constant companion throughout this journey. Having her to share my good and bad moments with makes them all just a little bit better (if not a lot better). I shudder to think how the experience would have been different (read: worse) without her presence.

All my life, my family has been an unending source of love and support. My achievements are built on that foundation. I look forward to our Friday phone calls, and to being able to visit more often.

[1] *e.g.*, only four restaurants, of which I heartily recommend Franchino's.

[2] Including, but not limited to: hitting up DBar; improving at trivia over the years; watching or speculating about Game of Thrones; soccer or summer softball (Go Team Pup N Suds and Big Bangers!); pig roasts, crawfish boils, and other food-related activities.

To my parents.

Contents

Abstract iii

Acknowledgements iv

List of Tables xii

List of Figures xiii

1 Dark matter **1**

1.1 Evidence for the existence of dark matter 1

1.2 Weakly interacting massive particles 2

1.3 Direct detection and the WIMP-nucleon scattering cross-section . . . 3

2 DarkSide-50 **6**

2.1 Outer detectors 6

2.1.1 Data acquisition and relevant reconstructed variables 8

2.2 Liquid argon time projection chamber 9

2.2.1 Event signals 9

2.2.2 Data acquisition and relevant reconstructed variables 11

2.2.3 Recoil energy to S1 light yield calibration 13

2.2.4 Corrections to S1 and S2 14

3 Background overview **15**

3.1 Main backgrounds 15

3.1.1 Neutron background 15

3.1.2 Surface background 16
3.1.3 Electron recoil background 17
3.2 Notable background-producing radioisotopes 18
3.2.1 Uranium-238 19
3.2.2 Uranium-235 21
3.2.3 Thorium-232 21
3.2.4 Potassium-40 21
3.2.5 Cobalt-60 22
3.2.6 Krypton-85 22
3.2.7 Argon-39 22
3.2.8 Argon-37 22
3.2.9 Radon daughters 22
3.3 Estimating radioisotope activities 23
3.3.1 Combined S1 and S2 energy variable 23
3.3.2 Method 24
3.3.3 Notes 25
3.3.4 Estimating radioisotope activities in the PMTs 29
3.3.5 Establishing upper and lower limits 30
3.3.6 Discussion 32
3.3.7 70d UAr analysis rates 34

4 Cut summary **39**

4.1 Event quality cuts 39
4.1.1 Number of channels 39
4.1.2 Baseline 39
4.1.3 S1 saturation 40
4.1.4 Veto present 40
4.1.5 Trigger type 40

4.2 Basic event topology cuts 41
4.2.1 Livetime 41
4.2.2 Number of pulses 41
4.2.3 Start time of S1 42
4.2.4 S2 F90 42
4.2.5 Minimum corrected S2/S1 42
4.3 Neutron background cuts 43
4.3.1 Prompt LSV signal 43
4.3.2 Delayed LSV signal 44
4.3.3 Pre-prompt LSV signal 44
4.3.4 Muon signal 45
4.3.5 Delayed neutrons from cosmogenic activation 45
4.4 Fiducialization 45
4.4.1 Drift time 45
4.4.2 Uncorrected S2 46
4.4.3 Radius 46
4.5 Surface background cuts 46
4.5.1 Long S1 tail 46
4.5.2 S1 top bottom asymmetry 47
4.5.3 Early S2 pulse shape 48
4.6 Electron recoil background cuts 48
4.6.1 Maximum corrected S2/S1 49
4.6.2 S1 prompt maximum fraction 49
4.6.3 Negative log-likelihood of S1 light distribution 50
4.6.4 WIMP search region 50
4.7 Background rejection 50
4.7.1 Neutron background 50

4.7.2 Electron recoil background 50
4.7.3 Surface background 53

5 Modeling electron recoil F90 **54**

5.1 Method overview 54
5.2 Simulated events 55
5.3 Clustering simulated event deposits 56
5.3.1 Development and implementation 57
5.4 Implementing a multiple-S2 resolution, and reproducing analogues of data variables 58
5.4.1 Developing a multiple-S2 resolution analogue 60
5.5 Obtaining the amount of cluster energy going into scintillation 61
5.6 Obtaining S1 from the scintillation energy 63
5.7 Smearing S1 65
5.8 Looking up F90 65
5.8.1 Selecting AAr data for use as an F90 reference 65
5.8.2 F90 model for low S1 scatters 66
5.8.3 Spectral dependence of F90 69
5.9 Constructing event S1 and F90 74
5.10 Combining with the Cherenkov model 74
5.10.1 S1 light distribution 74
5.11 Model systematics 76
5.12 Validation against 70d UAr data 77
5.12.1 Single-scatter events 77
5.12.2 Three-pulse events 79

6 The blind analysis **80**

6.1 Implementation of blinding 80

6.2 Sequential unmasking of data for testing 82
6.2.1 Events with a veto prompt signal 82
6.2.2 Non-single-scatter events 85
6.2.3 Events with high F90 85
6.3 Background predictions 87
6.3.1 Radiogenic neutron background 87
6.3.2 Cosmogenic neutron background 89
6.3.3 Surface backgrounds 89
6.3.4 Electron recoil background 90

7 Finalizing the WIMP search region **91**
7.1 Required simulation statistics 91
7.1.1 A note on previous analysis procedures 91
7.1.2 Implications of lower simulation statistics 91
7.2 WIMP box setting procedure 93
7.2.1 Shaping the WIMP search region at low S1 93
7.2.2 Positioning the contour 93
7.3 Discussion 94
7.3.1 Contour shapes 94
7.3.2 Impact of low simulation statistics in the WIMP search region 95

8 Cut acceptances **97**
8.1 Trigger type 97
8.2 Number of channels 98
8.3 Baseline 98
8.4 Livetime 99
8.5 Veto cuts 99
8.5.1 Veto present 99

8.5.2 Muon signal 99
8.5.3 Delayed neutrons from cosmogenic activation 100
8.5.4 Prompt LSV signal 100
8.5.5 Delayed LSV signal 102
8.5.6 Pre-prompt LSV signal 102
8.6 S1 range 103
8.7 Drift time 103
8.8 Number of pulses 103
8.9 Start time of S1 106
8.10 S1 saturation 106
8.11 Uncorrected S2 107
8.12 S2 cuts 108
8.12.1 S2 F90 109
8.12.2 Minimum corrected S2/S1 109
8.12.3 Maximum corrected S2/S1 110
8.12.4 Early S2 pulse shape 110
8.13 S1 prompt maximum fraction 112
8.14 S1 top bottom asymmetry 113
8.15 Long S1 tail 114
8.16 Radial fiducialization 115
8.17 Negative log-likelihood of S1 light distribution 115
8.18 Summary 116
8.19 Selecting neutrons from calibration data 116
8.19.1 Prompt LSV signal 119
8.19.2 F90 119
8.20 70d UAr analysis WIMP box 119

9 Setting the limit on the WIMP-nucleon scattering cross-section 121

9.1 Method overview 121

9.2 Simulated WIMP masses 122

9.3 Differential WIMP-argon recoil rate 122

9.4 Generating scatter S1 and F90, and accounting for analysis cut acceptances 124

9.5 Obtaining a limit on the WIMP-nucleon scattering cross-section . . . 124

10 Results and conclusion 126

A Recoil energy and angle 128

Bibliography 131

List of Tables

3.1 Radioisotope activity in various cryostat components from materials assay. 28

3.2 Fractional distribution of radioisotope activities across the various PMT components. 29

3.3 Radioisotope activities in the PMTs obtained by a sequential fit. . . . 30

3.4 Comparison of PMT rates from energy spectrum fits against measured PMT rates. 32

3.5 Predicted box event counts in 500 d of UAr running. 36

3.6 70d UAr analysis radioisotope activities, obtained with the procedure described in Sec. 3.3.4. 37

3.7 Predicted box event counts in 70 d of UAr running. 38

4.1 Coefficients for a 9th degree polynomial fit of σ_{TBA} *vs.* S1. 48

4.2 Responses of various event sets to analysis cuts. 52

5.1 Values for parameters used in the ion-electron recombination probability function, Eqn. 5.6. 63

5.2 Predicted event counts in 500 d of UAr running using different variants of the ER F90 model. 77

6.1 Coefficients for the polynomial describing the F90 lower bound of the blinding region. 81

6.2 Event counts observed in the data, and predicted by the electron recoil background model, in various unblinded test regions. 87

6.3 Predicted backgrounds in the 530d UAr exposure, surviving all WIMP search analysis cuts. 90

7.1 Implications of available simulation statistics (relative to data) on the precision of a background prediction of 0.08 event. 92

7.2 WIMP-nucleon scattering cross-section limits (for 100 $\mathrm{GeV/c^2}$ WIMPs) set by WIMP boxes admitting various amounts of total electron recoil background, and drawn with various procedures. 96

8.1 Summary of cuts, and their respective impact on livetime and WIMP acceptance. 118

9.1 Constant inputs for modeling the differential WIMP-argon recoil rate. 122

List of Figures

1.1 Upper limits on the WIMP-nucleon scattering cross-section set by various noble liquid direct-detection experiments. 5

2.1 The DarkSide-50 detectors. 7

2.2 F90 *vs.* S1 of data acquired with and without a neutron calibration source deployed. 10

3.1 Simulated TPC energy spectrum from $^{238}U_{lower}$ in the PMT stem. . . 25

3.2 Output from the energy spectrum fitting. 26

3.3 Simulated energy spectrum in the TPC from radioisotope activity in the cryostat, each with a $1\,\sigma$ uncertainty added. 27

3.4 Fits of individual PMT decay chains against peaks unique to their respective spectra, to obtain upper limits on their activities. 33

3.5 Fit to obtain lower limits on various radioisotope activities in the PMTs. 34

3.6 Fits to obtain upper and lower limits on $^{238}U_{upper}$ and ^{235}U activity in the PMTs. 35

3.7 Observed and modeled S1 spectra of 530d UAr events. 37

4.1 S2/S1 *vs.* S1 of $^{241}Am^{13}C$ neutron source calibration events, with the minimum and maximum S2/S1 cuts overlaid. 43

4.2 The drift time dependent radial cut. 47

4.3 Estimating background rejection from analysis cuts using $^{241}Am^{13}C$ and 70d UAr events. 51

5.1 Flowchart depicting the broad steps of the empirical F90 model. . . . 55

5.2 Positions and times of energy deposits in simulations of a 10 keV photon started in the bulk of the liquid argon volume. 57

5.3 Cluster multiplicity and energies of simulated ^{60}Co events in the cryostat, with various clustering ranges. 59

5.4 Cluster energy of simulated ^{39}Ar events, with various clustering thresholds. 60

5.5 Modeling the pulse-finding algorithm's efficiency at resolving simulated events with two S2 pulses. 62

5.6 Observed and modeled pulse multiplicity of UAr events. 63

5.7 Uncorrected S1 spectra of ^{57}Co from source calibration data and simulations with different smearing parameters. 64

5.8 Light yield implemented in the electron recoil background model. . . 64

5.9 Effect of the S1 prompt maximum fraction cut, and drift time fiducialization, on AAr data events to be used as an F90 reference in the electron recoil background model. 67

5.10 F90 *vs.* S1 of AAr data events with minimal selection criteria, and the S1pmf cut (1 through 6 in Sec. 5.8.1). 68

5.11 F90 *vs.* S1 of AAr data events used as the model's F90 reference. . . 68

5.12 **Left:** Approximate AAr and 530d UAr energy spectra used in the toy simulation. **Right:** $F90_{mean}$ vs energy function used in the toy simulation. 71

5.13 Comparing F90 contours set by events in the UAr and AAr toy simulations. 72

5.14 Energies of the component scatters in simulated unresolved two-Compton-scatter events. 73
5.15 Comparing F90 contours set by toy simulations of two-Compton-scatter events. 75
5.16 Comparing the modeled and observed F90 profiles of single-sited electron recoil events in UAr. 78
5.17 Comparing the modeled and observed F90 profiles of two-sited electron recoil events in UAr. 79

6.1 The blinding region. 81
6.2 Charge *vs.* multiplicity of LSV cluster signals, from ^{241}Am^{13}C neutron source calibration events with and without a veto prompt signal. . . . 83
6.3 F90 *vs.* S1 of events with a veto prompt signal. 84
6.4 Testing in regions unblinded during the later stages of the blind analysis. 88

7.1 WIMP search regions for the 70d UAr and AAr analyses. 92
7.2 Drawing the WIMP search region using the electron recoil F90 model. 94
7.3 Variations of the WIMP search region. 95

8.1 Residual livetime after various cuts with relevant impact. 98
8.2 Example waveforms, summed over the top and bottom PMT arrays, for a bipolar noise event, and a normal scintillation + ionization event. 99
8.3 When events may occur relative to the 0.6 s window of the cut against delayed neutrons from cosmogenic activation. 101
8.4 WIMP acceptance of the number of pulses/single-scatter cut. 105
8.5 WIMP acceptance of the S1 start time cut. 106
8.6 WIMP acceptance of the S1 saturation cut. 107
8.7 WIMP acceptance of the minimum uncorrected S2 cut. 108

8.8 Efficiency of the xy-algorithm at reconstructing ^{241}AmBe nuclear recoil events. 108
8.9 Radial distribution of AAr and ^{241}AmBe NR events. 109
8.10 WIMP acceptance of the S2 F90 cut. 110
8.11 WIMP acceptance of the minimum corrected S2/S1cut. 111
8.12 WIMP acceptance of the maximum S2/S1 cut. 111
8.13 WIMP acceptance of the early S2 pulse shape cut. 112
8.14 WIMP acceptance of the S1prompt maximum fraction cut. 113
8.15 WIMP acceptance of the S1 top bottom asymmetry cut. 114
8.16 WIMP acceptance of the long S1 tail cut. 115
8.17 WIMP acceptance of the radial cut *vs.* S1. 116
8.18 WIMP acceptance of the S1 light distribution negative log-likelihood cut. 117
8.19 Combined WIMP acceptance of cuts, including that of the WIMP search region for the 530d UAr analysis ("F90 NR acceptance"). . . . 117
8.20 WIMP acceptance of the 70d UAr WIMP box, estimated on ^{241}AmBe nuclear recoil data. 120

10.1 F90 *vs.* S1 of events in 530d UAr data, after application of all analysis cuts. 126
10.2 Limit on the spin-independent WIMP-nucleon scattering cross-section, based on the result observed in the 530d UAr analysis. 127

Chapter 1

Dark matter

Dark matter refers to the various candidates for non-luminous matter in the universe whose presence has so far only been detected through their gravitational effects. The existence of *some* form of dark matter is supported by mounting evidence over many decades, dating back to the first half of the twentieth century; however, many of its detailed properties are still unknown. In this chapter, we discuss some of the evidence for the existence of dark matter, before turning our focus to Weakly Interacting Massive Particles (WIMPs) in particular as a dark matter candidate. We will also briefly review the state of the field of dark matter detection experiments.

1.1 Evidence for the existence of dark matter

Early evidence for the existence dark matter came from observations of the motion of luminous astrophysical objects via their redshift. In particular, these were found to be moving more quickly than if the gravitational force responsible was exerted only by other luminous bodies (whose masses were estimated via their mass to luminosity ratios). These observations included that of: 1) The motion of stars in the Milky Way [1]; 2) The motion of galaxies in the Coma cluster [2]; and 3) The rotational velocities of numerous galaxies [3]. The last of these studies has been done extensively,

and little more than Newtonian gravity ($v^2 \propto GM/r$) is required to appreciate the implications of the resultant galactic rotation curves. Since the rotational velocity was observed to be constant at large galactic radii instead of decreasing with the expected $1/\sqrt{r}$ relation, either the presence of a halo of dark matter, or modified Newtonian dynamics (MOND), is necessitated [4].

Separate astrophysical evidence came from the observed gravitational lensing of luminous bodies, in which apparent twins of the same object—*i.e.*, with the same redshift, luminosity, and spectra—were observed in proximity to each other [5, 6] without an intervening foreground object. Gravitational lensing observations played a role as well in more recent observations of the Bullet cluster (which is notably the result of two clusters merging). Here, the interstellar gas—which accounted for most of the cluster's baryonic mass—was compressed and heated in the merger process, emitting X-rays that gave an indication of its distribution. Notably, this mass distribution was drastically different from that inferred from the cluster's lensing effect on background objects, which showed that most of the clusters' mass had actually passed by each other without interaction. This was consistent with the presence of non-baryonic, weakly interacting dark matter [7].

Further evidence came from the study of anisotropies in the cosmic microwave background (CMB), which indicated the extent of density fluctuations in the photon-baryon fluid and the dark matter distribution at the epoch of recombination[1]. In particular, analysis of the CMB power spectrum by fitting with a ΛCDM cosmology (the "standard model" of Big Bang cosmology) predicted that dark matter accounts for ∼84% of the total mass in the universe (the baryon and dark matter densities are often parametrized as Ω_b and Ω_c, respectively) [8]. We note that the cosmological evidence places some constraints on the characteristics of dark matter: 1) It is non-baryonic instead of merely non-luminous; 2) It has to be non-relativistic to account

[1] "Recombination" here refers to that of electrons and protons, so this is the time of photon-baryon decoupling, *i.e.*, when the universe became transparent to photons

for the formation of large-scale structure as we observe it; and 3) It has to be stable to exist in both the early and present universe.

1.2 Weakly interacting massive particles

The evidence summarized in the previous section motivates a form of dark matter that is non-baryonic, weakly interacting, non-relativistic, and stable. In particular, this rules out all standard model particles—*e.g.*, neutrinos are relativistic, the W/Z bosons are unstable, *etc.* A class of dark matter candidates meeting these requirements is referred to as Weakly Interacting Massive Particles, or WIMPs; one posited example is the lightest supersymmetric particle (LSP), also referred to as the neutralino. In terms of theoretical expedience, WIMPs were a popular dark matter candidate because of the "WIMP miracle"—the fact that calculations making minimal assumptions beyond an interaction cross-section on the weak scale predicted a relic dark matter density consistent with observations. This made WIMP masses on the $\sim 100\,\mathrm{GeV}/c^2$ scale (comparable to that of the W and Z gauge bosons) interesting.

Practically, WIMPs also make attractive dark matter candidates because the signatures of their existence (apart from their already observed gravitational effects) can feasibly be probed by current scientific apparatus. Many WIMP-search experiments are presently underway, falling into three broad categories [9]:

1. **Telescopes seeking to observe signatures of WIMP annihilation or decay [10].** Assuming WIMPs are their own anti-particles (as the LSP is predicted to be), they can self-annihilate, producing standard model products such as γ-rays and neutrinos. Since this is expected to be a rare process, the focus is on regions where the WIMP density might be higher, such as the centers of planets, stars, or galaxies. One such experiment is IceCube, a neutrino telescope that is sensitive to energetic annihilation neutrinos from the Sun [11].

2. **Collider searches seeking to produce WIMPs [12].** The reverse of the annihilation process, *i.e.*, WIMP production from standard model inputs, can also occur. Since any resultant WIMPs would be invisible to detectors, the signature for this would be missing energy among the collision products. Probeable WIMP masses are limited by attainable collider energies; thus, current searches at the LHC are only sensitive to WIMP masses up to the TeV scale.

3. **Direct detection experiments seeking to observe WIMP interactions with standard model particles.** We review the general principles behind such experiments—of which DarkSide-50 is one example—, and the current state of the field, in the subsequent section.

1.3 Direct detection and the WIMP-nucleon scattering cross-section

Direct detection of dark matter is an active field of research, with experiments using target media such as sodium iodide and germanium crystals (DAMA/LIBRA [13] and SuperCDMS [14] respectively), silicon charge-coupled devices (DAMIC [15]), liquid xenon (LUX-ZEPLIN [16], Xenon [17], PandaX [18]), and of course, liquid argon (DEAP [19], DarkSide [20]). These experiments generally involve the instrumentation of a target volume of judiciously chosen material, and essentially waiting for a WIMP-nucleus scattering event to occur. Since these scatters are expected to be rare, the challenge for direct detection experiments is in understanding and containing the background (*i.e.*, scatters not involving WIMPs). Consequently, the targets are typically chosen to have some combination of radiopurity, scalability, and good background discrimination properties.

The observed rate of WIMP scattering is used to derive limits on the scattering cross-section as a function of WIMP mass by assuming some local WIMP flux and

WIMP-nucleon scattering model. The Standard Halo Model is typically used to derive the local WIMP flux. Briefly, the model consists of a dark matter halo with some local mass density, and WIMP velocities following a Maxwell-Boltzmann distribution with some dispersion, through which the solar system is traveling. A bound on the WIMP velocity is set to account for the galactic escape velocity. We note that the Earth's orbit around the Sun results in a periodic modulation of the WIMP flux, which forms the basis of searches looking for an annually modulated dark matter signal.

With a $40\,\mathrm{GeV}/c^2$ target, momentum transfers of $\sim 0.2\,\mathrm{GeV}/c$ (corresponding with recoil energies of $\sim 0.7\,\mathrm{MeV}$) have de Broglie wavelengths of $\sim 5\,\mathrm{fm}$, which is comparable to the nuclear radius. In this regime, the WIMP-nucleus scattering is coherent, *i.e.*, the WIMP interacts with the entire nucleus. Depending on the spin of the target nucleus, then, there could be spin-dependent or spin-independent scattering. The latter case is interesting here because ^{40}Ar, the primary argon isotope in underground argon (the target in DarkSide-50) has spin 0. Because the scattering is coherent, the total scattering amplitude involves a sum over all A nucleons in the nucleus; the scattering cross-section is the square of the amplitude, and thus is enhanced by an A^2 factor. While this favors heavier targets (*e.g.*, xenon and germanium), it is offset by the lower recoil energy—and thus lower threshold—required for coherent scattering with such targets [21]. In more energetic recoils, the loss of coherence is accounted for with a nuclear form factor. (We note that in targets such as xenon, the presence of isotopes with non-zero spin provides some sensitivity to spin-dependent WIMP-nucleus interactions [22].)

For an elastic WIMP-nucleus scatter, the recoil energy E is maximized in the case of a back-scatter:

$$E_{\max} = \frac{2M_T(m_\chi v_\chi)^2}{(m_\chi + M_T)^2} \tag{1.1}$$

where m_χ is the WIMP mass, M_T is the mass of the target nucleus, and v_χ is the incoming (non-relativistic) WIMP velocity. Since the target nuclei in direct detection

experiments have masses on the order of 10-100 GeV/c^2, and $v_\chi = 232\,\mathrm{km\,s^{-1}} \approx 10^{-3}c$, experiments with a threshold on the keV scale are sensitive to $m_\chi \gtrsim 10\,\mathrm{GeV}/c^2$. More generally, this means that lower signal thresholds are needed for greater sensitivity to low mass WIMPs.

The mathematics for deriving the WIMP-nucleon scattering cross-section is briefly reviewed in Ch. 9. Figure 1.1 summarizes the limits on the spin-independent WIMP-nucleon scattering cross-section (σ_{SI}) set by the leading direct detection experiments as of Jan 2018. The individual curves denote 90% C.L. upper bounds on σ_{SI} set by their respective experiments—*i.e.*, if σ_{SI} was actually above the curve, there was a $\leq$0.1 probability for these experiments to have observed what they actually did.

For the WIMP masses shown ($10\,\mathrm{GeV}/c^2$-$10\,\mathrm{TeV}/c^2$), the lowest upper bounds on σ_{SI} have been set by LUX [16], XENON1T [17], and PandaX-II [18], xenon TPC experiments with ∼30-50 tonne-day exposures. DEAP-3600 [19] is a tonne-scale (active volume) single-phase liquid argon experiment, whose reported result was for a ∼10 tonne-day exposure; it and DarkSide-50 [20] have reported the best limits on σ_{SI} by liquid argon experiments. Because DarkSide-50 is the smallest detector by some margin among the ones just mentioned—with a ∼50 kg active volume, *vs.* the 250 kg volume of LUX, the next smallest detector—a competitive limit on σ_{SI} is not expected; however, it is unique for being the only argon TPC experiment.

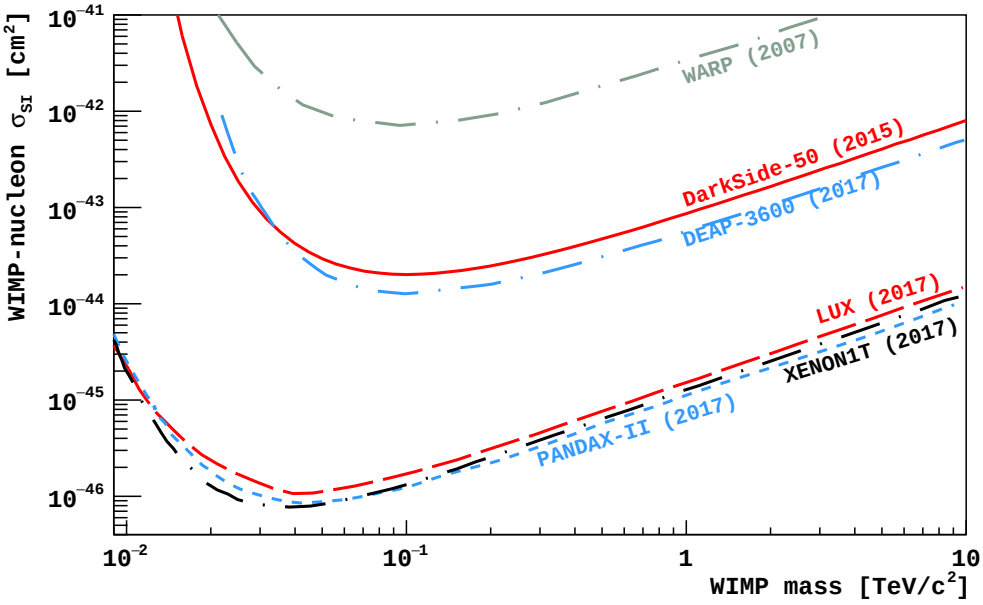

Figure 1.1: Upper limits (90% C.L.) on the WIMP-nucleon scattering cross-section, *vs.* WIMP mass, established by various noble liquid direct-detection experiments.

Chapter 2

DarkSide-50

DarkSide-50 (DS-50) is the second iteration of the DarkSide program (beginning in 2011 with the deployment of DarkSide-10) of liquid argon (LAr) time projection chamber (TPC) experiments for the direct detection of WIMP dark matter. DS-50 consists of three nested detectors, with the LAr TPC in a cryostat at the center of a liquid scintillator veto (LSV), which is in turn encompassed by a water Cherenkov veto (WCV) (Fig. 2.1). The ensemble of detectors is located in Hall C at Laboratori Nazionali del Gran Sasso (LNGS) in Italy, ∼1400 m underground (3800 m water equivalent).

DS-50 was first deployed with atmospheric argon (AAr), from Nov 2013 to May 2014 [23]. The second deployment, with underground argon (UAr) that was depleted in β-emitting ^{39}Ar, began in Apr 2015; analysis of the first 70.9 d of UAr data (the "70d UAr" analysis/data) is described in [20] (the benefit of using UAr will be discussed in Sec. 3.2.7). In this work we detail the blind analysis of the subsequent 532 d of data (the "530d UAr" analysis/data), taken from Aug 2015 to Oct 2017.

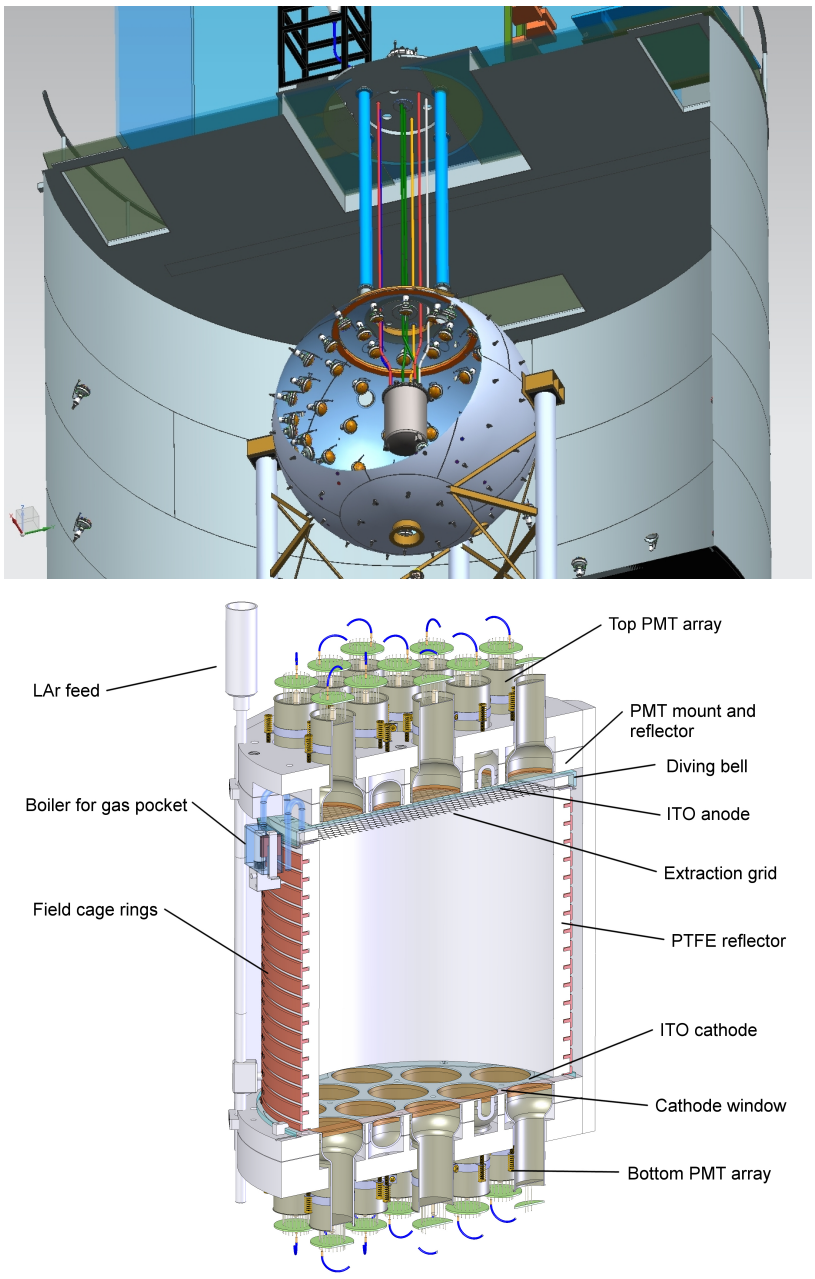

Figure 2.1: **Top:** The nested detectors comprising DarkSide-50. The liquid argon time projection chamber is in the cylindrical cryostat at the core, surrounded by the spherical liquid scintillator veto. Both of these are deployed in the cylindrical water Cherenkov veto. **Bottom:** The liquid argon time projection chamber. Both figures from [20].

2.1 Outer detectors

The outer detectors (OD) comprised of the LSV and the WCV, which are described in detail in [24] and [25].

The WCV is a 10 m tall × 11 m diameter cylinder filled with 1 kt of radio-purified water that is viewed by 80 ETL 9351 8" photomultiplier tubes (PMTs). It was used to veto events coincident with cosmogenic muon activity, as tagged by the consequent Cherenkov radiation in the WCV, or the Cherenkov radiation from their accompanying electromagnetic showers. This provided a handle on cosmogenic neutron background.

The LSV is a 4 m diameter stainless steel sphere within the WCV. It was filled with 30 t of a boron-loaded liquid scintillator cocktail, containing 95% pseudocumene (PC), 5% trimethyl borate (TMB), and 1.4 g L^{-1} 2,5-diphenyloxazole (PPO) [25, Tab. 8.3]. It was instrumented with 110 Hamamatsu R5912 LRI 8" PMTs, which detect scintillation from neutron scatters, neutron captures, or Compton scattering of γ-rays in the LSV.

The LSV and WCV provided not only passive shielding for the TPC, but active vetoing capabilities for neutron backgrounds as well. This provided an *in situ* measurement of the experiment's neutron background that, when combined with measured veto efficiency from neutron source calibration, was key to achieving DS-50's goal of background-free running.

2.1.1 Data acquisition and relevant reconstructed variables

Data acquired for the 530d UAr analysis were triggered on a signal in the TPC. Each PMT in the LSV and the WCV was read out in a separate channel, digitized at a 1.25 GHz sample rate over a 200 µs acquisition window spanning (−10.5, 189.5) µs relative to the TPC trigger. Calibration of the single photoelectron (SPE) signal in

each PMT was done using a low-intensity laser, through optical fibers pointed at the photocathode of each PMT.

Zero-suppression was done on the individual PMT waveforms as they were read out, with the channel waveforms only being recorded when they satisfied an amplitude threshold set to correspond to $\sim$0.25 PE. These recorded pulses included the twenty samples both before and after the sampling range satisfying the amplitude threshold. The first fifteen samples in each pulse were used to establish a channel baseline for the pulse, with which signals from various channels were aligned when summed. Channel waveforms in the LSV and WCV were summed separately (after normalizing for the channels' respective SPE responses), from which integrals (in [PE]) over various timing windows, including over the entire summed waveform, were obtained.

Signals in the summed LSV waveform were grouped into clusters representing LSV scintillation events using the "Top-Down Cluster Finder" algorithm:

1. The peak amplitude in the waveform was found. If the found peak had an amplitude $<$2 PE, the clustering process was terminated.

2. If the found peak had an amplitude $>$2 PE, a start time for the cluster was established by searching the preceding samples until no LSV signal was within 20 ns of the working start time.

3. From the peak, an end time for the cluster was established by searching subsequent samples until no LSV signal was within 20 ns of the working end time.

4. The preceding steps were repeated on the remaining waveform, *i.e.*, without scanning over found clusters.

Integral, timing, and multiplicity (*i.e.*, the number of PMTs contributing to the cluster signal) information were thus reconstructed on the cluster-level in the LSV. Similar clustering was done on the summed WCV waveform; however, cluster-level information from the WCV was not used in the 530d UAr analysis.

2.2 Liquid argon time projection chamber

The LAr TPC (Fig. 2.1) was situated within a stainless steel cryostat at the core of the LSV. The active argon was a two-phase (liquid/gas) volume contained on the side by a Teflon cylinder, and on the top and bottom by fused silica windows, measuring 35.6 cm tall × 35.6 cm diameter when warm. The active argon was viewed through the windows by top and bottom arrays of 19 Hamamatsu R11065 3" PMTs each. The PMTs were fitted with cold preamplifiers that allowed their use with a lower gain, which was instrumental to operating them without breakdown issues [26]. For completeness, we note that the original plan was to deploy DS-50 with the more radio-pure R11065-20 PMTs instead; however, the tubes we had on hand experienced catastrophic electrical breakdown at LAr temperature in a trial deployment of the TPC, and were thus replaced with the older R11065's in the final deployment.[1]

In two-phase operation, liquid argon was continuously boiled to create a ∼1 cm thick gas pocket that was trapped by a rim along the circumference of the top fused silica window, which was thus referred to as the "diving-bell". The thickness of the gas pocket was fixed by a bubbler welded to the diving-bell, which allowed excess argon gas to escape.

The top and bottom fused silica windows were each coated with a 15 nm thick layer of indium-tin-oxide (ITO), which were held at 0 V (anode) and −12.7 kV (cathode) respectively. A 50 µm thick stainless steel mesh with a hexagonal grid pattern was located 5 mm below the liquid surface and held at −5.6 kV. The grid, anode window, and cathode window maintained a 200 V cm^{-1} (2.8 kV cm^{-1}, 4.2 kV cm^{-1}) drift field

[1] For posterity, we would also like to log another experience from the trial deployments of the TPC, involving short-circuits in the PMT base connections when the cryostat was evacuated. It was found that a mix-up in the solder pastes—wherein a paste with water-soluble flux was expected, but a paste leaving an insoluble flux residue was used instead—was likely responsible, by allowing excess solder to shift along with the flux residue during evacuation. The use of excess amounts of solder was exacerbated by a lack of experience with this paste. A campaign of repeated soldering and evacuation in a vacuum oven was performed to ensure the solder joints were stable enough for deployment.

(extraction field, electroluminescence field). Copper rings and resistors on the external surface of the Teflon cylinder formed a voltage divider that kept the drift field uniform.

The surfaces of the Teflon cylinder, diving-bell, and cathode window facing the active argon were coated with a $\sim$200 µg cm^{-2} thick layer of tetraphenyl butadiene (TPB). TPB is a wavelength shifter that converts the 128 nm LAr scintillation into visible light ($\sim$420 nm) for detection by the PMTs [27].

2.2.1 Event signals

TPC events were dominated by scattering of various background γ-rays and particles in the active argon volume. There are typically two classes of events that result from such scatters: 1) Electron recoils (ER) from β-decay or Compton-scattering of γ-rays; and 2) Nuclear recoils (NR) from impinging neutrons or α's. Both ERs and NRs result in LAr scintillation via the production of ions or excitons in the LAr, and the subsequent formation and decay of excited argon dimers [28]. In the process involving ionization, Ar_2^+ recombines with electrons to form argon excitons (Ar^*):

$$\begin{aligned} Ar^+ + Ar &\rightarrow Ar_2^+ \\ Ar_2^+ + e^- &\rightarrow Ar^{**} + Ar \\ Ar^{**} &\rightarrow Ar^* + \text{heat} \end{aligned} \tag{2.1}$$

Argon excitons—from either the original scatter or Ar_2^+-e^- recombination—subsequently dimerize when they collide with unexcited argon atoms:

$$Ar^* + Ar \rightarrow Ar_2^* \tag{2.2}$$

The excited dimers then decay, producing scintillation in the form of a 128 nm photon:

$$Ar_2^* \rightarrow 2Ar + h\nu \tag{2.3}$$

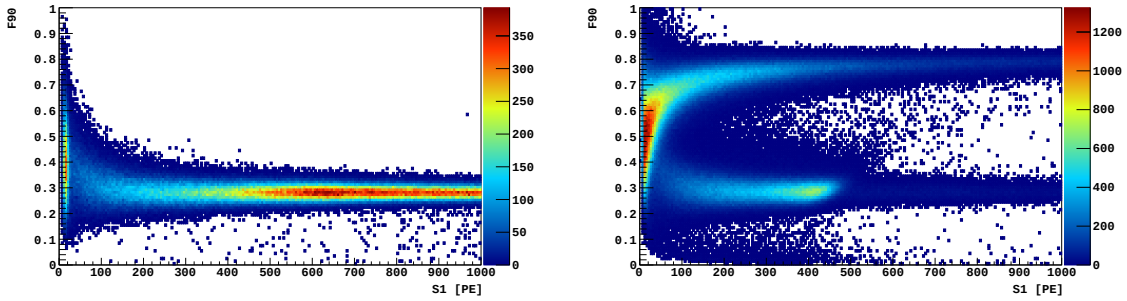

Figure 2.2: F90 *vs.* S1 of data taken (left) during regular UAr running, and (right) with an ^{241}AmBe calibration source deployed. The separation between the nuclear and electron recoil bands in F90 is clearly visible. UAr data and cuts from the 70d UAr analysis [20] have been used; in the case of the ^{241}AmBe data, veto cuts have not been applied.

where $h\nu$ represents the emitted photon. As mentioned above, these scintillation photons were wavelength-shifted to ∼420 nm by TPB for detection by our PMTs. In DS-50, the scintillation signal was measured in photoelectrons (PE), and referred to as "S1".

The Ar_2^* excimers in Eqn. 2.3 can be in either the singlet or triplet state, which have lifetimes of ∼7 ns and ∼1.6 µs respectively. The singlet-to-triplet ratio is ∼0.3 for ERs, and ∼3 for NRs [29]—*i.e.*, NR scintillation is more prompt. Accordingly, discrimination between ERs and NRs is primarily done using the shape of their respective S1 pulses. In DS-50, a parameter called F90—defined as the fraction of the pulse integral in the first 90 ns—was used for this pulse shape discrimination (PSD). As seen in Fig. 2.2, although its usefulness was limited by statistical fluctuations at lower S1, PSD effectively separates ERs from NRs at high S1.

In DS-50, ionization electrons were drifted toward the top of the TPC by an electric field (the drift field), where they were extracted from the liquid into the gaseous argon. The electroluminescence signal from the passage of these electrons through the argon gas produced a second event pulse, referred to as the ionization signal or "S2".

In LAr, ERs have a lower excitation-to-ionization ratio than NRs, with ratios of 0.21 for ERs [30] and 1 for NRs [31, Tab. VIII] typically used. Since ERs have less excitation to ionization relative to NRs, they have higher S2/S1 for the same S1, which provides another handle on ER/NR discrimination.

Algorithms were developed to reconstruct the event's horizontal (xy) position from the distribution of its S2 light across the various PMTs [32, 33]; the xy-reconstruction algorithm described in [32] was used for the analysis described here. The time separation ("drift time") between the S1 and S2 signals was a measurement of the vertical (z) location of the recoil. Notably, drift time and S2 information are not available in single-phase experiments such as DEAP-3600 [19] (although three-dimensional position reconstruction is still possible with only the scintillation signal).

Recoil signals in liquid xenon are produced via basically the same channels as in argon [29, 30]. However, the ionization to scintillation ratio is more powerful than PSD in the case of xenon, and hence the large xenon experiments (LUX [16] and Xenon [17]) are both two-phase TPC experiments.

In DS-50, recoil electrons from Compton-scattering of γ-rays in the Teflon and fused silica adjacent to the active argon also produced Cherenkov radiation that could be detected by the PMTs. In the absence of an accompanying scatter in the active argon, these were single-pulse (*i.e.*, S1-only) events with an entirely prompt signal (F90$\approx$1).

2.2.2 Data acquisition and relevant reconstructed variables

WIMP search data were collected via triggers on a TPC signal, which required the detection of $\geq$0.6 PE each by at least 2 TPC PMTs; each trigger of the data acquisition this way was referred to as an "event". Each TPC PMT was read out in a separate channel, digitized at a 250 MHz sample rate over a 440 µs acquisition window spanning (-5, 435) µs relative to the trigger time. A 810 µs inhibit window was enforced

with each trigger (starting at the trigger time), during which new triggers were not accepted. Calibration of the SPE signal in each PMT was done using a low-intensity laser, through an optical fiber pointed into the TPC from the bottom PMT array. Unlike in the OD, zero-suppression was not done on the TPC channel waveforms before recording.

For each channel, a starting baseline was established by looking in a 80 ns window centered about the highest (positive) amplitude fluctuation in the pre-trigger portion of the waveform (keeping in mind photoelectron signals resulted in negative fluctuations). If fluctuations about this positive pre-trigger peak were small, a baseline was deemed to have been found for the event. The baseline for the rest of the channel waveform was then constructed as the moving average in a sliding 80 ns window, interpolated over regions with signal (*i.e.*, large negative fluctuations). The individual channel waveforms were normalized to account for their respective SPE responses, and had their baselines subtracted, before the summed waveform was made.

Pulse-finding was then done on the summed waveform. In brief, this consisted of the following steps:

1. A down-sampled waveform was created by combining blocks of 500 consecutive fine samples (each 4 ns wide) together into coarse samples.

2. A pulse was found by searching, in chronological order, for a large change (>6 PE) in the waveform's amplitude between consecutive coarse samples. If no such change was found, the pulse-finding algorithm was terminated.

3. If a large change in the down-sampled waveform was found, a start time for the pulse was established by searching the fine samples comprising the working coarse samples chronologically for a large signal amplitude (>0.3 PE). The starting time of the pulse was declared to be 2 fine samples (*i.e.*, 8 ns) prior to this fine sample.

4. From the start time, an end time for the pulse was established by searching subsequent fine samples until the integrated signal in a 3.2 µs window starting from the working sample was small (<2 PE). Alternatively, an end time was declared for the current pulse if a subsequent pileup pulse was found.

5. Steps 2 through 4 were repeated until the algorithm terminated.

Pulses were thus found on the summed waveform, each demarcated with a start and an end time. Because S1 and S2 pulses have different pulse shapes, a pseudo-F90 parameter was constructed when a pulse was found, using the pulse's integral in its first 88 ns and 3.5 µs. The parameters in the description above (coarse and fine sample thresholds, and the width and integrated signal threshold of the end time search window) were applied to pulses with pseudo-F90 >0.12, which were deemed to be S1-like. Different sets of parameters were used for S2-like pulses, and pileup pulses (*i.e.*, pulses occurring before the end of the previous pulse).

After pulse-finding, all TPC analysis parameters were derived from the waveform:

- The number of pulses associated with an event was the number of pulses found on the summed waveform.

- The drift time was the separation between the start times of the first and second pulses. This definition was also used for events with more than two pulses. It is a meaningless quantity for events with only one pulse.

- Event S1 and F90 were derived from the earliest pulse in an event. S1 was the integral of the summed waveform in the first 7 µs of this pulse, beginning from its found start time. F90 was the fraction of S1 in the first 88 ns of this pulse.

- Event S2 and S2 F90 were derived from the second pulse in an event. S2 was the integral of the summed waveform in the first 30 µs of this pulse, beginning

from its found start time. S2 F90 was the fraction of S2 in the first 88 ns of this pulse.

- The light distribution pattern associated with a particular pulse was available by looking at information from the individual channel waveforms.

A detailed review of TPC data reconstruction can be found in [34, Ch. 3].

2.2.3 Recoil energy to S1 light yield calibration

The correlation between the observed S1 signal and the electron recoil energy, referred to as a light yield and quoted in [PE/keV], was measured via the deployment of various calibration sources. One such source was ^{83m}Kr from ^{83}Rb decay [35], which was injected directly into the TPC via a rubidium-infused charcoal pellet placed in a normally valved off loop in the argon recirculation system. Although its decay to ^{83}Kr is a two-stage process, ^{83m}Kr produced a mono-energetic S1 signal (32.1 keV+9.4 keV conversion electrons) in the TPC because the second decay in the sequence has a lifetime of 222 ns, which is short compared to the lifetime of the long-lived triplet state of Ar_2^* (1.6 µs). This did not introduce persistent contamination as the ^{83m}Kr itself has a lifetime of 2.64 h.

The ^{83m}Kr signal manifested as a peak in the S1 spectrum at ∼303 PE (∼333 PE) with a 200 V cm^{-1} (0 V cm^{-1}) drift field; this corresponded with a measured light yield of 7.29 PE/keV (8.03 PE/keV) [36, 37]. The ^{83m}Kr calibration was thus an important measure of the ER light yield at approximately the middle of the WIMP search S1 range of interest (<500 PE). We note as well that the light yield was lower in the presence of a drift field, as drifting electrons reduces Ar_2^+-e^- recombination, which suppresses one mode of the scintillation process (Eqn. 2.1).

External γ sources—^{133}Ba, ^{57}Co and ^{137}Cs, providing 356 keV, 122 keV+14 keV and 662 keV γ-rays respectively—were also deployed with the Calibration Insertion

System (CALIS) [38]. These provided peaks at higher ER energy for light yield measurement [39, Tab. 5.1]. For completeness, we note as well that the end-point of the ^{39}Ar spectrum has previously also been used for ER light yield estimation [23, Sec. 7].

As there was no way to get NRs of known energy in DS-50, a cross-calibration with the SCENE experiment was done to obtain the NR energy to S1 light yield (quoted in [PE/keV$_{\mathrm{nr}}$]). In particular, the ER light yield measured using $^{83\mathrm{m}}$Kr at null field in DS-50 ($\mathrm{LY_{Kr}}$) was scaled with $\mathcal{L}_{\mathrm{eff}}$, defined as SCENE's measurement of the scintillation efficiency of NRs with known energy relative to that of $^{83\mathrm{m}}$Kr ERs at null field [31], *i.e.*

$$\begin{aligned} \mathrm{S1_{NR}} &= E_{\mathrm{NR}} \times \mathcal{L}_{\mathrm{eff}} \times \mathrm{LY_{Kr}} \\ &= E_{\mathrm{NR}} \times \mathrm{LY_{NR}} \end{aligned} \tag{2.4}$$

where $\mathrm{S1_{NR}}$, E_{NR}, and $\mathrm{LY_{NR}}$ were the NR S1, NR energy, and NR light yield in DS-50, respectively.

2.2.4 Corrections to S1 and S2

S1

Total internal reflection at the gas-liquid interface resulted in a lower light yield near the top of the TPC (shorter drift times) relative to the bottom (longer drift times). This drift time dependence was corrected for using an empirical correction factor f:

$$f = \frac{0.0407 \times t^5 - 0.206 \times t^4 + 0.407 \times t^3 - 0.389 \times t^2 + 0.247 \times t + 0.898}{0.9977} \tag{2.5}$$

where t was the drift time relative to that at the middle (vertically) of the TPC:

$$t = \frac{t_{\mathrm{drift}}}{0.5 \times t_{\mathrm{drift\ max}}} \tag{2.6}$$

where $t_{\text{drift max}}$=376 µs was the maximum drift time, associated with an event occurring right above front of the cathode window. Equation 2.5 was determined by fitting the observed position of the ^{83m}Kr peak in the uncorrected S1 ($S1_{\text{uncorr}}$) spectrum as a function of drift time; the observed S1 closer to the top and bottom of the TPC was corrected to match that observed in the middle. Since $0 < t < 2$, the correction factor ranged from 0.9 at the top of the TPC to 1.1 at the bottom. S1 or $S1_{\text{corr}}$ will be used to refer to the drift time corrected quantity, *i.e.*,

$$S1 \equiv S1_{\text{corr}} = S1_{\text{uncorr}} \times f \tag{2.7}$$

S2

In the course of operating DS-50, it was discovered that S2 *vs.* S1 for our events varied with their reconstructed radii, with events reconstructed near the center (in xy) of the TPC having S2 $\sim$4$\times$ that of events with the same S1 reconstructed near the TPC wall [40, App. D]. It has been postulated that this could be the result of a slight sag in the diving-bell, with the consequent thinner gas pocket/stronger electric field near the center of the TPC resulting in higher electroluminescence light yield there; however, this has yet to be confirmed. An empirical correction on uncorrected S2 ($S2_{\text{uncorr}}$) was applied to account for this radial dependence, scaling $S2_{\text{uncorr}}$ of events based on their reconstructed xy position to match that of events reconstructed at the center—*i.e.*, events reconstructed at or near the center had their $S2_{\text{uncorr}}$ scaled by a factor of $\sim$1, which increased to $\sim$4 close to the TPC wall. S2 or $S2_{\text{corr}}$ will be used to refer to the xy corrected quantity.

Electronegative impurities in the LAr such as oxygen are known to capture drifting electrons, and hence result in decreasing S2 light yield with increasing drift time [41]. This was quantified in DS-50 by fitting an exponential decay to the S2 *vs.* drift time distribution, with the fitted time constant referred to as the electron drift lifetime

(often contracted to electron lifetime). The data were consistent with an electron drift lifetime of >5 ms [20], which is much longer than the maximum drift time of 376 µs; thus, we did not perform a drift time dependent correction on S2.

Chapter 3

Background overview

The goal of the WIMP search was to count WIMP-argon scattering events in the detector. To achieve this aim, the bulk of the analysis was focused on understanding and containing the various detector backgrounds, culminating in a background prediction which formed the basis of a null hypothesis that observed WIMP signals would be inconsistent with.

Although great effort was expended by the collaboration to use materials with low inherent radioactivity (including the procurement of UAr), and to keep them radiopure, some level of residual background was inevitable. In this chapter we describe the main backgrounds for the WIMP search analysis, the radioisotopes these backgrounds stemmed from, as well as the method used to estimate the activity of these radioisotopes in various detector locations.

3.1 Main backgrounds

Since WIMP events were expected to be rare, almost all the acquired data were background of some kind. There were three main types of background for the WIMP search analysis, which were identified in the detector design process and over the course of previous DarkSide analyses.

3.1.1 Neutron background

Neutrons entering the detector could be radiogenic or cosmogenic in origin—the former from fission or (α, n) reactions following α-decay, and the latter from cosmic ray interactions in surrounding material.

A neutron scatter in the active argon results in a nuclear recoil, just as a WIMP scatter would. However, neutron events can be distinguished from WIMP events via multiple interactions of the neutron—multiple S2 signals in the TPC, or an interaction in the veto.

During the detector design and cut development process, estimates of the neutron background were made using Monte Carlo simulations of various radioisotope decay chains in different detector locations (Sec. 3.2); in particular, an (α, n) yield calculator was developed for this purpose [25, Sec. 4.4.3]. The details surrounding these background estimates comprise volumes of work on their own, and so we direct interested readers to [25], and the upcoming work by Qian, for more thorough discussion.

As mentioned earlier, the advantage of having a neutron detector (instead of passive neutron shielding) as part of the experiment was that it provided a means of measuring DS-50's neutron background while WIMP search data were being acquired. In the later stages of the 530d UAr analysis, such a measurement of the actual neutron background was made (Sec. 6.3.1 and Sec. 6.3.2).

The LSV was an important component of the detector, whose purpose was to detect signals associated with neutron thermalization and capture. The criteria used for selecting neutron events in the WIMP search data are described in Sec. 4.3. The efficiencies of these event selection criteria at tagging TPC events triggered by a neutron scatter were measured using data from ^{241}Am^{13}C source calibration. Briefly, the ^{241}Am^{13}C source provided a source of neutrons with few coincident γ-rays, with which the scintillation response in the LSV was calibrated, and the neutron tagging

efficiencies of our LSV cuts were measured. Again, [25] and the upcoming work by Qian should be consulted for greater detail.

3.1.2 Surface background

α-decay produces an α-particle and a recoiling nucleus, both of which induce argon scintillation with NR-like F90. Because the emitted α-particles are typically very energetic, α-decays in the bulk of the liquid argon were not a problem for the WIMP search analysis due to their large scintillation signals. Since the emitted α-particles and recoiling nuclei generally have a short range because of their mass (the former also because of their charge), α-decays only posed a problem when they occurred on TPC surfaces touching the active argon, and hence were referred to as surface backgrounds. In this case, the particles' energies were easily degraded by intervening material [42], which could put their resultant S1 signal in the WIMP search range. Surface background in DS-50 resulted from α-decay of radon daughters on the inner surfaces of the TPC (Sec. 3.2.9).

High energy peaks (>30000 PE) were identified in the S1 spectrum of events with NR-like F90 ($0.5 < \text{F90} < 0.9$) [42, Sec. 8.3]. In particular, two of these peaks were found to be consistent with that from ^{222}Rn and its daughter ^{218}Po, comprising of events with correlated trigger times consistent with the latter's 3 min half-life. Although no selection for surface α-decays was done, via a fit, the profile of the S1 peak associated with ^{210}Po decay was found to be consistent with that of α-particles which had been degraded by intervening material. This indicated that ^{210}Po was the main source of surface background for the WIMP search analysis, with an observed α-emission rate of $(2.51 \pm 0.01)\,\text{mBq/m}^2$ on the TPC wall [43, Sec. IIIA].

Drift time fiducialization was effective against surface backgrounds from the anode and cathode windows; however, α-decays on the Teflon surfaces remained an issue. Problematic α-decays could occur on either the argon-TPB interface, or the TPB-

Teflon interface. Considering the two decay products (the α-particle and the recoiling nucleus), there were four event topologies:

1. A decay on the argon-TPB interface, with the α-particle (nucleus) recoiling into the argon (TPB).

2. A decay on the argon-TPB interface, with the α-particle (nucleus) recoiling into the TPB (argon).

3. A decay on the TPB-Teflon interface, with the α-particle (nucleus) recoiling into the TPB (Teflon).

4. A decay on the TPB-Teflon interface, with the α-particle (nucleus) recoiling into the Teflon (TPB).

We note that: In case 1, the scintillation signal was expected to be large (above the WIMP search S1 range) since the α-particle is not degraded before entering the liquid argon; and in case 4, the recoiling nucleus was expected to be stopped by the TPB before reaching the liquid argon. This left the cases where the α-particle entered the TPB as particularly problematic [42, Sec. 6.1]. A cut looking for α-induced scintillation of the TPB was developed to discriminate against such events (Sec. 4.5.1).

In DS-50, we observed a significant rate of single-pulse events (*i.e.*, with one S1 pulse but no S2) with NR-like F90. These were posited to be scatters very close to the TPC wall, whose ionization electrons were lost to the wall while being drifted. Since these were single-pulse events, a random coincidence with a stray S2-like signal would have been enough to create a spurious WIMP-like event. The rate of these single-pulse events was estimated by studying the 70d UAr data, and later, the single-pulse events in the 530d UAr data (Sec. 6.3.3). As there were too many of these single-pulse events to have been neutron scatters, they were classified as surface backgrounds. The

event selection criteria used to discriminate against such background events are also discussed in Sec. 4.5.

3.1.3 Electron recoil background

Electron recoil events in DS-50 resulted from Compton scattering of γ-rays from radioactive decay and electrons from β-decay in the bulk of the active argon. Although PSD provided a powerful handle on ER events, they were a far more prevalent background than neutron or surface events—ERs were the dominant contributor to background in the WIMP signal region in the AAr and 70d UAr analyses. To make matters worse, the 70d UAr analysis indicated that Cherenkov radiation in the Teflon and fused silica volumes volumes, when coupled with a Compton scatter in the active argon, resulted in TPC events with higher F90 and lower S2 than typical ERs, *i.e.*, making them more NR-like.

To estimate the ER background, a hybrid model was developed, using the collaboration's Geant4-based Monte Carlo simulation to handle γ-ray kinematics and Cherenkov radiation, and the AAr data as a reference for ER F90 (Ch. 5). These simulations were of radioisotope decay chains in various detector locations (Sec. 3.2), normalized using rates estimated from an energy spectrum fitting process (Sec. 3.3). The ER background model was used in the development of the main event cut utilizing PSD, *i.e.*, the definition of the WIMP search region in F90 *vs.* S1 phase-space (Ch. 7).

Background from Cherenkov radiation

DS-50 was sensitive to Cherenkov radiation emitted by the passage of energetic electrons in the fused silica (individual PMT windows, and anode/cathode windows) or Teflon (TPC top/bottom/side walls) volumes adjacent to the active argon. These

could be recoil electrons from Compton scattering, or energetic β's from radioactive decay.

The refractive index for fused silica n_{FS} ranges from 1.45 to 1.68 over our wavelengths of interest (visible to ultraviolet). Thus, the minimum electron velocity for the generation of Cherenkov radiation in fused silica was

$$v_{\text{thres, FS}} = c/n_{\mathrm{FS}} = c/1.68 = 0.6c \tag{3.1}$$

which required a kinetic energy of

$$E_{\text{thres, FS}} = \frac{m_e c^2}{\sqrt{1-\beta^2_{\text{thres, FS}}}} - m_e c^2 = 0.25 m_e c^2 \tag{3.2}$$

where $\beta_{\text{thres, FS}} = v_{\text{thres, FS}}/c = 0.6$. Substituting this into the formula for Compton scattering

$$E_{\text{thres, FS}} = E[1 - (1 + \frac{2E}{m_e c^2})^{-1}] \tag{3.3}$$

we see that it corresponded with the Compton edge of a 250 keV γ-ray. Similarly, the refractive index for Teflon n_{Tef}=1.35 corresponded with the Compton edge of a 400 keV γ-ray. As we will see, these were not particularly high thresholds given the sources of radioactivity in the detector.

3.2 Notable background-producing radioisotopes

The following radioisotopes present in various detector locations were found to be responsible for most of the observed background in DS-50. The major sources of radioisotope activity in DS-50 were the PMTs, 25 mm stainless steel of the flanges, 5 mm stainless steel of the cryostat, stainless steel cryostat nuts and bolts, stainless steel tubes leading to the cryostat, Viton o-ring, Mylar multi-layer insulation (MLI),

and the UAr. Since the LSV was an excellent passive shield, only radioactivity from the cryostat and its contents (*i.e.*, the liquid argon and the TPC) posed an issue.

3.2.1 Uranium-238

^{238}U is a primordial radionuclide, with a natural abundance of 99.27% and half-life of 4.5×10^9 yr [44]. It is present in soil with a median activity concentration of $35\,\mathrm{Bq\,kg^{-1}}$, which varies with location (e.g., soils from igneous sources tend to have higher activities) [45, Annex B Tab. 5].

^{238}U can undergo spontaneous fission with a branching ratio of 5.45×10^{-7}, producing an average of 2.01 neutrons per decay that may then scatter in the TPC; α-decay in the ^{238}U decay chain is also a source of neutrons from subsequent (α, n) reactions [25].

Secular equilibrium

When the daughter (d) of a parent radionuclide (p) is itself radioactive, the decay rate of the daughter can be described by the Bateman equation

$$\frac{dN_d}{dt} = \lambda_p N_p - \lambda_d N_d \tag{3.4}$$

where N is the number of each nuclide, and λ its decay constant. Recall that

$$N_p = N_{0p} e^{-\lambda_p t} \tag{3.5}$$

where N_{0p} is the initial number parent nuclides, so we have a first-order linear ODE

$$\frac{dN_d}{dt} + \lambda_d N_d = \lambda_p N_{0p} e^{-\lambda_p t} \tag{3.6}$$

which can be solved with an integrating factor

$$f(t) = e^{\int \lambda_d dt} = e^{\lambda_d t} \tag{3.7}$$

Thus,

$$\begin{aligned} N_d &= e^{-\lambda_d t} \int e^{\lambda_d t} \lambda_p N_{0p} e^{-\lambda_p t} dt \\ &= \lambda_p N_{0p} e^{-\lambda_d t} \int e^{(\lambda_d - \lambda_p)t} dt \\ &= \frac{\lambda_p}{\lambda_d - \lambda_p} N_{0p} e^{-\lambda_p t} + C e^{-\lambda_d t} \\ &= \frac{\lambda_p}{\lambda_d - \lambda_p} N_{0p} (e^{-\lambda_p t} - e^{-\lambda_d t}) \end{aligned} \tag{3.8}$$

if we start with none of the daughter nuclide.

If the half-life of the parent is much longer than that of its daughter ($\lambda_p \ll \lambda_d$), N_d becomes dependent on the decay of only the parent nuclide after several half-lives of the daughter:

$$N_d \rightarrow \frac{\lambda_p}{\lambda_d - \lambda_p} N_{0p} e^{-\lambda_p t} \approx \frac{\lambda_p}{\lambda_d} N_{0p} e^{-\lambda_p t} \tag{3.9}$$

Substituting eqn. 3.9 into eqn. 3.6 shows that $\frac{dN_d}{dt} = 0$ in this situation, known as secular equilibrium.

Since daughter decays now occur at the same rate as that of the parent, the same reasoning can be applied to subsequent daughters (as long as their respective half-lives are shorter than the parent) to show that the entire decay chain can be in secular equilibrium with its parent radionuclide. This is the case for ^{238}U, whose half-life is much longer than that of any of its daughters (the longest of which is for ^{234}U, at 2.5×10^5 yr; the same applies to ^{235}U and ^{232}Th.

Chain-breaking

Secular equilibrium is not guaranteed, even if it is possible. In general, breaking of secular equilibrium results from changes in the abundance of an element in the decay

chain from non-decay processes. For example, handling of the material could result in the removal of, or contamination with, certain elements; alternatively, an element could be very mobile—*e.g.*, ^{222}Rn in the ^{238}U chain can leave the sample via diffusion.

When such a break occurs, secular equilibrium can be re-established among the subsequent daughters. Thus, in the example of ^{222}Rn in the ^{238}U chain, since $t_{1/2}(^{222}\mathrm{Rn}) = 3.8\,\mathrm{d} \gg t_{1/2}(^{218}\mathrm{Po}) = 3.2\,\mathrm{min}$, subsequent daughters can be in secular equilibrium with ^{222}Rn instead of ^{238}U.

Note that some activity estimates were obtained from the detection of γ-rays from specific elements in the decay chain—*e.g.*, germanium counting of ^{238}U only looked for ^{234}Th, $^{234\mathrm{m}}$Pa, ^{214}Pb, and ^{214}Bi. Secular equilibrium in sections of the decay chain was then assumed to ascribe these estimated activities to other daughter elements based on their position in the decay chain. As mentioned above, the establishment of secular equilibrium should take several half-lives of the daughter. Since the daughters of ^{222}Rn up to ^{214}Po all have short half-lives ($<$1 h), the assumption of secular equilibrium is reasonable. The same reasoning applied to ^{226}Ra—with a half-life of 1600 yr—suggests that it is unlikely to be in secular equilibrium with its progenitor (^{230}Th) if either of their abundances have been changed in the recent past; similarly, ^{210}Pb ($t_{1/2} = 22.2\,\mathrm{yr}$) may not be in secular equilibrium with its predecessors in the lower chain.

In the case of ^{238}U, then, we will refer to the upper and lower parts of the chain, and ascribe a different activity to each. In the various DS-50 materials, it was not clear which element ought to be the parent of the lower chain. Compelling candidates were ^{226}Ra (due to its long half-life), and ^{222}Rn (due to its potential for out-diffusion); for the 530d UAr analysis we assumed that ^{226}Ra was the parent of the lower chain.

The ^{238}U upper chain ($^{238}\mathrm{U}_{\mathrm{upper}}$) mostly produces low energy γ-rays; intensities of γ-rays $>$400 keV are low (topping out at 0.8% for the 1001 keV γ-ray from $^{234\mathrm{m}}$Pa).

The emitted γ-rays can result in single- or multiple- LAr scatters, and Cherenkov radiation in the fused silica volume.

The ^{238}U lower chain ($^{238}\mathrm{U}_{\mathrm{lower}}$) produces γ-rays with significant intensities (>1%) up to 2.5 MeV. These can result in single- or multiple- LAr scatters, and Cherenkov radiation in the fused silica or Teflon volumes.

3.2.2 Uranium-235

^{235}U is a primordial radionuclide, with a natural abundance of 0.72% and half-life of 7.0×10^8 yr [44]. The activity ratio with respect to ^{238}U is 0.046.

Germanium counting of ^{235}U looked for the 143 keV and 185 keV γ-rays from ^{235}U decay. The entire ^{235}U decay chain was assumed to be in secular equilibrium.

The ^{235}U decay chain mostly produces low energy γ-rays. High energy γ-rays (>1 MeV) can be produced by ^{215}Bi decay; however, its branching ratio is $1.38\% \times 0.006\% \times 97\% = 0.00008\%$. These can result in single- or multiple- LAr scatters, and Cherenkov radiation in the fused silica volume.

^{235}U can undergo spontaneous fission with a branching ratio of 2.011×10^{-9}, producing an average of 1.86 neutrons per decay that may then scatter in the TPC; α-decay in the ^{238}U decay chain is also a source of neutrons from subsequent (α, n) reactions [25].

3.2.3 Thorium-232

^{232}Th is a primordial radionuclide, with a natural abundance of 100% and half-life of 1.4×10^{10} yr [44]. It is present in soil with a median activity concentration of 30 Bq kg^{-1}, which varies with location [45, Annex B Tab. 5].

Since the half-life of its longest-living daughter (^{228}Ra) is 5.7 yr, it is reasonable to assume that the entire decay chain is in secular equilibrium.

The ^{232}Th decay chain produces γ-rays, which can result in single- or multiple-LAr scatters, and Cherenkov radiation in the fused silica or Teflon volumes. Notably, the 2.6 MeV γ-ray from ^{208}Tl decay was the highest energy γ-ray emitted by any of the main radioisotopes in DS-50.

^{232}Th can undergo spontaneous fission with a branching ratio of 1.4×10^{-11}, producing an average of 2.14 neutrons per decay that may then scatter in the TPC; α-decay in the ^{232}Th decay chain is also a source of neutrons from subsequent (α, n) reactions [25].

3.2.4 Potassium-40

^{40}K is a primordial radionuclide, with a natural abundance of 0.012% and half-life of 1.2×10^{9} yr [44]. It is present in soil with a median activity concentration of 400 Bq kg^{-1}, which varies with location [45, Annex B Tab. 5].

In DS-50, the resultant background was primarily from the 1.46 MeV γ-ray emitted in the decay of ^{40}K to ^{40}Ar via electron capture (10.72% branching ratio; it mostly undergoes β-decay). This can result in single- or multiple- LAr scatters, and Cherenkov radiation in the fused silica or Teflon volumes.

3.2.5 Cobalt-60

^{60}Co is a synthetic radioisotope with a half-life of 5.27 yr [44]. It is incidentally present in steel (despite having no utility therein), entering the manufacturing process in the form of contaminated scrap.

^{60}Co undergoes β-decay to ^{60}Ni. In DS-50, the resultant background was primarily from a pair of coincident 1.17 MeV and 1.33 MeV γ-rays emitted in the de-excitation of the ^{60}Ni. This can result in single- or multiple- LAr scatters, and Cherenkov radiation in the fused silica or Teflon volumes.

3.2.6 Krypton-85

^{85}Kr is a cosmogenic/anthropogenic radioisotope with a half-life of 10.7 yr [44], whose unexpected presence in the UAr was reported in [20]. The suspected source of this contamination was a leak to the atmosphere somewhere in the argon handling process.

^{85}Kr undergoes β-decay to ^{85}Rb. This produces β-particles (687 keV end-point), which are single-sited electron recoils in the LAr.

3.2.7 Argon-39

^{39}Ar is a naturally occurring radioisotope with a half-life of 269 yr [44]. It is produced from cosmic ray activation of ^{40}Ar, which explains its lower abundance in long-sequestered UAr [46]. A central part of the DarkSide program is the sourcing and extraction of such UAr; in particular, the UAr used to fill DS-50 was the product of a years-long effort to extract UAr from a CO_2 well in Cortez, Colorado [47].

^{39}Ar undergoes β-decay to ^{39}K. This produces β-particles (565 keV end-point), which are single-sited electron recoils in the LAr. Although the absolute abundance of ^{39}Ar in AAr is low (8.0×10^{-4} ppt$_{\mathrm{mass}}$), its measured activity is 1.01 Bq/kg$_{\mathrm{AAr}}$ [48], making it likely the most prevalent background in an AAr experiment [20, Fig. 1], and certainly the most problematic when scaling up the fiducial volume. In [20] we reported that the ^{39}Ar activity in the UAr was suppressed by a factor of 1.4×10^3 relative to that in AAr.

3.2.8 Argon-37

^{37}Ar is a cosmogenic radioisotope with a half-life of 35 d [44], whose unexpected presence in the UAr was reported in [20]. It could have contaminated the UAr via a leak to the atmosphere, or the cosmic-ray activation of a portion of the UAr that was transported to LNGS by air rather than by sea.

Because of its short half-life, ^{37}Ar was not a major background in the post-70d UAr analysis; its initial presence is reported here for completeness.

3.2.9 Radon daughters

Radon isotopes are produced in the ^{232}Th and ^{238}U$_{\text{lower}}$ chains. These are unstable radioisotopes, the longest-lived being ^{222}Rn with a half-life of 3.8 d [44]. Radon is gaseous and highly mobile, and thus the main mode of contamination to DS-50 came from the deposition of its daughter elements on the TPC's surfaces. These radon daughters included ^{210}Pb, which decays with a half-life of 22.2 yr [44] to α-emitting ^{210}Po. As mentioned in Sec. 3.1.2, such α-decay was a source of surface background. The radon-suppressed clean rooms in which the TPC components were prepared and assembled, and that housed DS-50's argon recirculation system, were crucial parts of the mitigation strategy for this source of background [23].

3.3 Estimating radioisotope activities

An extensive materials assay program was undertaken by the collaboration to characterize the radioactivity in the various detector components before deployment. The aim was to assay all cryostat and TPC components, including the TPC PMTs; however, because of the late-breaking need to deploy the R11065's instead of the R11065-20's, we ended up not having had the PMTs counted before their deployment.

Previous efforts that were undertaken to estimate the PMTs' radioactivity involved multi-dimensional fitting of the observed spectrum in the TPC. However, because of degeneracies between the spectra from the PMTs and from elsewhere (mostly the cryostat components), this was a complicated process. Thus, the round of work presented here was started with the aim of keeping the estimation tractable, by systematically setting plausible constraints on the various background rates in the

PMTs, and studying the implications. The estimates obtained here were subsequently used for normalizing the Monte Carlo (MC) simulations forming the basis of our ER background estimates.

3.3.1 Combined S1 and S2 energy variable

An energy variable reconstructed from a linear combination of S1 and S2 was used for making the radioactivity estimates. Briefly, the reconstruction of this variable involved the following:

1. The full deposition peaks of ^{83m}Kr, ^{37}Ar, and γ-rays from source calibration, in S2 *vs.* S1 phase-space, were found in data. Since most of the calibration γ's were of moderately high energy, resulting in events consisting of multiple argon scatters, this required specialized analysis distinct from that used for the WIMP search.

2. The observed S1 and S2 corresponding to the deposition energy E were then used as inputs for the following equation representing the partition of this energy into the scintillation and ionization components

$$\begin{aligned} E &= W(n_\gamma + n_{\text{ion}}) \\ &= W(\frac{\text{S1}}{\varepsilon_1} + \frac{\text{S2}}{\varepsilon_2}) \end{aligned} \tag{3.10}$$

   where W was the average energy required to produce an argon exciton or ion, n_γ was the number of scintillation photons produced from excitons or ion-electron recombination, n_{ion} was the number of ions produced from the Compton scattering that survived ion-electron recombination, and ε_1 and ε_2 were gain factors related to S1 and S2 respectively.

3. The preceding steps were repeated with data taken at different drift fields, which provided data points with different $n_\gamma : n_{\text{ion}}$ ratios, but the same ε_1 and ε_2 factors. ε_1 and ε_2 were then extracted from fits to these data points.

Since the energy variable reconstructed above is independent of the drift field, it was referred to as the "global energy" variable. [40, Ch. 3] should be consulted for greater detail.

3.3.2 Method

Activity estimates were derived by fitting energy spectra from Monte Carlo simulations against an energy spectrum from UAr data, following these steps:

1. Get the TPC energy spectra from Monte Carlo simulations of the various decay chains, in the various detector components (Fig. 3.1).[1]

2. Scale these simulated TPC energy deposits E with a quenching factor q to get the quenched energy E_{quench}:

$$E_{\text{quench}} = qE \tag{3.11}$$

   The quenching factor q was described by an empirical function, tuned such that the simulated γ-lines aligned with their corresponding peaks in the observed global energy spectrum E_{rec} [40, Sec. 3.5.2]:

$$q = E_{\text{rec}}/E = 0.9941 + 1.068 \times 10^{-5} \times E - 0.06507 \times e^{-E/300.9} \tag{3.12}$$

[1] In the course of this work, we discovered that v3.1 of the PhotonEvaporation table in Geant4 for ^{231}Th does not produce the 185.715 keV γ-ray from ^{235}U decay with the correct intensity (57% [44]). Consequently, PhotonEvaporation v2.3 (which gives the right intensity for this γ) is used to generate the spectrum for the ^{235}U chain instead. This issue has actually been resolved in more recent releases of PhotonEvaporation (*e.g.*, v4.3); however, such libraries were not compatible with our version of Geant4 (v10.00.p02) at the time.

3. Apply an empirical smearing to the quenched energy so that the simulated spectrum matches that expected from the study of the global energy variable. In particular, this was done by drawing E_{smear} from a Normal distribution with mean E_{quench} and variance σ^2, where

$$\sigma = E \times 0.01 \times (\sqrt{21.06 + 3585/E} - 3.313) \tag{3.13}$$

4. Fit the simulated E_{smear} spectra against the observed global energy spectrum from $200\,\text{V}\,\text{cm}^{-1}$ UAr data, with the radioisotope activities as the only free parameters. The data were selected with the following criteria: $\geq$2 pulses; drift time >10 µs; and 0.1<F90<0.5. There is minimal stress on the details of Monte Carlo simulations: working with energy bypasses the scintillation and optical modeling, and the $\geq$2 pulse requirement means the modeling of multiple S2 resolution is not an issue.

Figure 3.2 shows the result from one such example of this fitting.

3.3.3 Notes

Thorium, Uranium, Potassium, and Cobalt in the cryostat

These refer to radioisotopes in the cryostat body (142.2 kg of 5 mm stainless steel), flanges (two 15 kg annuli of 25 mm stainless steel), nuts (0.826 kg of steel), bolts (2.92 kg of steel), tubes (1.92 kg of steel), Viton o-ring, and 0.743 kg of multi-layer insulation (MLI).

Decays in the cryostat body, inner flange, and outer flange were simulated separately—Where the nuts, bolts, and tubes had significant activity, this was divided and equally accounted for as extra activity on each flange; Where the o-ring had significant activity, this was accounted for as extra activity on the outer flange;

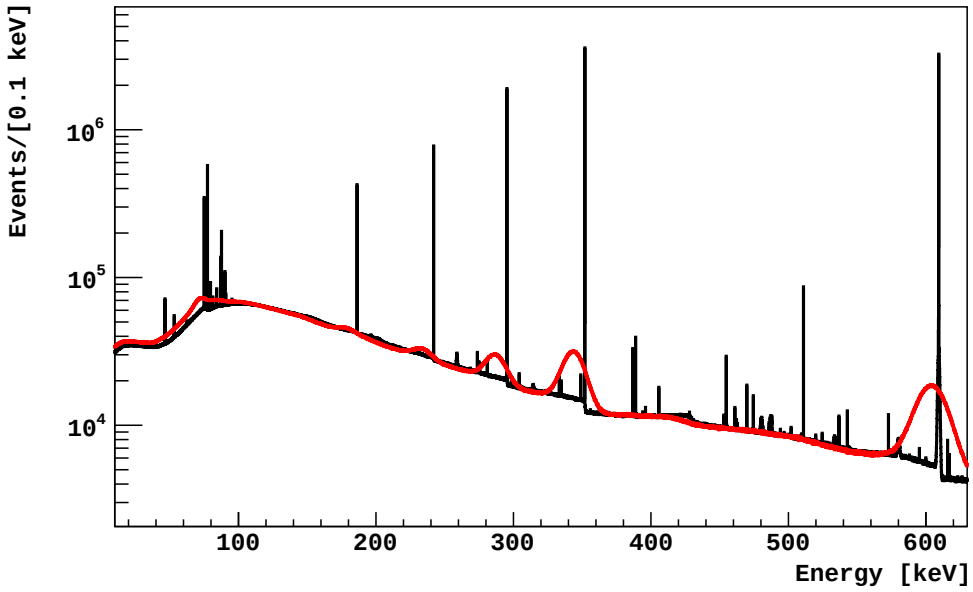

Figure 3.1: Simulated TPC energy spectrum from $^{238}U_{lower}$ in the PMT stem. Black: Before quenching and smearing; Red: After.

Where the MLI had significant activity, this was accounted for as extra activity on the cryostat body. The summed rate is referred to as the "cryostat" or "cryo" rate.

We note that for the discussed cryostat components, either the actual fabrication materials, or the consignments of components themselves, were assayed—either with germanium spectroscopy, glow discharge mass spectroscopy (GDMS), or inductively coupled plasma mass spectrometry (ICP-MS). The results from these measurements are presented in Tab. 3.1; radioisotope activities in the cryostat components were fixed at these rates in the fitting process.

The uncertainties in Tab. 3.1 were taken as upper/lower bounds on the respective activities. Figure 3.3 shows that taking all of these upper limits together does not account for the rate observed in the data spectrum; thus, activity from the PMTs or LAr is necessary to make up the difference.

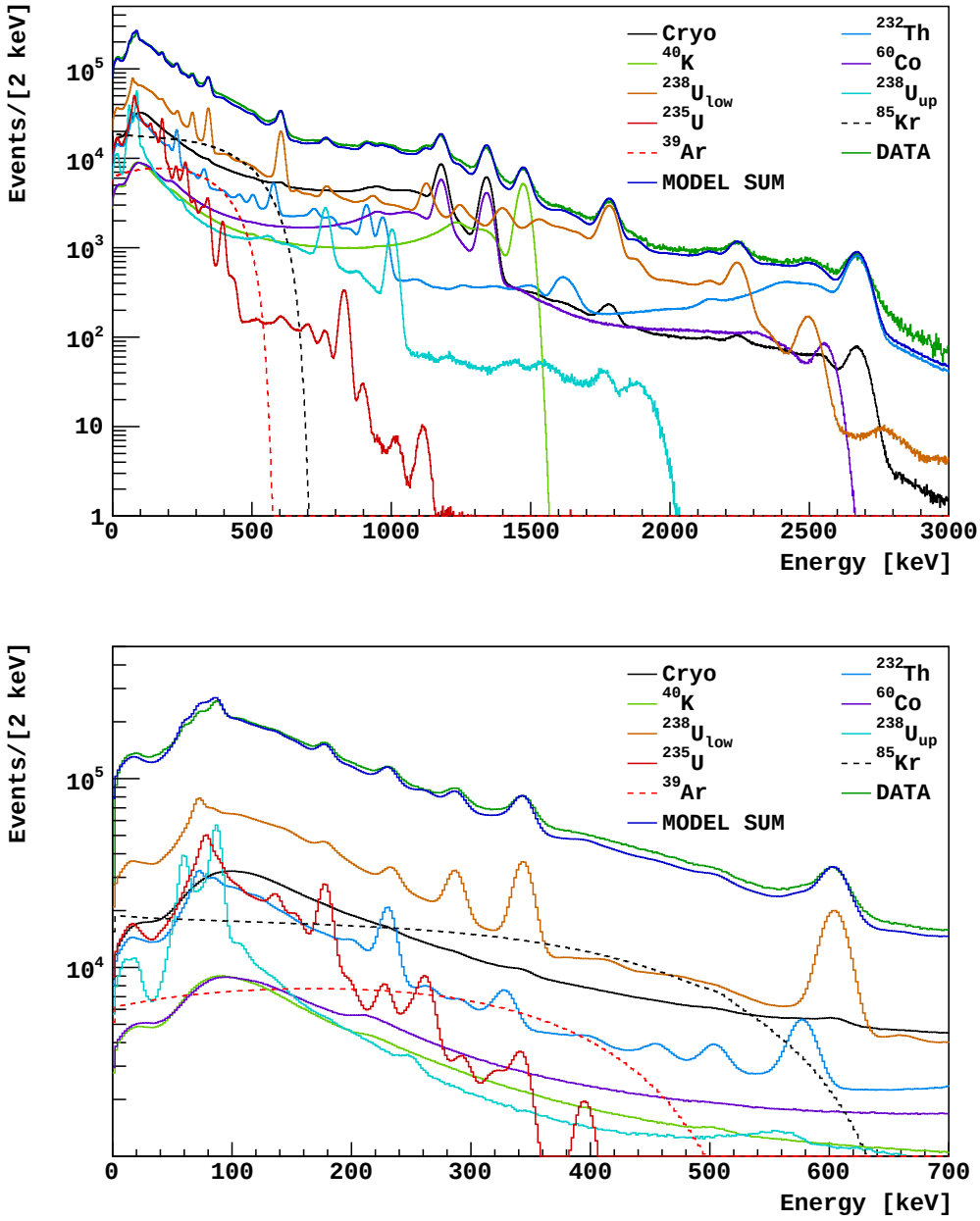

Figure 3.2: Output from the energy spectrum fitting. Since the actual cryostat materials were assayed, the radioisotope activities in the various cryostat components were fixed at the measured rates. However, because none of the PMTs used for counting were deployed, PMT radioisotope activities were free parameters in the fit. ^{39}Ar and ^{85}Kr activities were fixed in accordance with the measured rates reported in [20].

Table 3.1: Radioisotope activity in various cryostat components from materials assay. If a measured activity is an upper limit, no positive uncertainty/100% negative uncertainty is appended. If measured activity is not an upper limit, $1\,\sigma$ uncertainty is appended (in this case, uncertainty on GDMS measurements is 20%, based on information from the vendor). Presented ^{60}Co activity is the average for the UAr exposure presented in this work; assay of the steel was done about 3.5 yr prior to this. ICP-MS does not directly measure $^{238}U_{lower}$—where such a rate is reported, secular equilibrium in the entire ^{238}U chain is assumed; we note that assuming no $^{238}U_{lower}$ activity in the multi-layer insulation instead raises the estimated rate of $^{238}U_{lower}$ in the PMT by ∼2%.

	Rates [Bq]			
	Cryostat	I-flan	O-flan	Remarks
^{60}Co	1.2±0.1	0.11±0.01	0.11±0.01	**Cryostat:** 5 mm steel (Ge) **I-flan/O-flan:** 25 mm steel (Ge)
^{40}K	<0.004	<0.027	$0.13^{+0.02}_{-0.05}$	**Cryostat:** 5 mm steel (GDMS UL) **I-flan/O-flan:** 25 mm steel (Ge UL) **O-flan:** Viton o-ring (Ge)
^{232}Th	0.05±0.01	0.05±0.01	$0.09^{+0.01}_{-0.02}$	**Cryostat:** 5 mm steel (GDMS) **I-flan/O-flan:** Bolts (Ge/GDMS), Nuts (Ge UL), 25 mm steel (Ge/GDMS) **O-flan:** Viton o-ring (Ge)
^{235}U	0.015±0.003	$0.013^{+0.002}_{-0.007}$	$0.018^{+0.002}_{-0.012}$	**Cryostat:** 5 mm steel (GDMS) **I-flan/O-flan:** 25 mm steel (GDMS), Tubes (Ge UL) **O-flan:** Viton o-ring (Ge UL)
$^{238}U_{upper}$	0.35±0.07	$0.35^{+0.05}_{-0.15}$	$0.57^{+0.05}_{-0.37}$	**Cryostat:** 5 mm steel (GDMS) **I-flan/O-flan:** 25 mm steel (GDMS), Tubes (Ge UL), Bolts (GDMS) **O-flan:** Viton o-ring (Ge UL)
$^{238}U_{lower}$	$0.13^{+0.03}_{-0.10}$	$0.021^{+0.001}_{-0.020}$	$0.23^{+0.01}_{-0.03}$	(Not measured by GDMS) **Cryostat:** 5 mm steel (Ge), MLI (ICP-MS) **I-flan/O-flan:** Bolts (Ge), 25 mm steel (Ge UL), Nuts (Ge UL) **O-flan:** Viton o-ring (Ge)

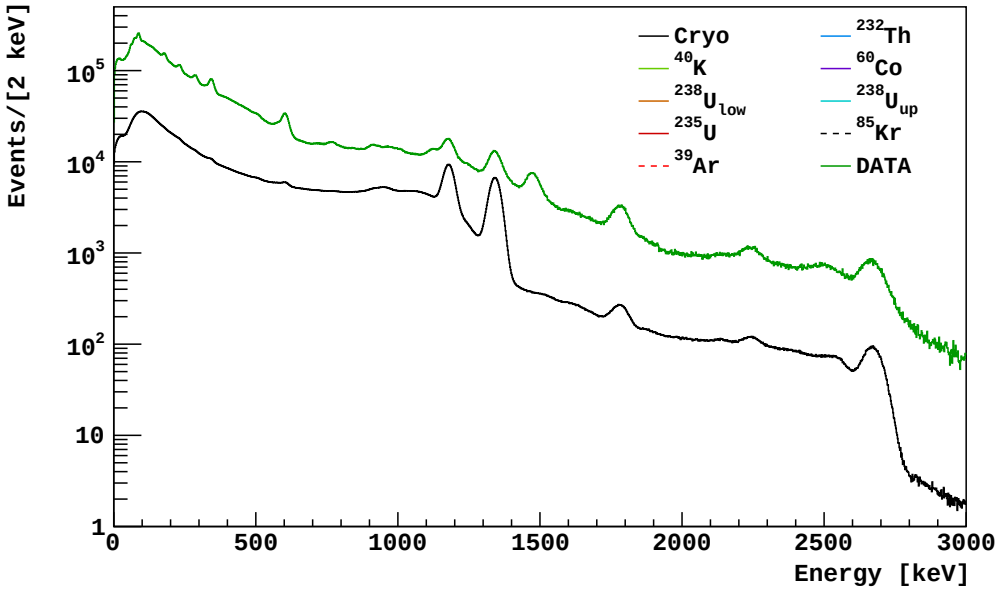

Figure 3.3: Simulated energy spectrum in the TPC from radioisotope activity in the cryostat, each with a $1\,\sigma$ uncertainty added.

Thorium, Uranium lower chain, Potassium, and Cobalt in the PMTs

These decay chains have peaks unique to their spectra—2.6 MeV from ^{208}Tl, 1.76 MeV from ^{214}Bi, 1.46 MeV from ^{40}K, and 1.33 MeV from ^{60}Co, respectively—that were readily identified in the data spectrum.

The main sources of radioactivity in the PMTs were the borosilicate glass stem at the back of the PMT, the ceramic insulators supporting the dynodes inside the PMT, and the Kovar casing of the PMT. From the assay of various models of R11065 PMTs, a Kovar casing, and a sample of the ceramic insulators, the distribution of various backgrounds across these PMT locations were inferred [49]; these are presented in Tab. 3.2. "PMT" rates are the summed rates over all of these PMT components, reflecting this distribution of activities within the PMTs, and across all 38 PMTs.[2]

[2] This work was initially done with a simulated PMT geometry that consisted of only vacuum within the Kovar casing. This allowed βs from activity in the stem (notably, from ^{238}U$_{\text{upper}}$) to easily impinge upon the PMT windows, and produce a tremendous excess of Cherenkov radiation (unaccompanied by scintillation) therein. This problem was caught in comparisons against the 1-pulse, high F90 S1 spectrum in data. We note that reasonable fits and rates for the various backgrounds

Table 3.2: Fractional distribution of radioisotope activities across the various PMT components.

	Ceramic	Stem	Kovar		Ceramic	Stem	Kovar
^{60}Co	0	0	1	^{235}U	0.8	0.2	0
^{40}K	0.2	0.8	0	$^{238}\mathrm{U}_{\mathrm{upper}}$	0.8	0.2	0
^{232}Th	0.3	0.7	0	$^{238}\mathrm{U}_{\mathrm{lower}}$	0.5	0.5	0

3.3.4 Estimating radioisotope activities in the PMTs

As mentioned in Sec. 3.3.3, the cryostat activities were anchored to their respective activities as determined by the material assays. In addition, ^{85}Kr and ^{39}Ar activities were fixed in accordance with their measured rates as reported in [20], with ^{85}Kr decay in the intervening time accounted for. PMT activities were then obtained using the following procedure (steps are cumulative):

1. **^{232}Th:** With the cryostat radioisotope activities fixed at their measured rates as shown in Tab. 3.1, fit about the ^{208}Tl peak (2.65-2.75 MeV) with the $^{232}\mathrm{Th}_{\mathrm{PMT}}$ rate as a free parameter.

2. **$^{238}\mathrm{U}_{\mathrm{lower}}$:** With $^{232}\mathrm{Th}_{\mathrm{PMT}}$ fixed at the rate estimated from the previous step, also fix $^{60}\mathrm{Co}_{\mathrm{PMT}}$ at $\sim$0.15 Bq. Here we are anticipating the estimated activity for $^{60}\mathrm{Co}_{\mathrm{PMT}}$; this is necessary because $^{60}\mathrm{Co}_{\mathrm{PMT}}$ accounts for a substantial amount of the activity in our fitting range. We arrived at our "guess" through manual iteration. Fit about the ^{214}Bi peak (1.75-1.85 MeV) with the $^{238}\mathrm{U}^{\mathrm{lower}}_{\mathrm{PMT}}$ rate as a free parameter.

3. **^{40}K:** With $^{238}\mathrm{U}^{\mathrm{lower}}_{\mathrm{PMT}}$ fixed at the rate estimated from the previous step, fit about the ^{40}K peak (1.45-1.55 MeV) with the $^{40}\mathrm{K}_{\mathrm{PMT}}$ rate as a free parameter.

4. **^{60}Co:** With $^{40}\mathrm{K}_{\mathrm{PMT}}$ fixed at the rate estimated from the previous step, fit about the ^{60}Co peak (1.3-1.4 MeV) with the $^{60}\mathrm{Co}_{\mathrm{PMT}}$ rate as a free parameter.

were obtained despite this simplistic modeling of the PMTs, indicating that our spectrum fitting scheme is insensitive to such variations.

Table 3.3: Radioisotope activities obtained by fitting $^{232}\mathrm{Th}_{\mathrm{PMT}}$, $^{238}\mathrm{U}^{\mathrm{lower}}_{\mathrm{PMT}}$, $^{40}\mathrm{K}_{\mathrm{PMT}}$, and $^{60}\mathrm{Co}_{\mathrm{PMT}}$ in sequence, followed by $^{235}\mathrm{U}_{\mathrm{PMT}}$ and $^{238}\mathrm{U}^{\mathrm{upper}}_{\mathrm{PMT}}$ simultaneously. Cryostat activities were fixed at their respective rates as determined by the material assays; ^{85}Kr and ^{39}Ar rates were fixed in accordance with their measured rates as reported in [20]. Presented PMT rates are for all 38 tubes combined.

Background	Rate [Bq]	Background	Rate [Bq]
$^{60}\mathrm{Co}_{\mathrm{PMT}}$	0.149	$^{60}\mathrm{Co}_{\mathrm{cryo}}$	1.375
$^{40}\mathrm{K}_{\mathrm{PMT}}$	2.738	$^{40}\mathrm{K}_{\mathrm{cryo}}$	0.159
$^{232}\mathrm{Th}_{\mathrm{PMT}}$	0.277	$^{232}\mathrm{Th}_{\mathrm{cryo}}$	0.192
$^{235}\mathrm{U}_{\mathrm{PMT}}$	0.194	$^{235}\mathrm{U}_{\mathrm{cryo}}$	0.045
$^{238}\mathrm{U}^{\mathrm{upper}}_{\mathrm{PMT}}$	4.177	$^{238}\mathrm{U}^{\mathrm{upper}}_{\mathrm{cryo}}$	1.269
$^{238}\mathrm{U}^{\mathrm{lower}}_{\mathrm{PMT}}$	0.844	$^{238}\mathrm{U}^{\mathrm{lower}}_{\mathrm{cryo}}$	0.378
^{85}Kr [/kg]	0.0019	^{39}Ar [/kg]	0.00073

5. **^{235}U and $^{238}\mathrm{U}_{\mathrm{upper}}$:** With $^{60}\mathrm{Co}_{\mathrm{PMT}}$ fixed at its best fit rate, fit simultaneously over 50-1000 keV; the rates for $^{235}\mathrm{U}_{\mathrm{PMT}}$ and $^{238}\mathrm{U}^{\mathrm{upper}}_{\mathrm{PMT}}$ are fit as one parameter to conserve their natural abundance ratio.

These estimated decay chain activities are summarized in Tab. 3.3, the resulting spectrum is shown in Fig. 3.2. We note that the uncertainties on these estimated rates from the fitting process are all <1%, which are much smaller than the uncertainties we will set in Sec. 3.3.5.

3.3.5 Establishing upper and lower limits

Thorium, Uranium lower chain, Potassium, and Cobalt in the PMTs

Upper limits (UL) on $^{232}\mathrm{Th}_{\mathrm{PMT}}$, $^{238}\mathrm{U}^{\mathrm{lower}}_{\mathrm{PMT}}$, $^{40}\mathrm{K}_{\mathrm{PMT}}$, and $^{60}\mathrm{Co}_{\mathrm{PMT}}$ activity were estimated in separate procedures, each involving a fit of the spectrum under considerations about the peak unique to it, while fixing the activity of other radioisotopes as prescribed below:

- **^{232}Th:** All cryostat activities were fixed at their lower limits (LL) as reported in Tab. 3.1; All other (*i.e.*, non-$^{232}\mathrm{Th}_{\mathrm{PMT}}$) activities were fixed at 0 Bq. The

UL on $^{232}\mathrm{Th}_{\mathrm{PMT}}$ activity was then obtained by fitting about the ^{208}Tl peak (2.65-2.75 MeV).

Given the fitting range, the only fixed spectrum with any impact on the UL estimate was that of $^{232}\mathrm{Th}_{\mathrm{cryo}}$, the summed contribution from all cryostat components as noted in Tab. 3.1. We used a simple sum of the presented LLs instead of a more sophisticated treatment (*e.g.*, summing uncertainties in quadrature), which gave an overestimate of the uncertainty; however, the estimated $^{232}\mathrm{Th}_{\mathrm{PMT}}$ UL with this treatment was already tolerably small anyway (Tab. 3.4).

- $^{238}\mathbf{U_{lower}}$**:** All cryostat activities were fixed at their LLs; $^{232}\mathrm{Th}_{\mathrm{PMT}}$ and $^{60}\mathrm{Co}_{\mathrm{PMT}}$ activities were fixed at their respective best fit rates as presented in Tab. 3.3; All other activities were fixed at 0 Bq. The UL on $^{238}\mathrm{U}^{\mathrm{lower}}_{\mathrm{PMT}}$ activity was then obtained by fitting about the ^{214}Bi peak (1.75-1.85 MeV).

  In principle the effect of variations in $^{238}\mathrm{U}_{\mathrm{lower}}/^{232}\mathrm{Th}/^{60}\mathrm{Co}$ activity in both the cryostat and PMTs should be studied, as Fig. 3.2 indicates significant contributions from these decay chains in the fitting range. We note that fixing the cryostat activities at their LLs returned a (slightly) higher UL estimate than fixing either the $^{232}\mathrm{Th}_{\mathrm{PMT}}$ or $^{60}\mathrm{Co}_{\mathrm{PMT}}$ activities at their respective LLs instead. We decided that fixing all three activities (cryostat, $^{232}\mathrm{Th}_{\mathrm{PMT}}$, and $^{60}\mathrm{Co}_{\mathrm{PMT}}$) at their LLs for this estimation would be too conservative.

- ^{40}**K:** All cryostat activities were fixed at their LLs; $^{232}\mathrm{Th}_{\mathrm{PMT}}$, $^{238}\mathrm{U}^{\mathrm{lower}}_{\mathrm{PMT}}$, and $^{60}\mathrm{Co}_{\mathrm{PMT}}$ activities were fixed at their respective best fit rates; All other activities were fixed at 0 Bq. The UL on $^{40}\mathrm{K}_{\mathrm{PMT}}$ activity was then obtained by fitting about the ^{40}K peak (1.45-1.55 MeV).

  We note that although $^{238}\mathrm{U}^{\mathrm{lower}}_{\mathrm{PMT}}$ (apart from $^{40}\mathrm{K}_{\mathrm{PMT}}$) contributed most to the spectrum in the fitting range (Fig. 3.2), the absolute uncertainty on the cryostat rates was actually the largest, and hence fixing the cryostat activities at their

LLs returned a higher UL estimate than fixing any one of the PMT activities at their respective LLs instead.

- **^{60}Co:** All cryostat activities were fixed at their LLs; $^{232}\mathrm{Th}_{\mathrm{PMT}}$, $^{238}\mathrm{U}^{\mathrm{lower}}_{\mathrm{PMT}}$, and $^{40}\mathrm{K}_{\mathrm{PMT}}$ activities were fixed at their respective best fit rates; All other activities were fixed at 0 Bq. The UL on $^{60}\mathrm{Co}_{\mathrm{PMT}}$ activity was then obtained by fitting about one of the ^{60}Co peaks (1.3-1.4 MeV).

  Figure 3.2 shows that $^{60}\mathrm{Co}_{\mathrm{cryo}}$ was the largest contributor to the 1.33 MeV peak apart from $^{60}\mathrm{Co}_{\mathrm{PMT}}$. $^{60}\mathrm{Co}_{\mathrm{cryo}}$ also had fairly large uncertainties (Tab. 3.1). Thus, a $-1\,\sigma$ fluctuation in $^{60}\mathrm{Co}_{\mathrm{cryo}}$ was a well-founded variation for setting a corresponding UL on $^{60}\mathrm{Co}_{\mathrm{PMT}}$.

The results from the UL fitting are shown in Fig. 3.4 and Tab. 3.4.

Lower limits on the activities of $^{232}\mathrm{Th}_{\mathrm{PMT}}$, $^{238}\mathrm{U}^{\mathrm{lower}}_{\mathrm{PMT}}$, $^{40}\mathrm{K}_{\mathrm{PMT}}$, and $^{60}\mathrm{Co}_{\mathrm{PMT}}$ were obtained with the following procedure (steps are cumulative):

1. **^{232}Th:** With the cryostat activities fixed at their ULs, and all other (*i.e.*, non-$^{232}\mathrm{Th}_{\mathrm{PMT}}$) activities fixed at 0 Bq, the LL on $^{232}\mathrm{Th}_{\mathrm{PMT}}$ activity was obtained by fitting about the ^{208}Tl peak (2.65-2.75 MeV).

2. **$^{238}\mathrm{U}_{\mathrm{lower}}$:** With the $^{232}\mathrm{Th}_{\mathrm{PMT}}$ activity fixed at its LL as obtained in the previous step, and $^{60}\mathrm{Co}_{\mathrm{PMT}}$ activity fixed at its best fit rates (Tab. 3.3), the LL on $^{238}\mathrm{U}^{\mathrm{lower}}_{\mathrm{PMT}}$ activity was obtained by fitting about the ^{214}Bi peak (1.75-1.85 MeV).

3. **^{40}K:** With the $^{238}\mathrm{U}^{\mathrm{lower}}_{\mathrm{PMT}}$ activity fixed at its LL as obtained in the previous step, the LL on $^{40}\mathrm{K}_{\mathrm{PMT}}$ activity was obtained by fitting about the ^{40}K peak (1.45-1.55 MeV).

4. **^{60}Co:** With the $^{40}\mathrm{K}_{\mathrm{PMT}}$ activity fixed at its LL as obtained in the previous step, the LL on $^{60}\mathrm{Co}_{\mathrm{PMT}}$ activity was obtained by fitting about the 1.3 MeV ^{60}Co peak (1.3-1.4 MeV).

Table 3.4: Comparison of PMT rates from energy spectrum fits against measured PMT rates (latter with measurement uncertainties). ^{60}Co decay since the PMTs had their rates counted has been accounted for. Measured ^{39}Ar and ^{85}Kr rates are from the 70d UAr analysis [20].

Background	Best fit rate [Bq]	UL rate [Bq]	LL rate [Bq]	Meas Rate [Bq]
$^{60}\mathrm{Co}_{\mathrm{PMT}}$	0.15	0.17	0.13	0.20±0.02
$^{40}\mathrm{K}_{\mathrm{PMT}}$	2.74	2.80	2.73	3.00±0.42
$^{232}\mathrm{Th}_{\mathrm{PMT}}$	0.277	0.282	0.272	0.23±0.04
$^{235}\mathrm{U}_{\mathrm{PMT}}$	0.19	0.20	0.17	0.27±0.02
$^{238}\mathrm{U}^{\mathrm{upper}}_{\mathrm{PMT}}$	4.18	4.26	3.62	5.72±0.42
$^{238}\mathrm{U}^{\mathrm{lower}}_{\mathrm{PMT}}$	0.84	0.87	0.83	0.69±0.02
^{85}Kr [/kg]	-	-	-	0.0019±0.0001
^{39}Ar [/kg]	-	-	-	0.0007±0.0001

The results from this fitting are shown in Fig. 3.5 and Tab. 3.4. In particular, the choice to set the cryostat rates at their ULs—and hence capping the respective PMT rates at their LLs (to conserve total activity at the high energy peaks)—was made as it returned lower LLs on the various PMT rates under consideration.

We note that overly conservative upper and lower bounds on the background activities—*i.e.*, ones assuming or allowing for wild variations in the rates—were found to be not particularly useful, as these did not allow us to perform meaningful testing of our background predictions.

Uranium-238 upper chain and Uranium-235 in the PMTs

Upper (lower) limits on $^{238}\mathrm{U}^{\mathrm{upper}}_{\mathrm{PMT}}$ and $^{235}\mathrm{U}_{\mathrm{PMT}}$ activities were obtained by fitting with one free parameter (to conserve their natural abundance ratio) over 50-200 keV, while cryostat activities were fixed at their LLs (ULs), all other PMT activities were fixed to their best fit rates, and ^{85}Kr and ^{39}Ar activities were fixed at their measured rates as reported in [20]. The results from these fits are shown in Fig. 3.6 and Tab. 3.4.

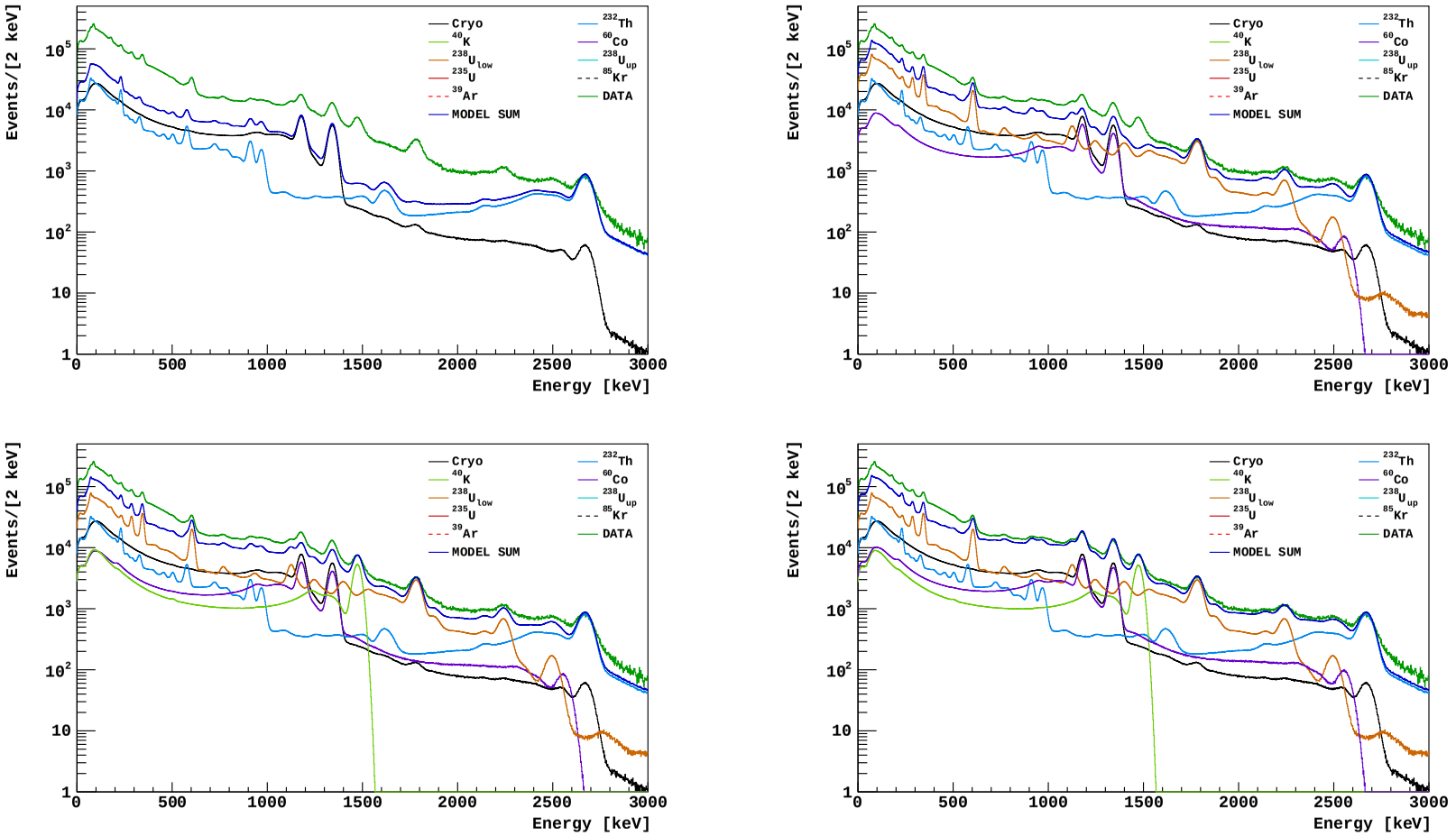

Figure 3.4: Fits of individual PMT decay chains against peaks unique to their respective spectra, to obtain upper limits on their activities. (Top left) $^{232}\mathrm{Th}_{\mathrm{PMT}}$; (Top right) $^{238}\mathrm{U}^{\mathrm{lower}}_{\mathrm{PMT}}$; (Bottom left) $^{40}\mathrm{K}_{\mathrm{PMT}}$; (Bottom right) $^{60}\mathrm{Co}_{\mathrm{PMT}}$.

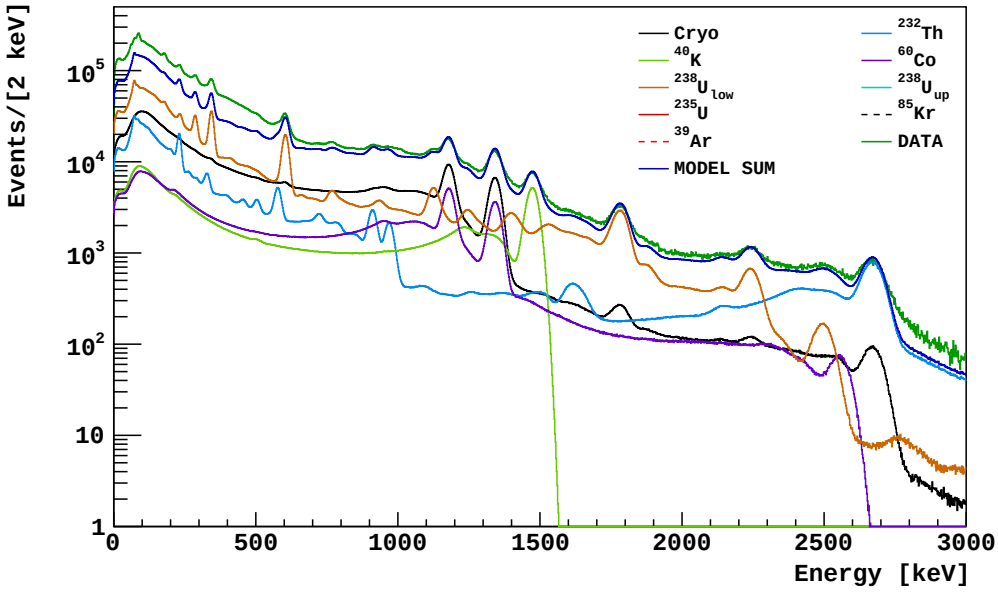

Figure 3.5: Fit to obtain lower limits on activities of $^{232}\mathrm{Th}_{\mathrm{PMT}}$, $^{238}\mathrm{U}^{\mathrm{lower}}_{\mathrm{PMT}}$, $^{40}\mathrm{K}_{\mathrm{PMT}}$, and $^{60}\mathrm{Co}_{\mathrm{PMT}}$. Cryostat activities are fixed at their upper limits throughout; this necessitates fixing the PMT rates at their respective lower limits as they are obtained, to conserve total activity at the high energy peaks.

3.3.6 Discussion

Tables 3.1 and 3.4 indicate that uncertainties on the potential Cherenkov-inducing backgrounds (^{232}Th, $^{238}\mathrm{U}_{\mathrm{lower}}$, ^{40}K, ^{60}Co) were tolerable—topping out at about +16% for ^{232}Th in the cryostat.

Since the eventual goal was to propagate the rate uncertainties to the background prediction, we used the ER background model (to be described in Ch. 5) to study the impact of using the estimated upper and lower limits on predicted event counts in the WIMP-search F90 *vs.* S1 box used in [20]. Table 3.5 summarizes the predicted box event counts using the best fit, UL and LL rates for normalization, in 500 d of UAr running, and passing a 40 µs drift time fiducialization and the S1 prompt maximum fraction cut (S1pmf; see Ch. 4 for details). The event counts in Tab. 3.5 have been broken down into various categories: single LAr scatter only, unresolved multiple LAr

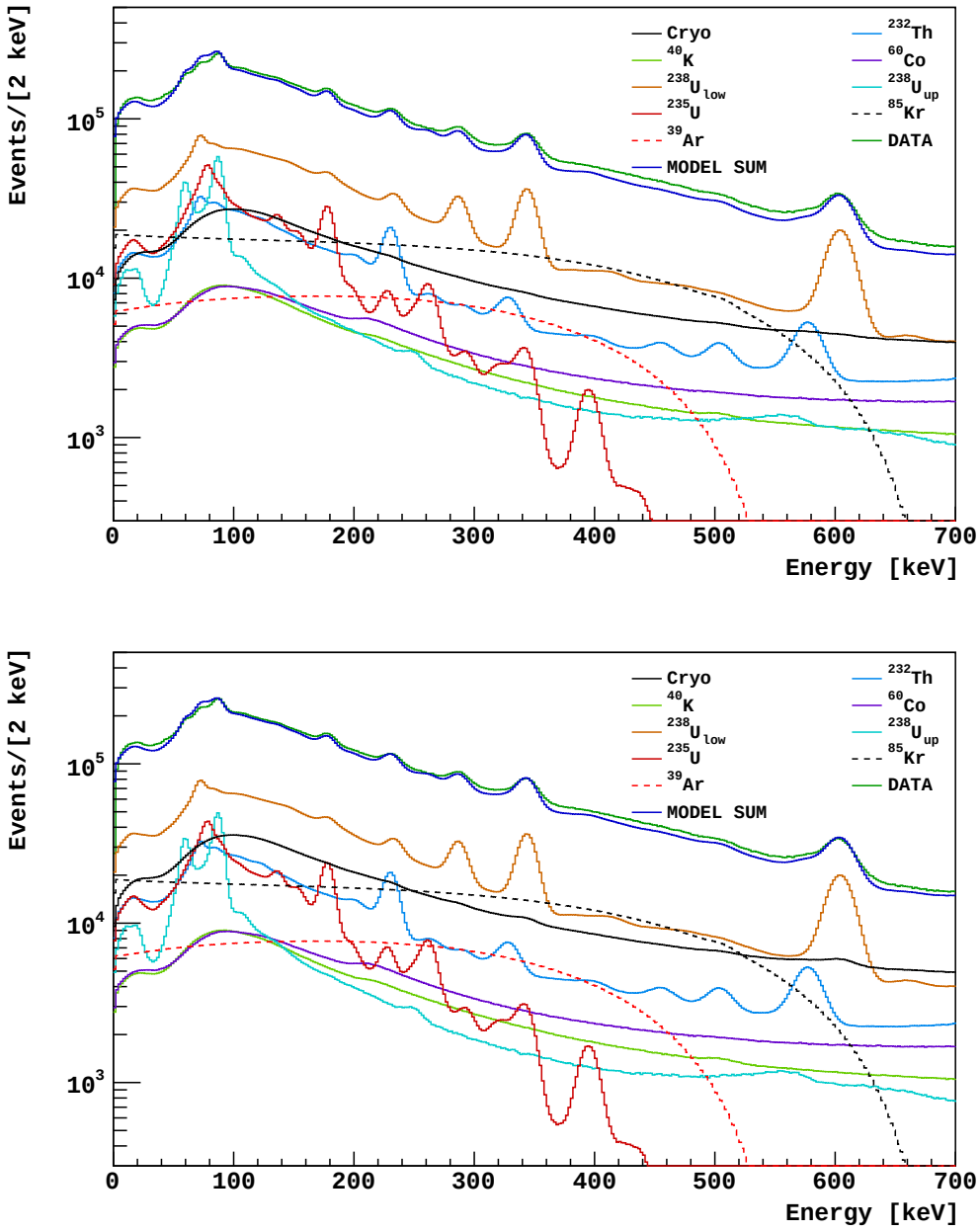

Figure 3.6: **Top:** Upper limit fit for $^{238}\mathrm{U}^{\mathrm{upper}}_{\mathrm{PMT}}$ and $^{235}\mathrm{U}_{\mathrm{PMT}}$; **Bottom:** Lower limit fit for $^{238}\mathrm{U}^{\mathrm{upper}}_{\mathrm{PMT}}$ and $^{235}\mathrm{U}_{\mathrm{PMT}}$.

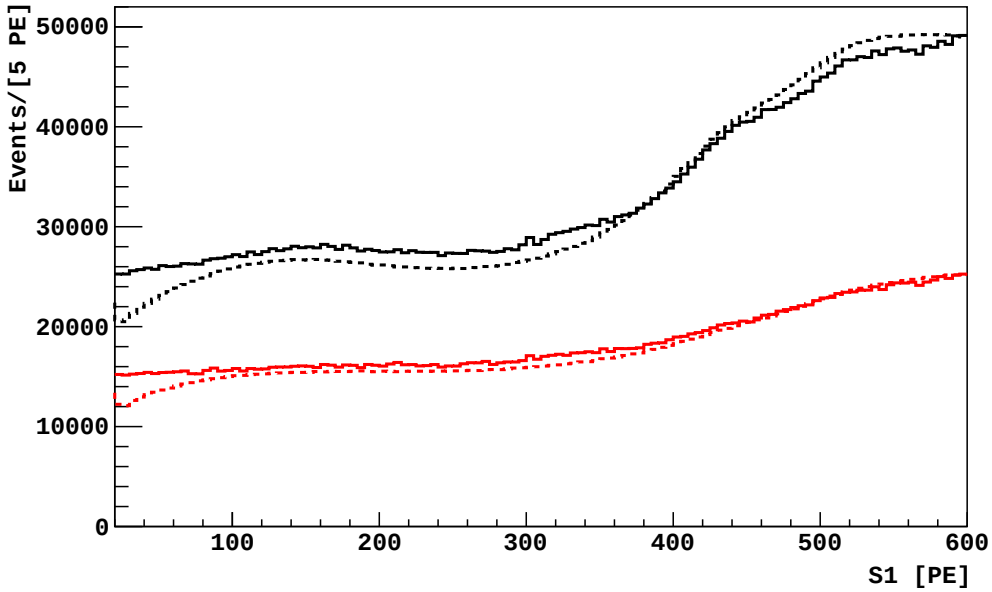

Figure 3.7: 530d UAr data (solid) and modeled (dashed) S1 spectra of 2-pulse events passing the S1 prompt maximum fraction cut, with 10 µs (black) and 40 µs (red) drift time fiducialization. The model consists of simulated events from decay chains and detector locations described in this chapter, normalized using the best fit rates.

scatters only, scintillation with Teflon Cherenkov only, scintillation with fused silica Cherenkov only, and scintillation with Cherenkov in both Teflon and fused sillica only.

The predicted event counts indicated that using the upper limit activities for every radioisotope considered in this chapter resulted in only a +5% change in total predicted background; conversely, using all the lower limits resulted in a −4% change. In particular, we expected larger uncertainties on the background prediction to come from elsewhere, and so these were very tolerable.

Figure 3.7 shows the 530d UAr data and modeled S1 spectra of two-pulse events passing the S1pmf cut, with 10 µs and 40 µs fiducial cuts applied. We see that the model underestimated the event rates for S1<400 PE by <10%.

Table 3.5: Predicted box event counts using the best fit, UL and LL rates for normalization, in 500 d of UAr running, and passing a 40 µs drift time fiducialization, the S1 prompt maximum fraction cut, and $60 < \mathrm{S1} < 300$. The MC event statistics are high—equivalent to >10000 d worth.

	PMT						Cryo						LAr		
Event type	^{232}Th	^{238}U$_{\mathrm{low}}$	^{40}K	^{60}Co	^{238}U$_{\mathrm{up}}$	^{235}U	^{232}Th	^{238}U$_{\mathrm{low}}$	^{40}K	^{60}Co	^{238}U$_{\mathrm{up}}$	^{235}U	^{39}Ar	^{85}Kr	Total
	Best fit rates														
1-sctr	0.0	0.0	0.0	0.0	0.0	0.0	0.0	0.0	0.0	0.0	0.0	0.0	0.0	0.0	0.1
>1-sctr	0.0	0.0	0.0	0.0	0.0	0.0	0.0	0.0	0.0	0.0	0.0	0.0	0.0	0.0	0.0
+Tef	11.5	7.8	0.4	0.1	0.1	0.0	1.6	0.6	0.0	0.2	0.0	0.0	0.0	0.0	22.4
+FS	0.4	0.3	0.0	0.1	0.0	0.0	0.0	0.0	0.0	0.0	0.0	0.0	0.0	0.0	0.8
+Tef+FS	0.2	0.1	0.0	0.0	0.0	0.0	0.0	0.0	0.0	0.0	0.0	0.0	0.0	0.0	0.3
	UL rates														
1-sctr	0.0	0.0	0.0	0.0	0.0	0.0	0.0	0.0	0.0	0.0	0.0	0.0	0.0	0.0	0.1
>1-sctr	0.0	0.0	0.0	0.0	0.0	0.0	0.0	0.0	0.0	0.0	0.0	0.0	0.0	0.0	0.0
+Tef	11.7	8.1	0.4	0.1	0.1	0.0	2.0	0.7	0.0	0.2	0.0	0.0	0.0	0.0	23.4
+FS	0.4	0.3	0.0	0.1	0.0	0.0	0.0	0.0	0.0	0.0	0.0	0.0	0.0	0.0	0.9
+Tef+FS	0.2	0.1	0.0	0.0	0.0	0.0	0.0	0.0	0.0	0.0	0.0	0.0	0.0	0.0	0.4
	LL rates														
1-sctr	0.0	0.0	0.0	0.0	0.0	0.0	0.0	0.0	0.0	0.0	0.0	0.0	0.0	0.0	0.1
>1-sctr	0.0	0.0	0.0	0.0	0.0	0.0	0.0	0.0	0.0	0.0	0.0	0.0	0.0	0.0	0.0
+Tef	11.2	7.7	0.4	0.1	0.1	0.0	1.3	0.2	0.0	0.2	0.0	0.0	0.0	0.0	21.3
+FS	0.4	0.3	0.0	0.1	0.0	0.0	0.0	0.0	0.0	0.0	0.0	0.0	0.0	0.0	0.8
+Tef+FS	0.2	0.1	0.0	0.0	0.0	0.0	0.0	0.0	0.0	0.0	0.0	0.0	0.0	0.0	0.3
	Best fit rates, Passing veto prompt and 0.84 veto delayed acceptance														
1-sctr	0.0	0.0	0.0	0.0	0.0	0.0	0.0	0.0	0.0	0.0	0.0	0.0	0.0	0.0	0.0
>1-sctr	0.0	0.0	0.0	0.0	0.0	0.0	0.0	0.0	0.0	0.0	0.0	0.0	0.0	0.0	0.0
+Tef	4.2	5.3	0.3	0.0	0.0	0.0	0.4	0.4	0.0	0.1	0.0	0.0	0.0	0.0	10.7
+FS	0.2	0.2	0.0	0.0	0.0	0.0	0.0	0.0	0.0	0.0	0.0	0.0	0.0	0.0	0.4
+Tef+FS	0.1	0.0	0.0	0.0	0.0	0.0	0.0	0.0	0.0	0.0	0.0	0.0	0.0	0.0	0.2

Table 3.6: 70d UAr analysis radioisotope activities, obtained with the procedure described in Sec. 3.3.4.

Background	Rate [Bq]	Background	Rate [Bq]
$^{60}\mathrm{Co}_{\mathrm{PMT}}$	0.179	$^{60}\mathrm{Co}_{\mathrm{cryo}}$	1.515
$^{40}\mathrm{K}_{\mathrm{PMT}}$	2.781	$^{40}\mathrm{K}_{\mathrm{cryo}}$	0.159
$^{232}\mathrm{Th}_{\mathrm{PMT}}$	0.268	$^{232}\mathrm{Th}_{\mathrm{cryo}}$	0.192
$^{235}\mathrm{U}_{\mathrm{PMT}}$	0.214	$^{235}\mathrm{U}_{\mathrm{cryo}}$	0.045
$^{238}\mathrm{U}^{\mathrm{upper}}_{\mathrm{PMT}}$	4.604	$^{238}\mathrm{U}^{\mathrm{upper}}_{\mathrm{cryo}}$	1.269
$^{238}\mathrm{U}^{\mathrm{lower}}_{\mathrm{PMT}}$	0.837	$^{238}\mathrm{U}^{\mathrm{lower}}_{\mathrm{cryo}}$	0.378
^{85}Kr [/kg]	0.0020	^{39}Ar [/kg]	0.00073

3.3.7 70d UAr analysis rates

The procedure described above was also used to estimate radioisotope activities for the 70d UAr analysis, where notably a higher $^{60}\mathrm{Co}_{\mathrm{cryo}}$ rate was used. Summaries of these rates, and the projected 70d UAr event count in the 70d UAr box, are shown in Tab. 3.6 and Tab. 3.7. We note that the predicted ER background count of 1.6 (after accounting for veto cuts) is compatible with the actual observation of 0 background events.

Table 3.7: Predicted box event counts using the best fit rates for normalization, in 70 d of UAr running, and passing a 40 µs drift time fiducialization, the S1 prompt maximum fraction cut, and $60 < \text{S1} < 300$. The MC event statistics are high—equivalent to >10000 d worth.

	PMT						Cryo						LAr		
Event type	^{232}Th	^{238}U$_{\text{low}}$	^{40}K	^{60}Co	^{238}U$_{\text{up}}$	^{235}U	^{232}Th	^{238}U$_{\text{low}}$	^{40}K	^{60}Co	^{238}U$_{\text{up}}$	^{235}U	^{39}Ar	^{85}Kr	Total
	Best fit rates														
1-sctr	0.0	0.0	0.0	0.0	0.0	0.0	0.0	0.0	0.0	0.0	0.0	0.0	0.0	0.0	0.0
>1-sctr	0.0	0.0	0.0	0.0	0.0	0.0	0.0	0.0	0.0	0.0	0.0	0.0	0.0	0.0	0.0
+Tef	1.6	1.1	0.1	0.0	0.0	0.0	0.2	0.1	0.0	0.0	0.0	0.0	0.0	0.0	3.1
+FS	0.1	0.0	0.0	0.0	0.0	0.0	0.0	0.0	0.0	0.0	0.0	0.0	0.0	0.0	0.1
+Tef+FS	0.0	0.0	0.0	0.0	0.0	0.0	0.0	0.0	0.0	0.0	0.0	0.0	0.0	0.0	0.0
	Passing veto prompt and 0.84 veto delayed acceptance														
1-sctr	0.0	0.0	0.0	0.0	0.0	0.0	0.0	0.0	0.0	0.0	0.0	0.0	0.0	0.0	0.0
>1-sctr	0.0	0.0	0.0	0.0	0.0	0.0	0.0	0.0	0.0	0.0	0.0	0.0	0.0	0.0	0.0
+Tef	0.6	0.7	0.0	0.0	0.0	0.0	0.1	0.1	0.0	0.0	0.0	0.0	0.0	0.0	1.5
+FS	0.0	0.0	0.0	0.0	0.0	0.0	0.0	0.0	0.0	0.0	0.0	0.0	0.0	0.0	0.1
+Tef+FS	0.0	0.0	0.0	0.0	0.0	0.0	0.0	0.0	0.0	0.0	0.0	0.0	0.0	0.0	0.0

Chapter 4

Cut summary

Cuts were implemented on the data to reduce the neutron, surface, and electron recoil backgrounds while preserving acceptance for WIMP events. The 530d UAr analysis benefited from already having a suite of cuts in place for the AAr and 70d UAr analyses; however, because of the increased exposure, further cut development was necessary. We note that cut development was an iterative process: certain cuts were necessary to obtain sensible event data for the development of background models, which were in turn required to motivate additional cuts to obtain the desired level of background. In this chapter we introduce the cuts used for the 530d UAr WIMP search analysis, and estimate the background rejection they provide.

4.1 Event quality cuts

The following cuts were implemented to ensure properly reconstructed event variables.

4.1.1 Number of channels

Purpose: Without information from all PMT channels, reconstructed parameters were not reliable.

Cut definition: Selected events with

```
nchannel == 38
```

which meant that all 38 PMT channels in the front-end boards of the data acquisition hardware were recorded.

Discussion: This cut was present in all previous DS-50 analyses.

4.1.2 Baseline

Purpose: Without a found baseline, analysis variables such as pulse integrals could not be reconstructed.

Cut definition: Selected events with

```
SumChannelHasNoBaseline == false
```

which meant that a baseline was found in the pre-trigger region of each channel waveform (see Sec. 2.2.2 for a description of the baseline-finding algorithm).

Discussion: This cut was present in all previous DS-50 analyses.

4.1.3 S1 saturation

Purpose: If there was ADC (analog-to-digital converter) saturation in any PMT channel for the S1 pulse, reconstructed parameters may not have been reliable. Such saturation was not expected to occur for S1's within the WIMP search region ($<$500 PE).

Cut definition: Selected events with

```
is_saturated_pulse0 == false
```

Discussion: This cut was present in all previous DS-50 analyses.

4.1.4 Veto present

Purpose: If veto information was not available for a particular event, we ran the risk of accepting a neutron event.

Cut definition: Selected events with

```
veto_present == true
```

meaning there was a veto event whose clock information matched that of the TPC event under consideration.

Discussion: This cut was present in the 70d UAr analysis. We note that problems with OD data processing (in which some OD runs could not be fully processed) resulted in slightly more events failing this cut in the original 70d UAr analysis; this issue was resolved when the 70d UAr data was reprocessed.

4.1.5 Trigger type

Purpose: Pulser triggers were mixed in with regular TPC triggers in the 530d UAr data. The pulser strobed at a rate of 0.05 Hz (0.01 Hz before Run 16708)[1]; however, it only opened an acquisition window if one was not already open (which in regular UAr running would have been caused by a TPC trigger). The analysis was not set up to look for WIMP events occuring in pulser-triggered acquisition windows.

Cut definition: Selected events with

```
trigger_type == 6 || trigger_type == 1
```

which refer to the TPC triggers[2]; pulser triggers had `trigger_type == 4`.

Discussion: This cut was new.

[1] DS-50 elog 5253.

[2] These were known as the low and high triggers respectively, and were a feature of the data acquisition allowing discrimination between small and large trigger signals upon acquisition. This was used to "prescale" high energy events during the AAr campaign, wherein only a set fraction of high energy events were recorded to reduce disk usage.

4.2 Basic event topology cuts

WIMP events were expected to be single-scatters in the active argon, *i.e.*, with one S1 pulse followed by one S2 pulse. The following cuts were implemented to select for such events.

4.2.1 Livetime

Purpose: A scatter in the LAr could occur during the inhibit window following a prior trigger. In such a scenario, the S1 signal would not trigger the detector, but the S2 signal might, if it arrived within the subsequent live window. A coincident pulse in the consequent acquisition window would then have been enough to create a spurious two-pulse event.

Cut definition: Selected events with

$$\texttt{livetime} > 400\,\mu\text{s}$$

Discussion: This was updated from the definition in previous analyses, which considered `(livetime + inhibittime)`. The new definition clearly accomplished its goal—if a LAr scatter occurred during the inhibit window, the latest an associated S2 could possibly arrive was one `tdrift_max` ($\sim$376 µs) from the end of the inhibit window/the start of the subsequent live window.

4.2.2 Number of pulses

Purpose: A WIMP event was expected to be a single-scatter in the LAr, consisting of one S1 and one S2 pulse. Occasionally, the intense illumination from S2 could induce the emission of electrons from the cathode window. These electrons would be drifted over the full vertical length of the TPC before their passage through the gas pocket resulted in a secondary ionization pulse, which we referred to as S3, or an

S2-echo. To account for this, the topology for single-scatters was expanded to also include events that had exactly three pulses, wherein the second and third pulses were separated by 372-400 µs.

Cut definition: Selected events with

```
n_phys_pulses == 2 || (n_phys_pulses == 3 && has_s3 == true)
```

Discussion: This cut was present in all previous DS-50 analyses.

4.2.3 Start time of S1

Purpose: This cut was used in previous analyses to remove events triggered by the long tail of an S2 pulse. In such a scenario, the pulse-finding algorithm—which looks for macroscopic photoelectron signals regardless of PMT multiplicity—would often reconstruct the start time of the first pulse to be distinct from the trigger time.

We note that cut 4.2.1 should have already addressed this issue—if an S2 pulse occurred near the end of the inhibit window, such that its tail (and not its leading edge) caused a trigger, the event livetime would be less than 400 µs, and the event would be removed; if the trigger occurred late enough to survive cut 4.2.1, the trigger signal would have been the leading edge of the S2 pulse instead of its tail, and the event would have survived this cut anyway. Nevertheless, this cut was retained as a safeguard against pathological events, as it had virtually no impact on WIMP acceptance.

Cut definition: The trigger time corresponded with $t = 0$, but the trigger signal timing was offset because of hardware delays (*e.g.*, from cabling). We selected events with

```
s1_start_time >= -6.1 µs && s1_start_time <= -6.0 µs
```

Discussion: This cut was present in all previous DS-50 analyses, but with different offsets for different run sets.

4.2.4 S2 F90

Purpose: The S2 risetime (pulse start time to pulse peak time) was on the order of 1 µs [50], which was much slower than that for S1. Thus, F90 for a true S2 signal was very small.

Cut definition: Selected events with

$$\texttt{total\_s2\_f90\_fixed} < 0.2$$

Discussion: This cut was present in the AAr and 70d UAr analyses.

Background rejection: Like WIMP events, the second pulse in all two-pulse background events (*i.e.*, passing cut 4.2.2) should be an S2. Thus, any background rejection from this cut should be from accidental acceptance loss.

4.2.5 Minimum corrected S2/S1

Purpose: S2 pulses were expected to be large—a single electron extracted at the (radial) center of the TPC corresponded with an S2 of ∼24 PE [40, Sec. 4.3.2]. This cut was implemented to help ensure that the second pulse in any potential WIMP event was indeed an ionization signal, even in the context of NRs (which were expected to have lower $^{\mathrm{S2}}/_{\mathrm{S1}}$ relative to ERs).

Cut definition: Selected events with

$$\texttt{total\_s2\_xycorr/total\_s1\_corr} > \texttt{f(total\_s1\_corr)}$$

where `f(total_s1_corr)` was a polynomial

$$f(x) = 21 - 0.14 \times x + 4.6 \times 10^{-4} \times x^2 - 7.4 \times 10^{-7} \times x^3 + 4.4 \times 10^{-10} \times x^4$$

set to have an acceptance of 0.99 on ^{241}AmBe NR events. $f(\mathrm{S1})$ evaluates to 14.1 at S1 = 60 PE, and to 1.61 at S1 = 460 PE (Fig. 4.1).

Discussion: This cut was new.

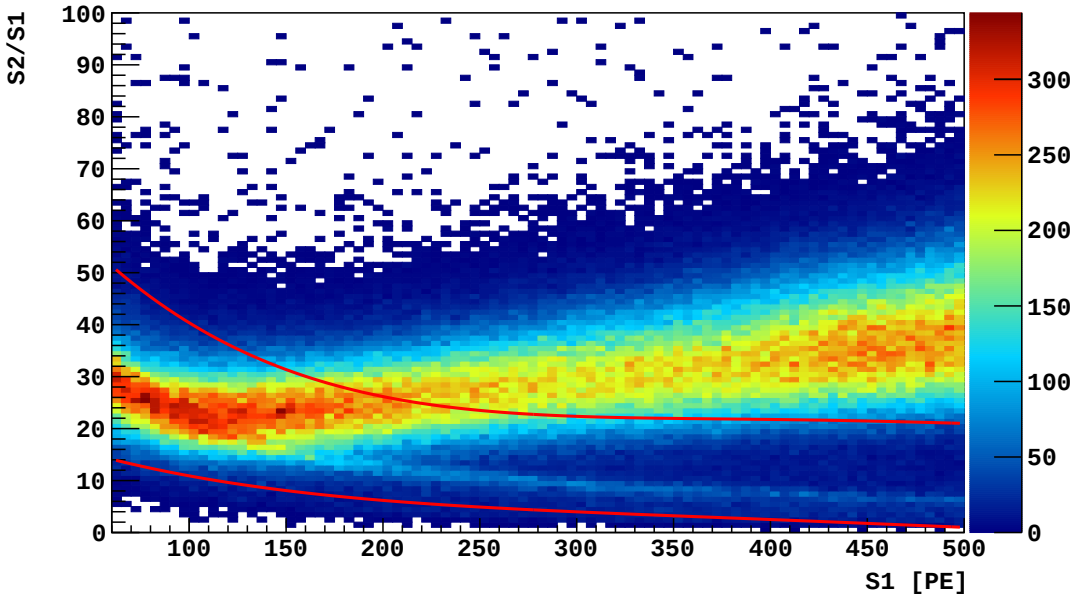

Figure 4.1: S2/S1 *vs.* S1 of ^{241}Am^{13}C neutron source calibration events, with the minimum and maximum S2/S1 cuts overlaid in red. The cuts select for NRs, which have lower S2/S1 relative to ERs (the bright band of events).

4.3 Neutron background cuts

The outer detector (LSV and WCV) cuts were designed to tag and veto cosmogenic and radiogenic neutron events. The development of these cuts is reviewed in detail in [25].

The acquisition window for the OD spanned $t \in [-10.5, 190]$ µs, where $t = 0$ was when the OD received the TPC trigger signal. Calibration with a source of coincident γ-rays (*e.g.*, ^{60}Co) indicated that the signal responsible for the TPC trigger corresponded with $t \approx -6.5$ µs in the LSV, which is referred to as the prompt time.

4.3.1 Prompt LSV signal

Purpose: The prompt LSV window was defined to be $t \in [-50, 250]$ ns about the prompt time. An LSV signal in this window could come from several processes:

1. Thermalization of a neutron in the LSV.

2. Scattering of a γ-ray in the LSV. Such γ-rays could come from radioactive decay or inelastic neutron scattering.

Cut definition: Selected events with

`veto_roi_lsv_charge_vec[0] < 1 PE`

Discussion: This cut was present in the 70d UAr analysis (veto Phase II).

4.3.2 Delayed LSV signal

Purpose: The LSV scintillator cocktail was loaded with ^{10}B (in the form of trimethyl borate, TMB) as a target for neutron capture. In particular, this neutron capture process produced α-particles that had a short range in the LSV, thus ensuring a corresponding veto signal was seen. Neutron capture, dominated by capture on ^{10}B in the LSV, occurred with a time constant of 22 µs (given the pseudocumene, PC, to TMB mixture in the scintillator cocktail). We looked for this signal in a 500 ns-wide sliding window scanning over the LSV acquisition window, starting from the prompt time (*i.e.*, $t \in [0, 190]$ µs).

Neutron capture could also occur with other elements present in the LSV, *e.g.*, H, C, and O; however, such captures produced high energy γ-rays that could escape without scattering in the LSV.

Cut definition: Selected events with

`veto_slider_lsv_charge_vec[0] < 6 PE`

Discussion: This cut was present in the 70d UAr analysis (veto Phase II).

4.3.3 Pre-prompt LSV signal

Purpose: External neutrons could scatter in the LSV before entering the TPC. We looked for such signals in a 500 ns-wide sliding window scanning over the LSV acquisition window, up to the prompt time (*i.e.*, $t \in [-10.5, 0]$ µs).

Cut definition: Select events with

$$\texttt{veto\_slider\_lsv\_charge\_vec[1]} < 3\ \texttt{PE}$$

Discussion: This cut was present in the 70d UAr analysis (veto Phase II).

Rejection:

4.3.4 Muon signal

Purpose: Passing muons could result in neutron production via spallation. We tagged muons, and any energetic charged particles from the accompanying showers passing through the OD using their large Cherenkov signal in either the LSV or the WCV.

Cut definition: Selected events with

$$\texttt{veto\_lsv\_total\_charge} < 2000\ \texttt{PE}\ \texttt{\&\&}\ \texttt{veto\_wt\_total\_charge} < 400\ \texttt{PE}$$

Discussion: This cut was present in the 70d UAr analysis (veto Phase II).

4.3.5 Delayed neutrons from cosmogenic activation

Purpose: Muon interactions could activate nuclei that then decayed via neutron emission. The main culprit was ^{9}Li, which decays with a lifetime of 0.18 s [51].

Cut definition: Selected events with

$$\texttt{muon\_dt} > 0.6\ \texttt{s}$$

where `muon_dt` was the accumulated `(livetime + inhibittime)` of events since the last event failing cut 4.3.4 (*i.e.*, `muon_dt` was reset to 0 whenever an event failed cut 4.3.4). An event's `livetime` was added to `muon_dt` before this cut was checked, and its `inhibittime` was added after.

We note that this scheme did not tag all passing muons, only those with a TPC coincidence that triggered the data acquisition.

Discussion: The width of the time window (*i.e.*, threshold for `muon_dt`) was decreased from the 2 s duration used in the 70d UAr analysis to reduce acceptance loss.

4.4 Fiducialization

Fiducial cuts were implemented to remove scatters close to the inner surfaces of the detector (anode/cathode windows and Teflon TPC wall). This mitigated the surface and ER backgrounds (the latter since instigating γ-rays originated from outside the active volume).

4.4.1 Drift time

Purpose: Some fiducialization was necessary along the vertical axis to deal with γ-induced background from the PMTs, as well as surface background from the anode/cathode windows. We preserved the drift time fiducialization from the AAr and 70d UAr analyses.

Cut definition: Selected events with

$$40 < \texttt{tdrift} < 334.6 \text{ µs}$$

which corresponded to $\sim$4 mm from the grid and the cathode window.

Discussion: This cut was present in the AAr and 70d UAr analyses.

4.4.2 Uncorrected S2

Purpose: Successful xy-reconstruction was required for the implementation of radial fiducialization; however, the xy-reconstruction algorithm [32] did not work on

events with small uncorrected S2 signals, assigning such events an (x, y) position of $(-19, -19)$ cm. We introduced a cut on uncorrected S2 to make this behavior of the xy-reconstruction more explicit.

Cut definition: Selected events with

$$\texttt{total\_s2} > 200 \text{ PE}$$

where the 200 PE threshold was approximately where the xy-algorithm had a 50% efficiency at reconstructing events.

Discussion: This was an updated version of a cut on minimum S2; in the 70d UAr analysis the cut was defined to select events with `total_s2_xycorr > 100`.

4.4.3 Radius

Purpose: A drift time dependent radial fiducialization was implemented to reject background events with reconstructed xy positions near the TPC wall (Fig. 4.2). The radial cut was designed using Monte Carlo simulations of the ER background to remove 50% of simulated events with a Teflon Cherenkov component in each bin of drift time (by Zhu). Because of difficulties in accounting for the resolution of the xy reconstruction algorithm in our simulations, the radial cut's background rejection measured using the 530d UAr data was used for making background predictions (Sec. 6.2.3). The cut's effect on events in the fully open 530d UAr data, passing cuts 4.1.1 through 4.2.3 and 4.4.1 through 4.4.2, with $60 < \text{S1} < 460$ PE, and in the original blinding box (Fig. 6.1), is shown in Fig. 4.2.

Cut definition: Selected events with

$$\texttt{r} < \texttt{r\_thres(tdrift)}$$

Discussion: This cut was new.

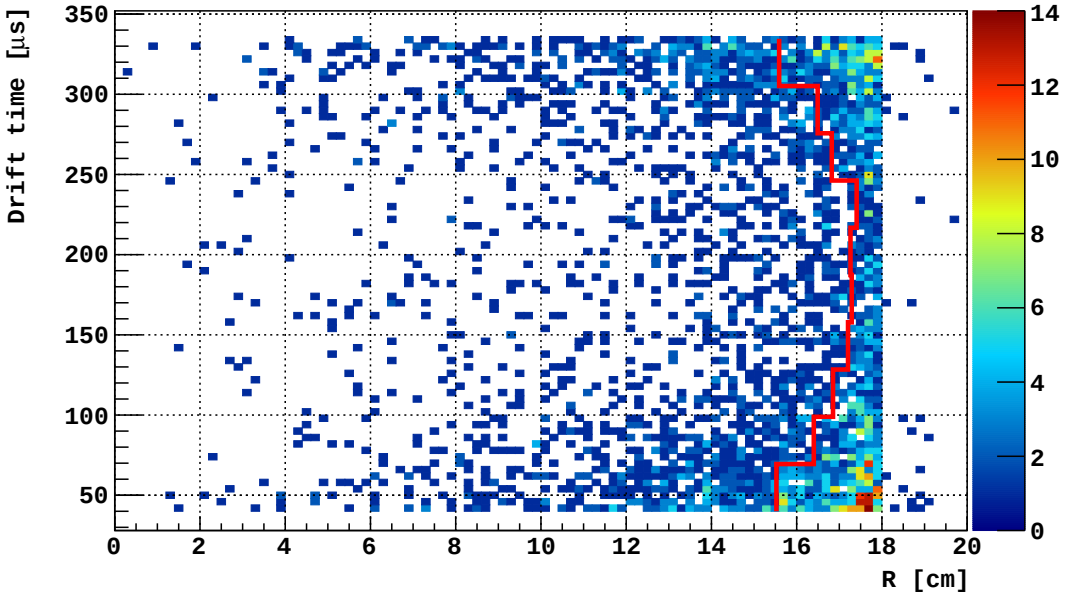

Figure 4.2: The drift time dependent radial cut.

4.5 Surface background cuts

The following cuts were designed to remove the two classes of surface background discussed in Sec. 3.1.2.

4.5.1 Long S1 tail

Purpose: The scintillation response of LAr and TPB induced by α-particles was studied in a separate experiment (RaDOSE), which involved a detector set-up with α-emitters (in the form of a ^{210}Po needle, or deposited radon daughters) in front of a TPB-coated surface, in both vacuum and LAr. In particular, the passage of α-particles through TPB was found to induce long-lived scintillation in the TPB, which provided a way to tag the problematic α-decay topologies described in Sec. 3.1.2. [42] should be consulted for more detail.

Cut definition: Selected events with

```
iTail < iTail_thres(99th percentile)
```

where

$$\texttt{iTail = e.total\_s1\_long\_us\_integrals[0] - e.total\_s1\_long\_us\_integrals[64]}$$

was the integral (in [PE]) spanning from 10 µs after the start of the S1 pulse to the start of the S2 pulse, and `iTail_thres` (which was set using observations from RaDOSE) depended on `total_s1` and `tdrift`.

Discussion: This cut was new.

4.5.2 S1 top bottom asymmetry

Purpose: This cut was implemented to help ensure that the event had correlated S1 and S2 pulses, instead of being a spurious S1-only + stray S2 event (Sec. 3.1.2). This was done by checking that the vertical position as indicated by the S1 pulse's top bottom asymmetry (TBA) was consistent with the event's drift time. [52] should be consulted for more detail.

Cut definition: Selected events with

$$\texttt{TBA}_{\texttt{tdrift}} - 3\sigma_{\texttt{TBA}} < \texttt{TBA}_{\texttt{obs}} < \texttt{TBA}_{\texttt{tdrift}} + 3\sigma_{\texttt{TBA}}$$

where $\texttt{TBA}_{\texttt{obs}}$ was the observed TBA of the S1 pulse, $\texttt{TBA}_{\texttt{tdrift}}$ was the mean TBA (as a function of drift time), obtained from a fit on AAr data:

$$\texttt{TBA}_{\texttt{tdrift}} = 0.0453611 - 6.36123\text{E-}4 \times \texttt{tdrift} - 8.66415\text{E-}7 \times \texttt{tdrift}^2$$

and $\sigma_{\texttt{TBA}}$ was the RMS of $(\text{TBA} - \text{TBA}_{\text{mean}})$ (as a function of S1), also obtained from a fit on AAr data. $\sigma_{\texttt{TBA}}$ was a 9th degree polynomial with coefficients shown in Tab. 4.1:

$$\sigma_{\texttt{TBA}} = \sum_{i=0}^{9} p_i \times \texttt{total\_s1}^i$$

Discussion: This cut was new.

Table 4.1: Coefficients for a 9th degree polynomial fit of σ_{TBA} *vs.* S1.

p_0	p_1	p_2	p_3	p_4
0.332	−0.00744	1.21E−4	−1.25E−6	8.31E−9
p_5	p_6	p_7	p_8	p_9
−3.59E−11	1.00E−13	−1.75E−16	1.72E−19	7.31E−23

4.5.3 Early S2 pulse shape

Purpose: This cut was applied to help ensure that the second pulse in an event was an S2 signal, instead of an unresolved S1-S2 pileup signal (*i.e.*, a short drift time event that looks like a single S2 pulse). This was done by inspecting the early pulse shape of the second pulse to see if it was consistent with an S2 (*i.e.*, slow). [52] should be consulted for more detail.

Cut definition: Selected events with

$$\texttt{I1} < 4 \;\texttt{||}\; (4 < \texttt{I1} < 500 \;\texttt{\&\&}\; \frac{\texttt{I90}}{\texttt{I1}} < e^{-\frac{\texttt{I1-2.5}}{4}} + 0.1e^{-\frac{\texttt{I1-2.5}}{400}} + 0.2e^{-\frac{\texttt{I1-2.5}}{60}})$$

where `I90` was the integral of the candidate S2 pulse over the first 90 ns, and `I1` was its integral over the first 1 µs:

$$\texttt{I90} = \texttt{total\_s2} \times \texttt{total\_s2\_f90\_fixed}$$

$$\texttt{I1} = \texttt{pulse\_info\_us\_integrals[7]}$$

Discussion: This cut was new.

4.6 Electron recoil background cuts

The development of an F90 model for ER background will be discussed in detail in Ch. 5. The subsequent development of the WIMP search region (a cut in F90 *vs.* S1 phase-space), which was one of the main cuts against ER background, will be discussed in Ch. 7.

4.6.1 Maximum corrected S2/S1

Purpose: $^{S2}/_{S1}$ for NRs was expected to be lower than that for ERs. Unlike cut 4.2.5, this cut strongly discriminated between NRs and ERs for S1>200 PE. We note that since S2 light was not propagated in our final ER background simulations, this cut's rejection on ER events was not accounted for in the ER background prediction. This conservative approach was feasible because the designed WIMP acceptance of the cut was very high, and rejection of the problematic ER background (ER events with a Cherenkov component) was modest.

Cut definition: Selected events with

$$\texttt{total\_s2\_xycorr/total\_s1\_corr} < \texttt{f(stotal\_s1\_corr)}$$

where `f(total_s1_corr)` was a polynomial

$$f(x) = 76 - 0.51 \times x + 1.8 \times 10^{-3} \times x^2 - 2.8 \times 10^{-6} \times x^3 + 1.6 \times 10^{-9} \times x^4$$

set to have an acceptance of 0.99 on ^{241}AmBe NR events. f(S1) evaluates to 51.3 at S1 = 60 PE, and to 21.4 at S1 = 460 PE (Fig. 4.1).

Discussion: This cut was new.

4.6.2 S1 prompt maximum fraction

Purpose: Compton scattering of γ-rays in the fused silica windows (the individual PMT windows, and the anode/cathode windows) could produce recoil electrons energetic enough to generate Cherenkov radiation. If accompanied by a Compton scatter in the LAr, the resulting event could look like a NR for two reasons: 1) Since the Cherenkov signal is entirely prompt, its pileup with the LAr scintillation increases event F90; and 2) Since the Cherenkov signal increases the event's S1, but is not accompanied by an S2, there is an overall decrease in event $^{S2}/_{S1}$.

The proximity of the fused silica windows to the TPC PMTs meant that Cherenkov radiation in these volumes had a high probability of being concentrated in a single PMT. Thus, we removed events with high concentrations of prompt S1 (*i.e.*, S1 in the first 90 ns of the pulse) in a single PMT—in particular, the cut threshold was set to remove the 5% of AAr events with the highest S1 prompt maximum fraction, per (S1 prompt, Drift time) bin.

We note that Cherenkov radiation in the Teflon TPC wall presented the same problem when accompanying a Compton scatter in LAr; however, because of the distance from the PMTs, and the diffuse reflectance of the Teflon, this cut was not particularly effective on such events.

Cut definition: Selected events with

$$\texttt{s1\_prompt\_max\_frac} < \texttt{s1\_prompt\_max\_frac\_thres(AAr 95th percentile)}$$

Discussion: Some version of this cut was present in all previous DS-50 analyses; here, however, the cut was updated to consider the light distribution of prompt S1, rather than that of total S1. The S1 prompt maximum fraction is also referred to as "S1pmf".

4.6.3 Negative log-likelihood of S1 light distribution

Purpose: This was an intricate cut designed to remove events whose S1 light distributions were inconsistent with their reconstructed xy positions (which was derived from the events' S2 information) and drift time; [53] should be consulted for more detail. In brief, events were first binned into voxels based on their drift time and reconstructed xy position, and then had their S1 light distributions compared against voxel-dependent templates made from AAr data.

We note that since S2 light was not propagated in our final ER background simulations, this cut's rejection on ER events was not accounted for in the ER background

prediction. This conservative approach was feasible because the designed WIMP acceptance of the cut was very high, and background rejection after application of the S1 prompt maximum fraction cut (cut 4.6.2) was low.

Cut definition: Selected events whose S1 light distributions had a low negative log-likelihood given their reconstructed xy positions (*i.e.*, `!nll_hi`).

Discussion: This cut was new.

4.6.4 WIMP search region

Purpose: The WIMP search region, or WIMP box, was the cut in F90 *vs.* S1 phase-space, designed to discriminate between ERs and NRs.

Cut definition: The development of this cut will be discussed in Ch. 7.

4.7 Background rejection

Table 4.2 summarizes the responses of various sets of events to the cuts described above, applied in the sequence shown on the table. It provides an indication of the background rejection coming from the various cuts. In all cases, we began with a set of "basic" cuts that are not based on the events' physics, and hence do not discriminate between WIMP and background events—the event quality cuts (Sec. 4.1), the livetime cut (cut 4.2.1), and the inhibit window guarding against delayed neutrons from cosmogenic activation (cut 4.3.5).

4.7.1 Neutron background

The cuts' effects on neutron background were studied by counting events from $^{241}\mathrm{Am}^{13}\mathrm{C}$ source calibration data with $60 < \mathrm{S1} < 460\,\mathrm{PE}$ and $0.6 < \mathrm{F90} < 0.85$ (Fig. 4.3). We see from Tab. 4.2 that together, the LSV prompt and delayed cuts

Table 4.2: Responses of various event sets to analysis cuts, applied in the sequence shown. $^{241}Am^{13}C$ data were a source of neutron events, and 70d UAr data were a source of ER background. The modeled ER background with either a Teflon (Tef) or fused silica (FS) Cherenkov component (described in Ch. 5) were normalized to 530 d of UAr running.

Cuts applied	$^{241}Am^{13}C$ data	70d UAr data	Model ER w/Tef Cherenkov	Model ER w/FS Cherenkov
Basic	56809	13607	-	-
Single-scatter	22732	10909	3749	2557
Drift time	17553	4410	2385	2296
S1 start time	17552	4405	-	-
S2 F90	17535	4281	-	-
Min. uncorr. S2	17432	4076	-	-
Min. S2/S1	17165	3988	-	-
S1pmf	16246	3238	2096	428
LSV prompt	120	2259	1070	227
LSV delayed	60	1862	-	-
LSV preprompt	60	1855	-	-
Muon	60	1854	-	-
Radius	50	1333	-	-
S1 tail	50	1330	-	-
S1 TBA	50	1326	-	-
S2 shape	50	1326	-	-
Max. S2/S1	49	1243	-	-
NLL	47	1226	-	-
WIMP box	20	0	0.194	0.000

(cuts 4.3.1 and 4.3.2) rejected neutron events by a factor of >200. The most effective TPC cut against neutron background was the single-scatter cut (cut 4.2.2).

4.7.2 Electron recoil background

The cuts' effects on ER background were studied by counting events from the 70d UAr data with $60 < \text{S1} < 460$ PE and $0.4 < \text{F90} < 0.85$ (Fig. 4.3), where the F90 selection was implemented to isolate ER events that were particularly problematic (*i.e.*, ER events with a Cherenkov component). To remove single-pulse surface background events in the data (Sec. 3.1.2), the basic cuts were extended to also remove events with $\leq$1 pulse. From Tab. 4.2, we see that PSD, implemented via the WIMP box

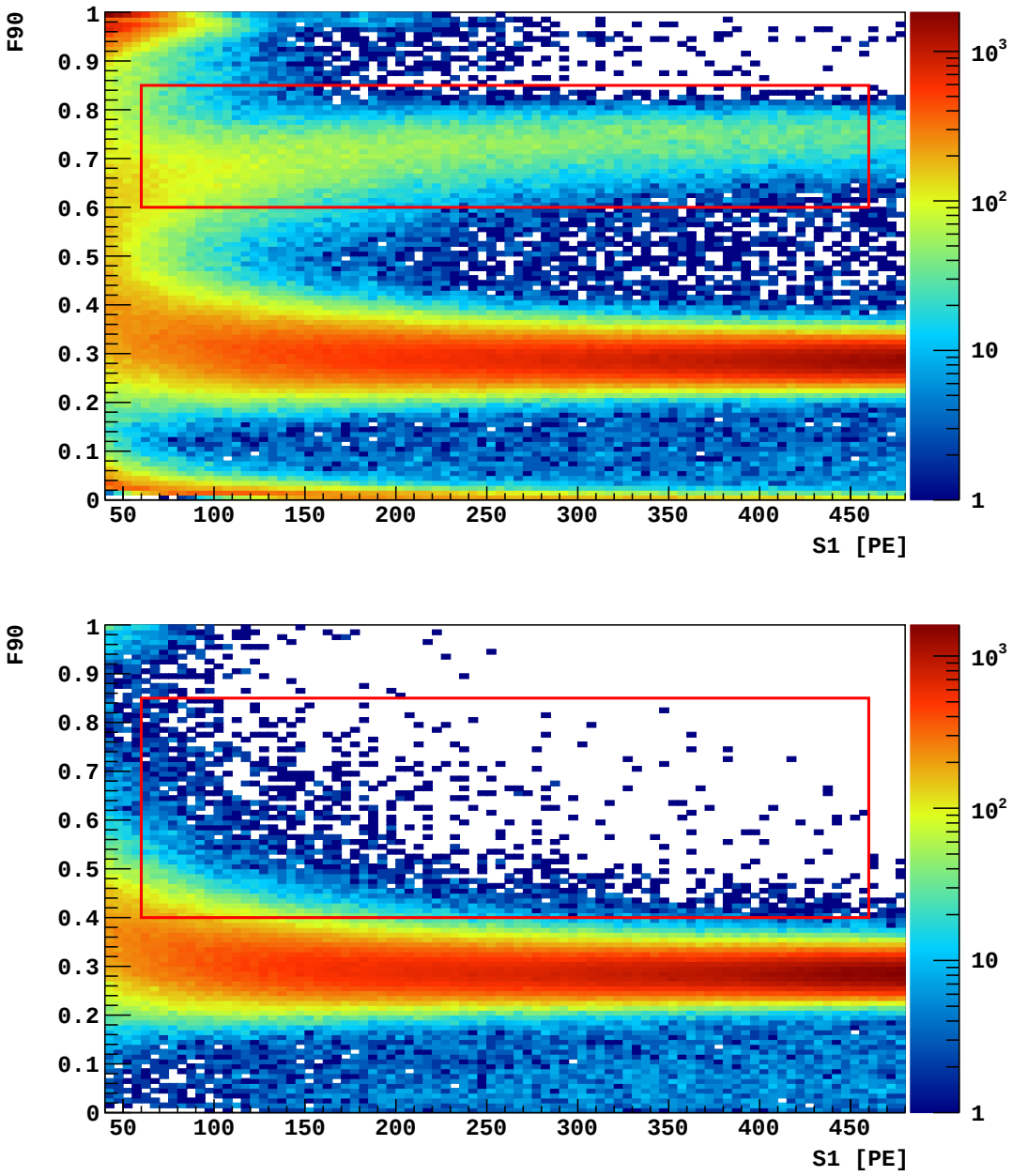

Figure 4.3: **Top:** ^{241}Am^{13}C neutron source calibration events passing basic cuts (see text for details). **Bottom:** 70d UAr events passing basic cuts, and with >1 pulses. Events in the red boxes were counted to estimate the rejection power of the analysis cuts.

(cut 4.6.4), was the most effective cut against ER background. Drift time fiducialization was also quite effective against ER events, which is unsurprising given many of these events were caused by Compton scattering of γ-rays from radioactive decay in the PMTs.

As a supplement, we also present in Tab. 4.2 the various cuts' effects on modeled ER events with Teflon or fused silica Cherenkov components (see Ch. 5 for a description of the model). We note that only a few of the cuts could be applied on the modeled events because details such as S2 and random coincidences were not modeled. However, we still see from Tab. 4.2 that the S1pmf cut (cut 4.6.2) was most effective at rejecting ER events with a fused silica Cherenkov component. Since the S1pmf cut was an existing cut from the 70d UAr analysis, this indicated from the outset of the 530d UAr analysis that ERs with a Teflon Cherenkov component would require extra attention.

4.7.3 Surface background

A similar treatment for surface background was not feasible as there was no good way to isolate surface background events in DS-50 data without using the cuts meant to reject them.[3] Thus, we direct readers to [42, Sec. 8.8] and [52] for detailed estimates of the rejection provided by the surface background cuts (Sec. 4.5).

[3] We note that surface events can be isolated at high S1 (Sec. 3.1.2); however these all fail the saturation cut (cut 4.1.3).

Chapter 5

Modeling electron recoil F90

Pulse shape discrimination via F90 is a powerful discriminator between electron and nuclear recoils in liquid argon. In particular, the WIMP search regions in both the AAr and 70d UAr analyses were shaped to reduce the ER background—which was the dominant background in both analyses—to acceptable levels. Since the 530d UAr analysis was to have greater exposure, and was to be a blind analysis (*i.e.*, analyzers would not have access to data with high F90; see Ch. 6 for details), modeling the F90 of electron recoils was important both for cut design (in the form of the WIMP box) and for background prediction.

Among its generation of liquid argon dark matter search experiments, DS-50 is unique for its use of depleted argon. The primary goal for this is the reduction of ER background from ^{39}Ar β-decay. Since a significant amount of data was taken with AAr in DS-50 prior to UAr running, the possibility of modeling ER F90 using a high-statistics empirical data set instead of an analytic model presented itself. In this chapter we describe the development of such a data-driven model for the F90 of single-scatter ERs.

5.1 Method overview

Presented here is an overview of the steps followed in constructing S1 and F90 for simulated background events (shown schematically in Fig. 5.1). Details pertaining to each step will be provided in subsequent sections.

1. Start with background events from our Monte Carlo simulations.

2. Cluster the simulated deposits to obtain individual scatters for each event. Each event now has an associated number of clusters/scatters, each of which has an associated energy, E_{clus}. (Henceforth, "cluster" and "scatter" may be used interchangeably.) As a guide, we note that the S1 range of interest was expected to be between 60 PE and 460 PE, or approximately between 8 keV and 63 keV in terms of electron recoil energy.

3. Implement a multiple-S2 resolution cut, to mimic the effect of pulse-finding. Also construct the number of pulses, and drift time, associated with this event.

4. For each cluster, calculate the amount of energy that manifests as a scintillation signal, E_{scin}. The rest of the energy either goes into the ionization signal (S2), or is lost as heat.

5. Scale E_{scin} by a light yield to obtain a true scintillation signal S1.

6. Smear $\mathrm{S1}_{\mathrm{true}}$ to simulate resolution effects in the detector. The smeared quantity $\mathrm{S1}_{\mathrm{smeared}}$ is analogous to S1 actually observed in the detector.

7. Using $\mathrm{S1}_{\mathrm{smeared}}$, look up a corresponding F90 from the F90 *vs.* S1 distribution of AAr data (used as a probability density function).

8. By keeping track of each cluster's contribution to the prompt signal (*i.e.*, that in the first 90 ns), construct the overall S1 and F90 of the event. Any Cherenkov

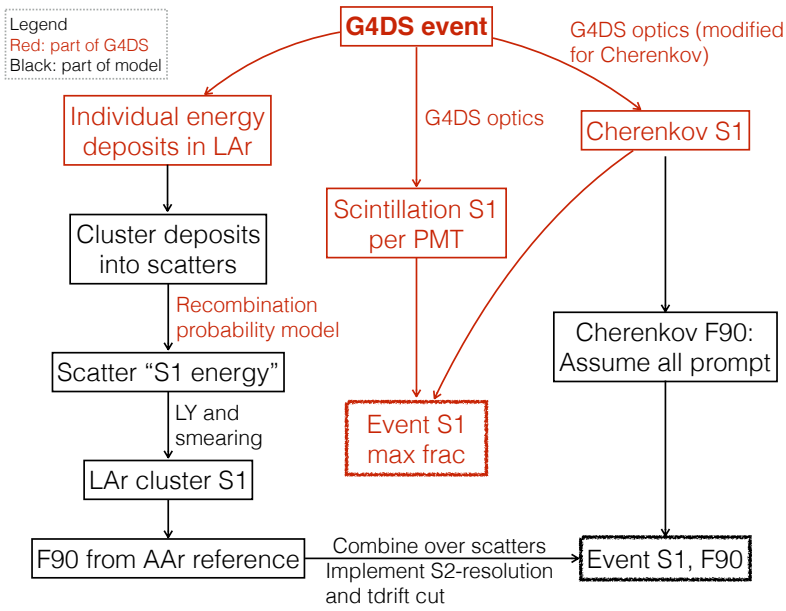

Figure 5.1: Flowchart depicting the broad steps of the empirical F90 model. Steps for combining Cherenkov output from the simulation with the model's S1 and F90 output are also shown. "G4DS" is the collaboration's Geant4-based Monte Carlo simulation [54].

signal generated in the simulation is also added to the event at this stage, assuming Cherenkov signals are entirely prompt.

5.2 Simulated events

Monte Carlo simulations of the backgrounds described in Ch. 3 are used. In particular, the collaboration's Geant4-based Monte Carlo simulation, known as "G4DS" [54], is used; in addition to DS-50 detector geometries and materials, this framework includes a model for DS-50 detector optics.

The simulated events provide information about γ and β interactions in the various detector volumes/materials (including the LSV), and also track the production of Cherenkov radiation in the Teflon and fused silica volumes in the TPC.

We note that two variants of the Monte Carlo were actually run. In one version scintillation photons for LAr interactions were always generated and tracked, as long as the interactions fell below some energy threshold (<110 keV); ∼500 d worth of simulated UAr events were generated with this version. In the other version, scintillation photons for LAr interactions were only generated and tracked if the event also produced a Cherenkov signal; this pared-down version was necessary to reduce the computational requirements (both in terms of time and storage) for running the simulations. ∼30000 d worth of simulated UAr events were generated with this second version of the Monte Carlo; this was the primary simulated event set used for the WIMP-search analysis presented in this work.

5.3 Clustering simulated event deposits

There is generally no one-to-one correspondence between the number of energy deposits in the simulation output, and the number of physical scatters in an event. A simple Monte Carlo simulation of a 10 keV photon started in the active argon volume was run to illustrate this. The following information was extracted from the simulation:

- **The track of the seeded photon.** Since only one photon was started at a time, it was always tagged with *Parent track ID* = 0 and *Track ID* = 1 in the simulation. These uniquely identify the *primary track*.

- **Vertices off the primary track.** In the simulation, there is one such vertex for each instance in which a secondary track branches off of the primary track.[1] Each vertex had a *Creator process ID* that described the nature of the interaction that generated it—*e.g.*, photoelectric effect or Compton scatter.[2]

[1] If the secondary track is below some energy threshold, the simulation skips tracking, and proceeds to generating deposits instead; in such cases there is still an associated vertex.

[2] Only looking at deposit information is not viable, as deposits off secondary tracks do not provide information about the interaction that produced the secondary track.

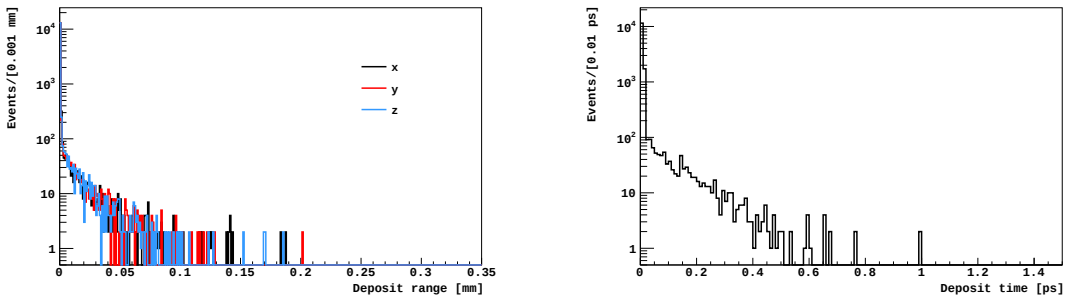

Figure 5.2: (Left) Positions, and (Right) times of simulated deposits, relative to an arbitrarily picked reference deposit for each simulated event; each simulated event was a 10 keV photon started in the bulk of the liquid argon volume.

- **Deposit information.** This was to be compared against the vertices' physics information.

5000 such events were simulated. Of these, all had a photoelectric vertex, while only 5 events also had a Compton scatter vertex. This indicated that the vast majority events were single-sited, with only a few double-scatters. In contrast, the number of deposits per event ranged from 1 to 10. Thus, there was a need for clustering deposits to attain the expected physical result. Figure 5.2 shows the positions and times of the deposits for each simulated event, relative to an arbitrarily picked reference deposit.

5.3.1 Development and implementation

Figure 5.2 suggests that the clustering range should be something on the order of 0.001 ns and $r = \sqrt{3 \times (0.2\,\text{mm})^2} = 0.35\,\text{mm}$. The final threshold was set by studying the model's response to changes in the clustering range. In particular, two parameters were examined: the number of clusters, and the energy per cluster, in an event.

Figure 5.3 shows the number of clusters in simulated $^{60}\text{Co}_{\text{cryo}}$ events (events induced by γ-rays from ^{60}Co decay in the cryostat components) with <200 keV total cluster energy, corresponding to various clustering ranges. We see that a clustering range of 0.01 cm resulted in more two-cluster than single-cluster events, which was

not the case with longer clustering ranges. The cluster multiplicity per event was roughly stable for clustering thresholds $\geq$0.03 cm.

Figure 5.3 shows $^{60}\mathrm{Co}_{\mathrm{cryo}}$ E_{clus} spectra corresponding to different clustering ranges. We note that a clustering range of 0.01 cm resulted in several spikes in the spectrum at low E_{clus} that were ameliorated, but still present, with a threshold of 0.02 cm. These spikes were absent with the higher clustering thresholds. These low energy spikes were not expected since ^{60}Co decay does not produce x-rays with such intensities. Inspection of the simulation's output revealed that clusters contributing to one of these spikes overwhelmingly had $E_{\mathrm{clus}} = 3.1775999$ keV exactly, and were present only in events that had more than one cluster (given the clustering range). This indicated that a clustering range of $\leq$0.02 cm resulted in scatters being incorrectly broken up, and hence were too short. Such spikes were also present in the E_{clus} spectra of the other γ-ray backgrounds when clustering ranges $\leq$0.02 cm were used.

Finally, we noted that the E_{clus} spectra with clustering ranges of 0.03 cm and 0.04 cm were different. To choose between the two, we studied the simulated E_{clus} spectrum from ^{39}Ar. For our energy range of interest ($\sim$8-63 keV), LAr has a stopping power of $\sim$18-4 MeVcm^2/g for electrons [55]. Given the density of LAr (1.4 g/cm^3), this meant that decay-β's in our energy range of interest have a range of $<$0.01 cm, and hence should consist of single-cluster events only. To establish what the ^{39}Ar spectrum ought to look like, an extremely loose displacement and timing threshold of (0.2 cm, 10 ns) was first used to guarantee all such events ended up as single-clusters (Fig. 5.4). In particular, the emergence of features in the (0.03 cm, 10 ns) spectrum suggested the 0.03 cm clustering range was too tight, whereas (0.04 cm,0.01 ns) produced the desired spectrum. Thus, the clustering threshold was set at (0.04 cm, 0.01 ns), where the 0.01 ns threshold was chosen to be generous, since this threshold had typically been set at 1 ns in previous analyses.

The clustering algorithm constructed the position of a cluster as an average of its component deposits' positions, weighted by their respective deposit energies; the time of the cluster was arbitrarily set as that of one of its component deposits because the 0.01 ns clustering threshold was small to begin with.

Systematics with tighter and looser clustering conditions will be studied in Sec. 5.11.

5.4 Implementing a multiple-S2 resolution, and reproducing analogues of data variables

Selection criteria were first implemented to only consider deposits in the TPC/active Ar. In G4DS output parameters, a deposit is in the active argon volume if:

$$\texttt{dep\_mat == 8} \tag{5.1}$$

$$\sqrt{\texttt{dep\_x}^2 + \texttt{dep\_y}^2} \texttt{ < 17.77 cm} \tag{5.2}$$

$$\texttt{-21.439 < dep\_z < 14.31 cm} \tag{5.3}$$

where `dep_mat` is a material identifier, and `dep_x`, `dep_y` and `dep_z` denote the deposit's coordinates.

To construct the number of pulses (`npulses`) and drift time (`tdrift`), the simulated events were then processed as follows:

- **Accounting for multiple-S2 resolution.** In actual data processing, the pulse-finding algorithm tags events containing multiple S2's with some efficiency. The development of an analogue on the simulated events will be discussed in Sec. 5.4.1.

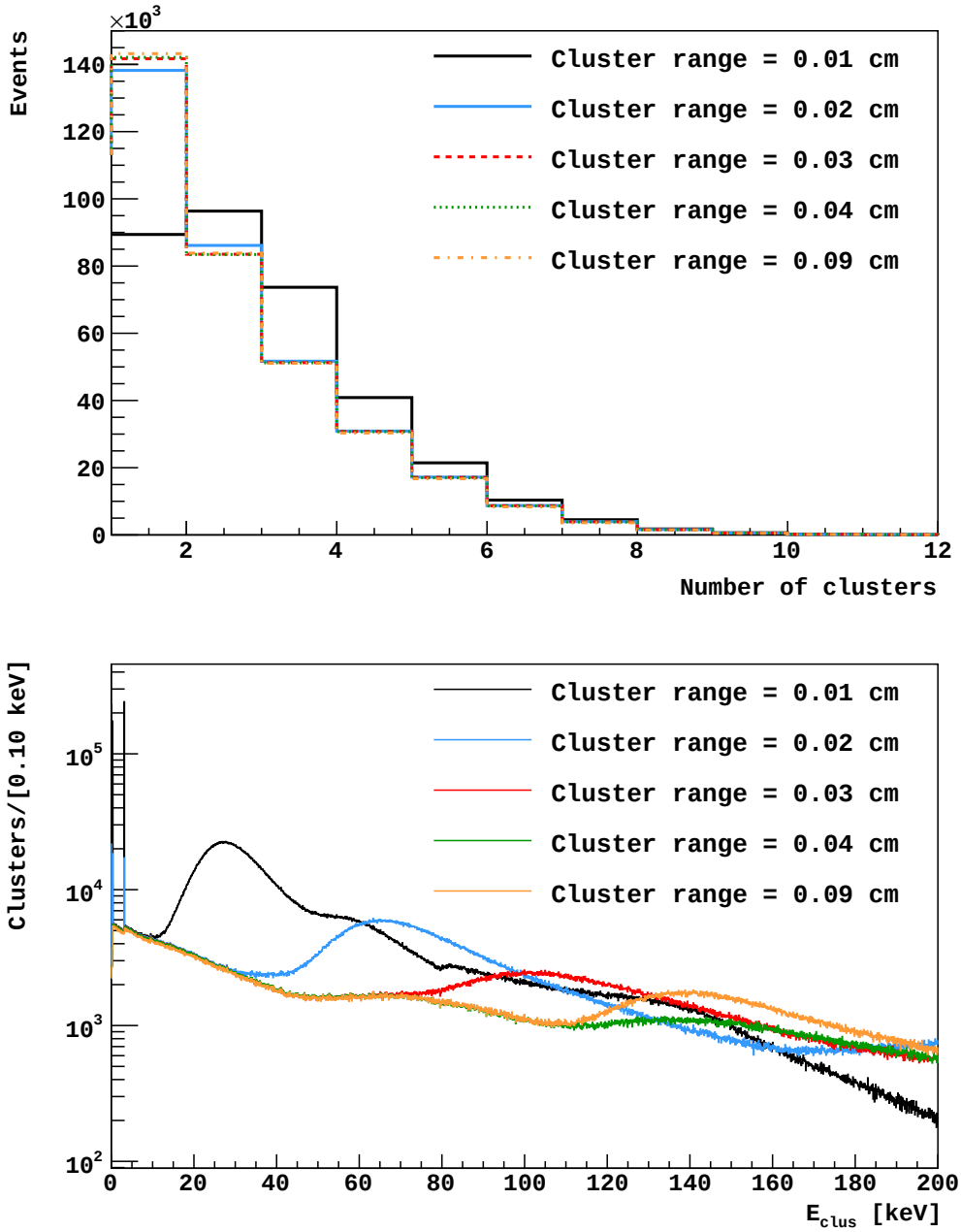

Figure 5.3: **Top:** Cluster multiplicity of simulated $^{60}\mathrm{Co}_{\mathrm{cryo}}$ events, with <200 keV total cluster energy, corresponding to various clustering ranges. **Bottom:** Cluster energy of simulated $^{60}\mathrm{Co}_{\mathrm{cryo}}$ events, with various clustering ranges. Since ^{60}Co-decay does not emit low energy x-rays, the spikes at low energy (<5 keV) indicate that cluster ranges of 0.01 cm and 0.02 cm were incorrectly breaking up single-sited events.

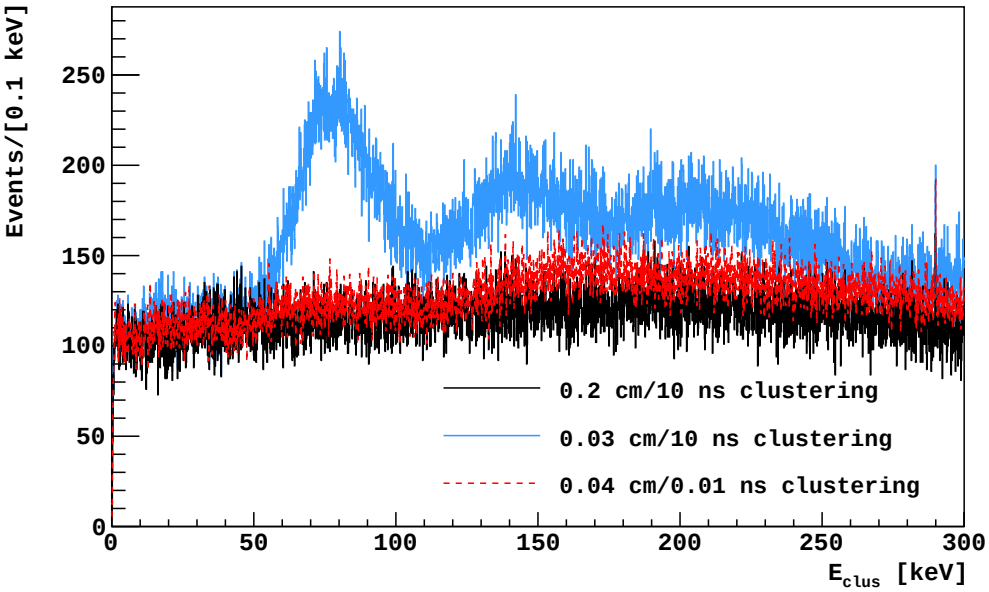

Figure 5.4: Cluster energy of simulated ^{39}Ar events, with various clustering thresholds.

- **Reconstructing the number of pulses.** Simulated events with at least 1 scatter in the active argon were reconstructed to have

$$\texttt{npulses = n\_s2\_pulses + 1} \tag{5.4}$$

where `n_s2_pulses` is the number of S2 pulses for the event, as determined by the multiple-S2 resolution, and the extra pulse was added to account for the expected S1 signal. We note that simulated events with a Cherenkov signal but no scatters in the active argon have `n_s2_pulses = 0`, and thus `npulses = 1`.

- **Reconstructing the drift time.** The drift time for a simulated event was constructed to be

$$\texttt{tdrift = max\_s2\_z / v\_drift} \tag{5.5}$$

where `max_s2_z` is the z-position of the highest scatter after applying the clustering and multiple-S2 resolution, and `v_drift` $= (0.93 \pm 0.01)\,\mathrm{mm\,\mu s^{-1}}$ is the drift velocity with a $200\,\mathrm{V\,cm^{-1}}$ drift field [23].

5.4.1 Developing a multiple-S2 resolution analogue

The performance of the actual data processing's (`darkart v2_00_03`) pulse-finding algorithm with various S2 sizes and time separations ΔT between them was studied using the DS-50 electronics simulation [34, Sec. 3.7]. Event waveforms were simulated, each comprising of one S1 pulse, and two S2 pulses separated by ΔT µs, overlaid on baseline signals from data acquired with a pulser trigger. In detail, the following settings were used for the electronics simulation:

- Baseline from pulser Run 8834.
- One S1 pulse in mode 0 (1 PE per PMT), with signal delay 0.004 µs. The signal delay is the timing offset between the trigger time of the baseline signal (taken from data), and where the pulse will be simulated.
- One S2 pulse in mode 2 (500-5000 PE total—to roughly correspond with the expected size of NR S2's in the WIMP search energy range—, picked from a uniform distribution), with signal delay 30 µs.
- A second S2 pulse in mode 2 (500-5000 PE total, picked from a uniform distribution; the seed for this random variable is different from the one used in the previous step), with signal delay 30+ΔT µs.

These simulated event waveforms were then processed by `darkart` like regular data would be.

The efficiency of the pulse-finding algorithm at successfully identifying these as 3-pulse events is presented in Fig. 5.5, which narrowed sensible z-separation thresholds

to the range of (3-6) µs × 0.93 mm µs^{-1} = 2.79-5.58 mm. The pulse multiplicity (which counts the S1 pulse) from ^{57}Co source calibration data, and from corresponding simulations with 2.79, 3.72, 4.65, and 5.58 mm S2 resolutions (corresponding with drift time separations of 3, 4, 5, and 6 µs respectively), is shown in Fig. 5.5. ^{57}Co decays via electron capture, which emits a 122 keV γ-ray with an intensity of 85.6% [44]; thus, it is a source of Compton scatters that covers the WIMP search S1 range.

Based on Fig. 5.5, a z (drift time) separation threshold of 4.65 mm (5 µs) was chosen, *i.e.*, clusters within this range of each other were deemed to have unresolved S2's.

Figure 5.6 shows the effect of varying the S2 resolution in the case of the 530d UAr (using the activities in Tab. 3.3 for normalization among the various backgrounds). Varying the model's S2 resolution as shown has a small impact (∼1%) on the number of simulated 2- and 3- pulse events. However, we see in all cases that the model systematically predicts more 2-pulse and less 3-pulse events relative to the data; this is a ∼2% effect. Systematics from varying the S2 resolution will be studied in Sec. 5.11.

5.5 Obtaining the amount of cluster energy going into scintillation

Scattering in the LAr produces excitons and ions, both of which result in scintillation. Since the scintillation process involving ions requires recombination with electrons, the application of a drift field has a quenching effect on the scintillation as it separates the ions and electrons. The track length of the recoil particle has also been theorized to affect the ion-electron recombination probability [54, 56].

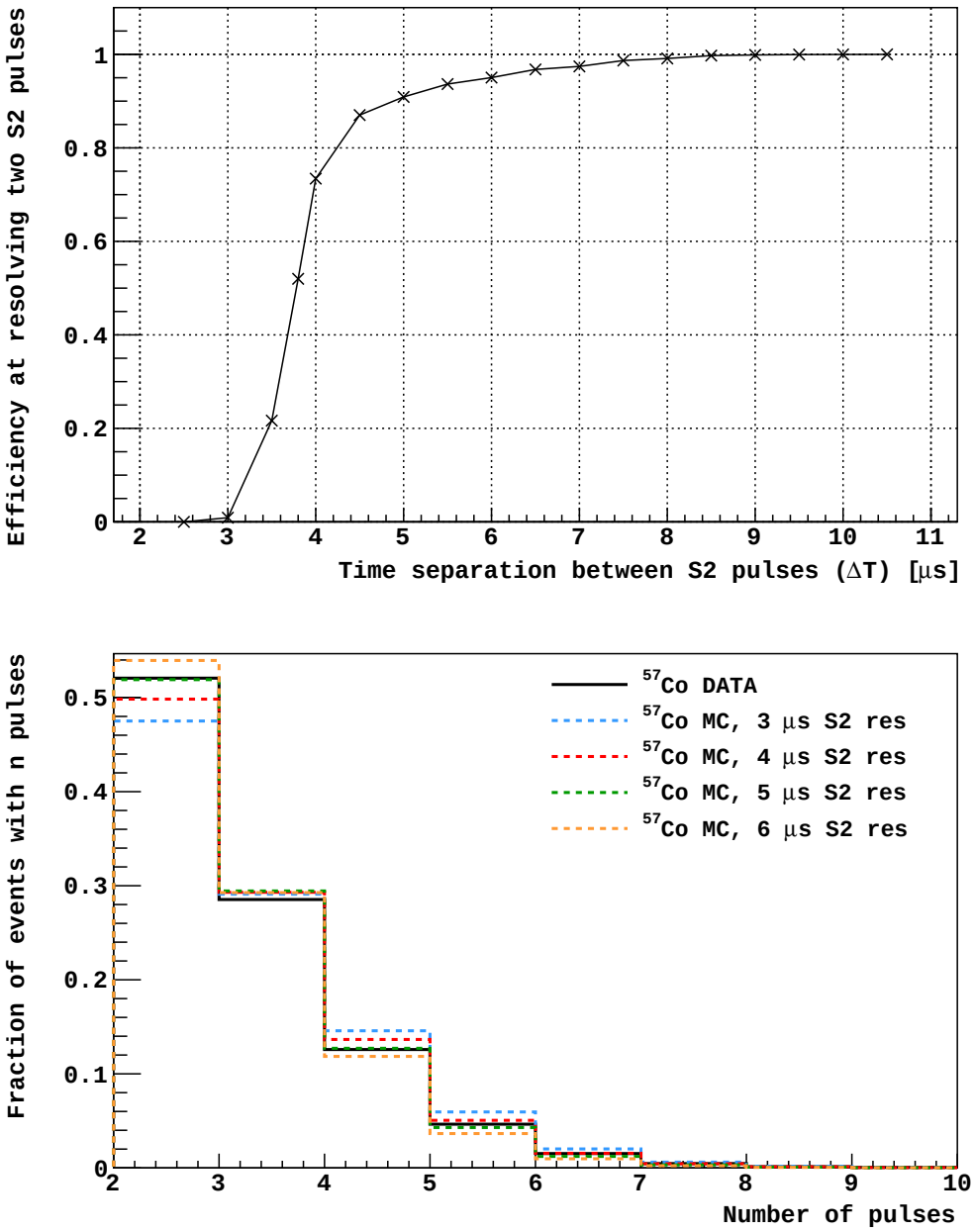

Figure 5.5: **Top:** Efficiency of the pulse-finding algorithm at successfully resolving simulated events with two S2 pulses, with various time separations ΔT between them. Generated with the electronics simulation; the S2 pulses were independently randomly picked from a 500-5000 PE uniform distribution. **Bottom:** Pulse multiplicity from ^{57}Co source calibration data, and from simulations with 2.79, 3.72, 4.65, and 5.58 mm S2 resolutions (corresponding with drift time separations of 3, 4, 5, and 6 μs respectively). Counted were events passing basic quality cuts (Sec. 4.1) with drift time >10 μs. Plots have been normalized to have equal integrals in the pulse multiplicity range shown.

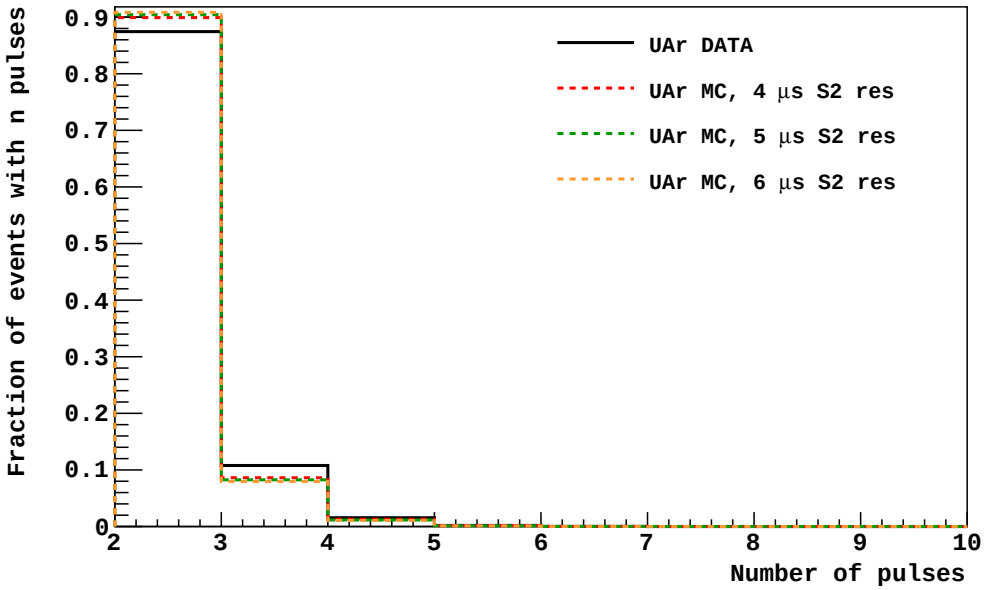

Figure 5.6: Pulse multiplicity distribution from 530d UAr data, and from simulations with 3.72, 4.65, and 5.58 mm S2 resolutions (corresponding with drift time separations of 4, 5, and 6 µs respectively). Counted were events passing basic quality cuts (Sec. 4.1), after 40 µs fiducialization (Sec. 4.4.1), passing the S1 prompt maximum fraction cut (Sec. 4.6.2), and with $100 < \text{S1} < 200$ PE. Plots have been normalized for equal integrals in the displayed range.

To obtain E_{scin} from E_{clus}, a function (obtained via a fit to data) for deriving the ion-electron recombination probability R was used [57, Sec. 3.3.3][3]:

$$R = p_0 \times (1 - p_1 e^{E_{\text{clus}} p_2}) \times e^{p_3 E_{\text{clus}}^{p_4}} + p_5 \tag{5.6}$$

where E_{clus} is in keV, and the values for p_i are summarized in Table 5.1. Then

$$E_{\text{scin}} = E_{\text{clus}} \times \frac{\alpha + R}{1 + \alpha} \tag{5.7}$$

where $\alpha = 0.21$ is the excitation-to-ionization ratio [54], and $\frac{\alpha+R}{1+\alpha}$ is the scintillation fraction.

[3] Further work has since been done to this, leading to the functional form presented in [54, Sec. 5] (not used here).

Table 5.1: Values for parameters used in the ion-electron recombination probability function, Eqn. 5.6.

p_0	p_1	p_2	p_3	p_4	p_5
0.296766	3.95496	−0.517812	−0.0138485	0.912436	0.661046

5.6 Obtaining S1 from the scintillation energy

A constant scale factor of $8.057\,\mathrm{PE/keV}_{E_{\mathrm{scin}}}$ was applied to obtain $\mathrm{S1}_{\mathrm{true}}$ from E_{scin}. This was calibrated so that the (9.4+32.1) keV signal from $^{83\mathrm{m}}$Kr returned an $\mathrm{S1}_{\mathrm{true}}$ of 302.6 PE [58]. Doing so resulted in $\mathrm{S1}_{\mathrm{true}}$ of 14.9 PE for the 2.6 keV signal from ^{37}Ar and 787.1 PE (870.6 PE) for the 122 keV (136.5 keV) signal from ^{57}Co (Fig. 5.7). The overall light yield (in $\mathrm{PE/keV}_{E_{\mathrm{clus}}}$) *vs.* $\mathrm{S1}_{\mathrm{true}}$ is shown in Fig. 5.8.

Various measurements of the light yield (performed by Fitzpatrick [59], Hackett [39], Pagani [40], and Wada [58]) using ^{37}Ar and/or $^{83\mathrm{m}}$Kr are also presented in Fig. 5.8. Since these measurements could not resolve the two-stage decay of $^{83\mathrm{m}}$Kr, the light yields they report at 41.5 keV are higher than the modeled value, which reflect the higher light yields at 9.1 keV and 23.1 keV instead. We note that the modeled light yield at 2.6 keV was lower than the values measured using the ^{37}Ar peak; this will be considered in our study of systematics later (Sec. 5.11).

5.7 Smearing S1

To simulate statistical fluctuations in detected S1, $\mathrm{S1}_{\mathrm{true}}$ was smeared the following way:

- If $\mathrm{S1}_{\mathrm{true}}<20$ PE, $\mathrm{S1}_{\mathrm{smeared}}$ was drawn at random from a Poisson distribution with mean $\mathrm{S1}_{\mathrm{true}}$.

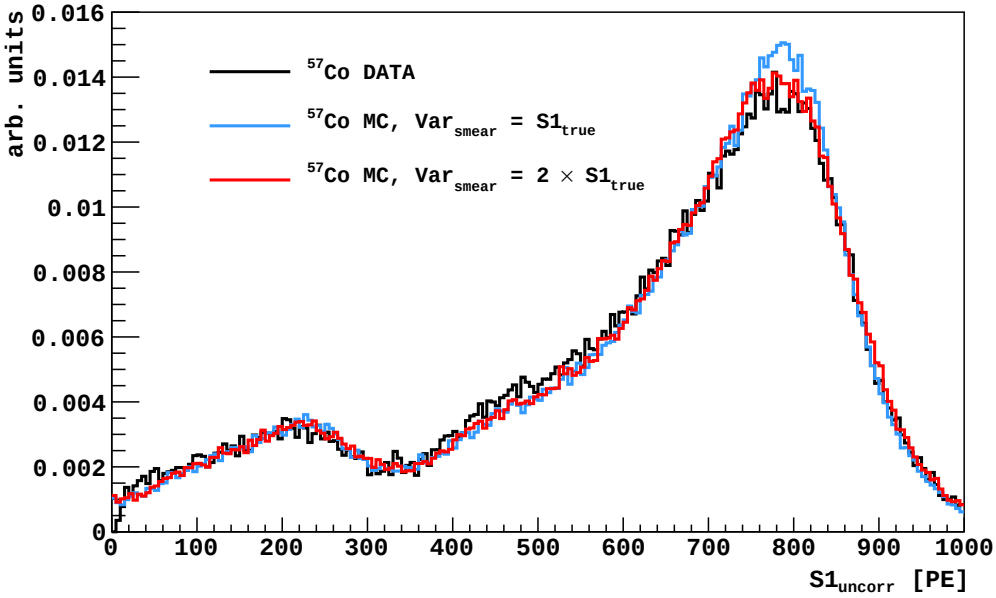

Figure 5.7: $\mathrm{S1_{uncorr}}$ spectra of ^{57}Co from source calibration data and simulations with different smearing parameters $\mathrm{Var_{smear}}$. Spectra have been normalized to have unit integral for $100 < \mathrm{S1_{uncorr}} < 1000\,\mathrm{PE}$.

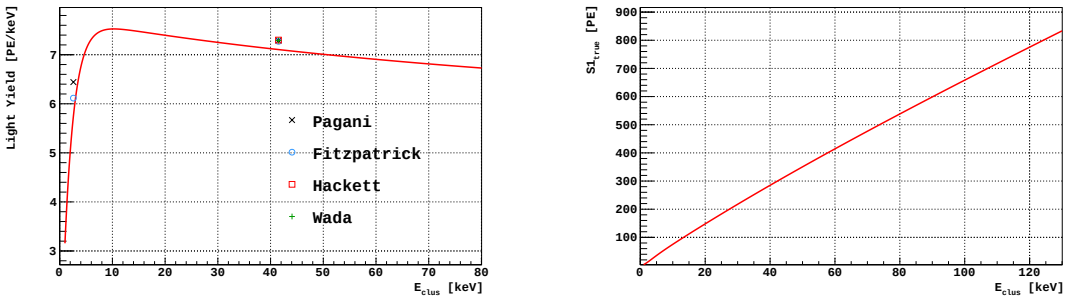

Figure 5.8: **Left:** Overall light yield (in $[\mathrm{PE/keV}_{E_{\mathrm{clus}}}]$) *vs.* E_{clus}, with a $200\,\mathrm{V\,cm^{-1}}$ drift field. Light yields measured using the ^{37}Ar (2.6 keV) and $^{83\mathrm{m}}$Kr (41.5 keV) peaks in data [59, 58, 40, 39] are also shown. **Right:** Consequent $\mathrm{S1_{true}}$ *vs.* E_{clus}.

- If $S1_{true}$>20 PE, $S1_{smeared}$ was drawn at random from a Gaussian distribution with mean $S1_{true}$ and variance ($2 \times S1_{true}$); this variance was the result of studies using the ^{57}Co spectrum (Fig. 5.7).

5.8 Looking up F90

For each scatter, an F90 was drawn from an appropriate reference F90 profile using its $S1_{smeared}$:

- If $S1_{smeared}$>10 PE, F90 was drawn from the F90 profile of the corresponding S1 bin in a reference made from the AAr data. See Sec. 5.8.1 for selection criteria on the reference data.

- If $S1_{smeared}$<10 PE, a uniform distribution between 0 and 1 was used as the F90 profile. See Sec. 5.8.2 for details.

5.8.1 Selecting AAr data for use as an F90 reference

Since the aim was to use the AAr data as an F90 reference for single-scatter ERs, an effort was made to maintain large statistics in the data set, *i.e.*, to apply as few cuts as possible, while removing non-single-scatter ERs from the sample. These cuts were chosen by studying the response of the AAr event count in a strip of F90, for $10 < S1 < 500$ PE (Fig. 5.9). We began with the basic event selection criteria:

1. **For event quality:** All 38 PMT channels present; Baseline found on the event waveform; No saturated pulses; Event livetime <1 s.

2. **To ensure the first pulse is an S1:** Event livetime >400 µs; S1 start time matches the expected trigger time; F90 of the S1 pulse >0.05.

3. **To select single-scatter events:** Event has exactly 2 pulses, or exactly 3 pulses with an identified S2-echo.

4. **To ensure the second pulse is an S2:** F90 of the S2 pulse <0.2; xy-corrected S2 >100 PE.

5. **Fiducialization:** Drift time >10 µs. (A minimal drift time cut like this is necessary to remove events with potential S1-S2 pileup.)

First, we checked if a cut targeting events with a fused silica Cherenkov component for removal was necessary. In particular, we implemented the S1 prompt maximum fraction (S1pmf) cut, which had been designed using ^{241}AmBe source calibration data to remove the 5% of events with S1 that was most concentrated in a single PMT. The fraction of events selected by the criteria listed above (1 through 5) and surviving the S1pmf cut is presented in Fig. 5.9. We see that the cut's rejection in the high F90 test strip was higher than its rejection over the full range of F90; this indicated that it was indeed removing non-single-scatter ERs from the AAr as desired, which motivated its use in the selection of the reference data:

6. **To remove events with a fused silica Cherenkov component:** Passing 95th-percentile S1pmf cut.

Next, we checked if additional fiducialization from the bottom of the TPC was necessary. To do so, we implemented a 10 µs drift time cut from the bottom of the TPC, *i.e.*, requiring that drift time <366 µs. The fraction of events selected by the criteria listed above (1 through 6) within this smaller fiducial volume is shown in Fig. 5.9. We see that the fraction of events removed by this cut corresponded with the reduction in fiducial volume. This indicated that events in the data sample before this additional fiducialization were already uniformly distributed in z, which was consistent with them being ^{39}Ar events in AAr.

As it is dominated by single-scatter ERs from ^{39}Ar β-decay, a reference selected using criteria 1 through 6—shown in Fig. 5.10—should have been sufficient for modeling the majority of our F90 distributions. However, because the eventual goal was

to make a background prediction at high F90, even lone contaminant events in the reference could be problematic. In particular, several such events can be seen in Fig. 5.10, at ∼80 PE, ∼130 PE, ∼160 PE, ∼220 PE, and ∼300 PE. Given the available statistics in the reference and the anticipated rate of single-scatter events, it was estimated that each of these outlier events could contribute 0.05-0.1 event worth of background in 500 d of UAr running, which would have made them the driver of predicted ER background in any WIMP search region. Having such outliers drive the background prediction would be correct only if they were truly single-scatter ERs. Thus, we implemented the full suite of AAr analysis cuts [23], which were developed to remove non-single-scatter ER events:

7. **More aggressive fiducialization:** 40 µs < drift time < 334.6 µs.

8. **Veto cuts:** Passing all AAr analysis veto cuts.

The S1 *vs.* F90 of reference AAr events selected using criteria 1 through 8 in Sec. 5.8.1 is shown in Fig. 5.11. Since the selection criteria have been well-documented, and were necessary, systematics from changing the reference were not studied.

5.8.2 F90 model for low S1 scatters

Although single-sited events with low S1 (<60 PE) were outside the S1 range of interest, multi-sited events could have low-energy component scatters, and so it was necessary to model such scatters.

The data reference could not be used at low S1 (<10 PE) because it eventually ran out of statistics when triggering conditions could no longer be met. In addition, the multiplicity requirement on the trigger imposed a bias on recorded low S1 events—*i.e.*, since the AAr trigger required signals seen in three PMTs (instead of two in UAr running), a 10 PE event needed to have F90$\gtrsim$0.3. The choice to model F90 of such scatters using a uniform distribution was arbitrary. The impact of this choice of

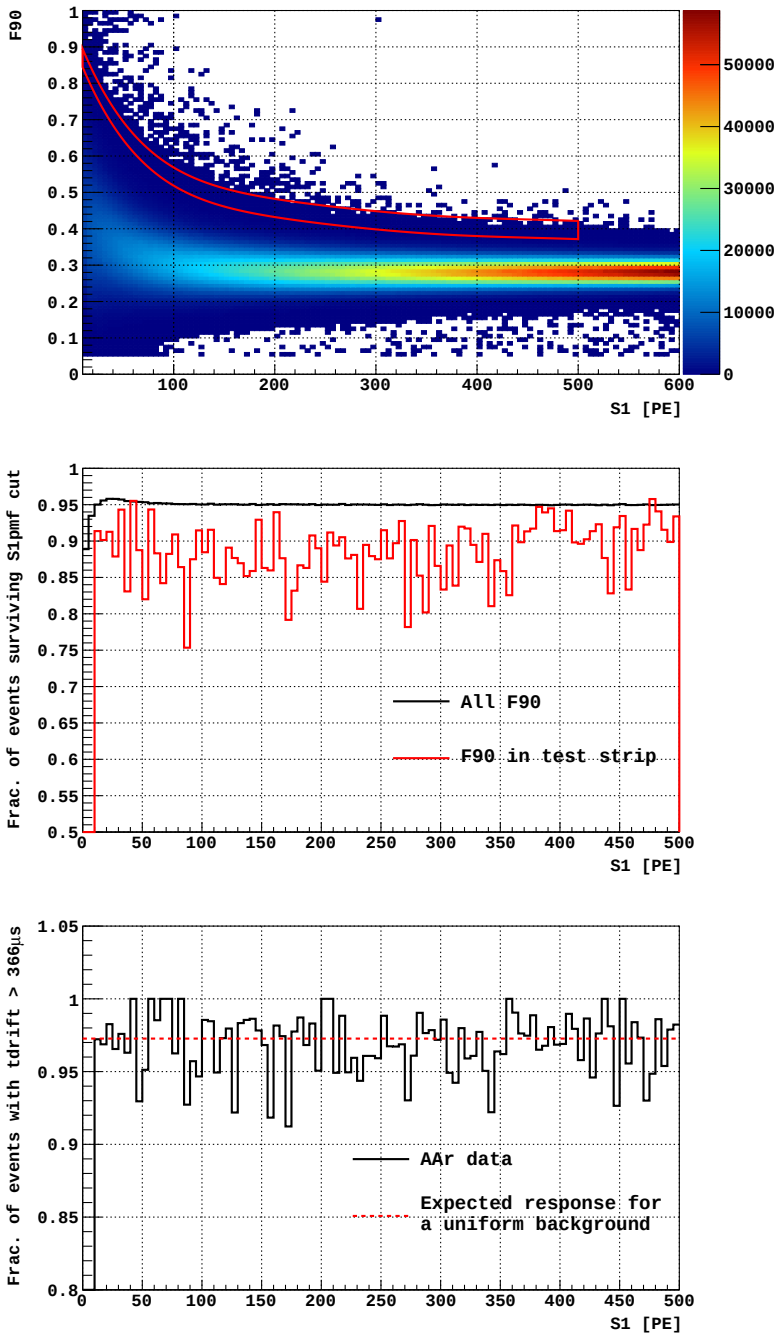

Figure 5.9: **Top:** F90 *vs.* S1 of AAr data events with minimal selection criteria (1 through 5), overlaid with a test strip in red for event counting. **Middle:** Fraction of events remaining after applying the S1 prompt maximum fraction (S1pmf) cut. **Bottom:** Fraction of test region events surviving a drift time <366 µs fiducialization.

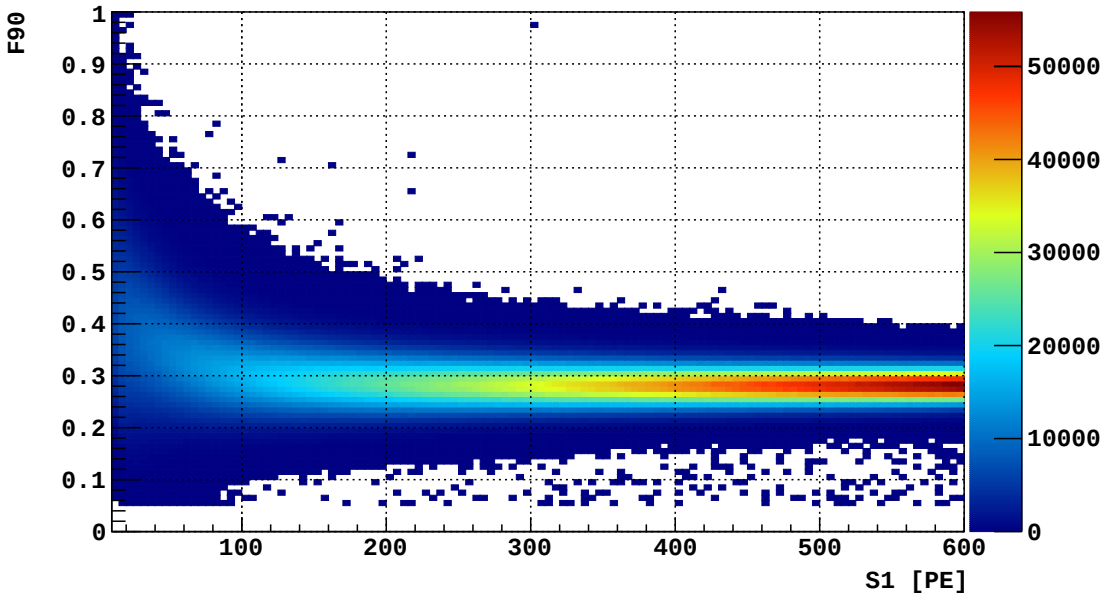

Figure 5.10: F90 *vs.* S1 of AAr data events with minimal selection criteria, and the S1pmf cut (1 through 6 in Sec. 5.8.1).

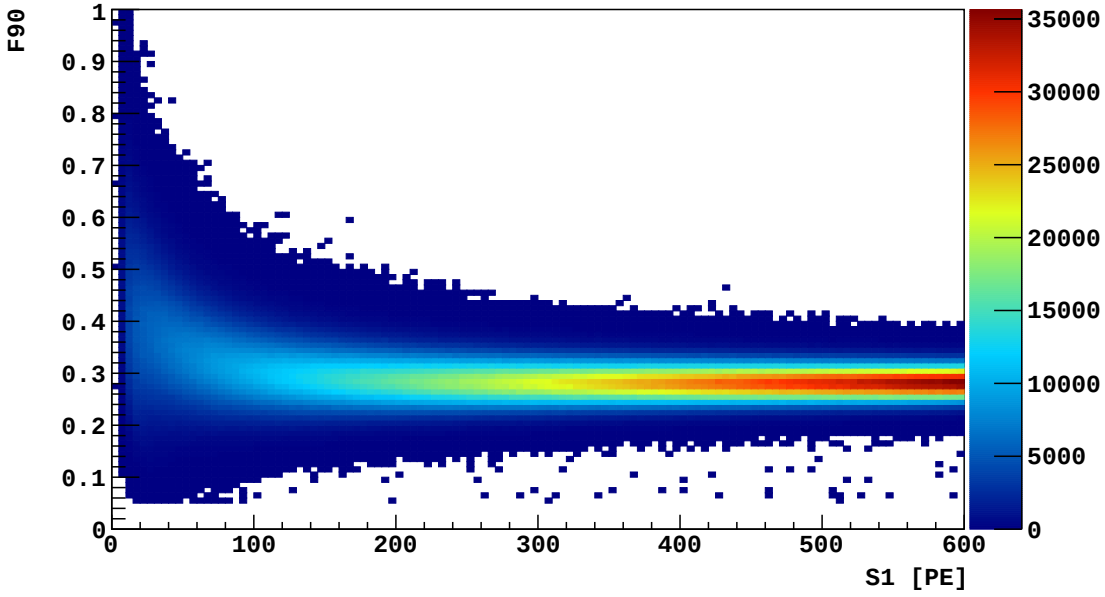

Figure 5.11: F90 *vs.* S1 of AAr data events used as the model's F90 reference.

model was studied by assuming extreme F90 (*i.e.*, 0 or 1) for such scatters, and will be reported later.

5.8.3 Spectral dependence of F90

The F90 for a modeled event is drawn from the S1 bin of the reference histogram (Fig. 5.11) that contains $S1_{smeared}$ (instead of $S1_{true}$) for two reasons: 1) $S1_{true}$ is never accessible in data, and hence S1 in the data is directly analogous to $S1_{smeared}$; and 2) This procedure ensured that the modeled F90 *vs.* S1 for ^{39}Ar matched that from AAr data.

A consequence of this was that for single-sited events, the modeled F90 profile in an $S1_{smeared}$ bin was just a sampling of the F90 profile in the corresponding S1 bin of the reference data. Thus, we had to check that the F90 distribution in any S1 bin of AAr data (the reference) was a good approximation for that in the corresponding bin of UAr. This was not obviously true—as F90 is energy-dependent, since the AAr and UAr had different recoil energy spectra, the mix of energies and consequent F90 distributions in each S1 bin would be different for AAr and UAr.

Method

A toy Monte Carlo was used to investigate the impact of this spectral dependence of F90, following these steps:

1. Approximate AAr and UAr recoil energy spectra were obtained by fitting (with polynomials) their respective two-pulse S1 spectra, and dividing by an approximate light yield of 7 PE/keV (Fig. 5.12). Since this was done for the 530d UAr analysis, the ^{37}Ar peak was not included in the UAr spectrum. For each spectrum, an energy E was picked using the spectrum as a probability distribution.

2. $\mathrm{S1_{true}}$ was obtained from E using a light yield of 7 PE/keV.

3. $\mathrm{S1_{true}}$ was smeared to get $\mathrm{S1_{smeared}}$:

$$\begin{aligned} \mathrm{S1_{smeared}} &= \mathrm{Pois(S1_{true})\ for\ S1_{true} < 20} \\ \mathrm{S1_{smeared}} &= \mathrm{Gaus(Mean = S1_{true}, Var = S1_{true})\ for\ S1_{true} \geq 20} \end{aligned} \tag{5.8}$$

4. A mean F90 was gotten from a toy F90 *vs.* E function:

$$\mathrm{F90_{mean}} = 0.205563 \times e^{-E/7.16924} + 0.279701 \tag{5.9}$$

that was obtained from a rough fit of the AAr $\mathrm{F90_{mean}}$ *vs.* S1, and dividing by the 7 PE/keV light yield (Fig. 5.12).

5. $\mathrm{F90_{mean}}$ was then smeared using:

$$\mathrm{S1_{prompt}} = \mathrm{Gaus(Mean} = np, \mathrm{Var} = np(1-p)) \tag{5.10}$$

where $n = \mathrm{S1_{true}}$ and $p = \mathrm{F90_{mean}}$, i.e., assuming $\mathrm{S1_{prompt}}$ follows a binomial distribution.

6. A histogram was filled using ($\mathrm{S1_{smeared}}$, F90).

7. Steps 1 through 6 were repeated to generate a large number of events (here 10^9) per spectrum.

The impact of the possible spectral dependence of F90 was then judged using the following metrics:

- The relative placement of toy AAr and toy UAr F90 contours admitting n "leakage events" (*i.e.*, events lying above the F90 contour) per S1 bin.

- The impact on the number of leakage events if the contour drawn on the toy AAr F90 *vs.* S1 distribution was applied to the UAr distribution.

Impact on F90 contour placement

We chose to first normalize the output from the toy simulation to match the event count in the 70d UAr data: with 40 µs drift time fiducialization applied, there were $\sim 3.32 \times 10^5$ two-pulse events with $0 < \text{S1} < 600$ PE in the data, corresponding to $\sim 8.15 \times 10^9$ events in the toy UAr simulation. Accordingly, the simulated data were normalized by a factor of $3.32 \times 10^5 / 8.15 \times 10^9 = 4.07 \times 10^{-5}$. After this normalization, the F90 contour admitting 0.01 leakage events/[S1 bin]—*i.e.*, events with F90 higher than the contour—was found on the toy UAr F90 *vs.* S1 distribution.

A modified procedure was used to draw an F90 contour on the toy AAr events for comparison. This is because although the same number of *total* events was generated in both toy simulations, the number of events *in each S1 bin* was spectrum-dependent. This discrepancy in bin event counts had to be accounted for as it contributed to the width of that S1 bin's F90 distribution. We did this by first normalizing the event count in each S1 bin of the toy AAr F90 *vs.* S1 histogram to match that in the corresponding bin in the toy UAr; after this was done, the F90 contour admitting 0.01 leakage events/[S1 bin] was drawn, as was done on the toy UAr distribution.

Both F90 contours are shown in Fig. 5.13. We observe the following: 1) For S1 <10 PE, both contours are at F90 = 1 because the F90 distributions at low S1 were just that wide—*i.e.*, the highest bin of F90 (spanning 0.9999 to 1) contained more than 0.01 events. 2) In each S1 bin, the separation between the contours (ΔF90) was small (<0.003).

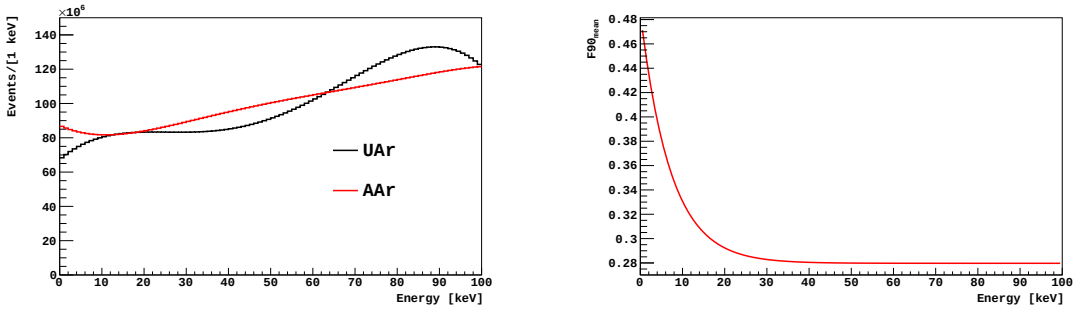

Figure 5.12: **Left:** Approximate AAr and 530d UAr energy spectra used in the toy simulation. **Right:** $F90_{\text{mean}}$ vs energy function used in the toy simulation.

Impact on leakage events

Figure 5.13(bottom) shows the change in leakage event count when the toy AAr-driven contour was applied on the toy UAr events instead of the toy UAr-driven contour. We see that the variation in leakage events with this substituton, Δ(leakage events), is consistent with statistical fluctuations.

Based on the small impact on F90 contour placement, and the small consequent effect on the number of leakage events, we concluded that S1 *vs.* F90 drawn from AAr data was a good model for single-scatter ERs in UAr.

Multiple Compton scatters

Next we had to see if the AAr data was a good F90 reference for component scatters in multiple scatter events. In this case, however, kinematic correlations between individual scatter energies made it not particularly meaningful to consider the impact of, *e.g.*, the aggregate spectrum of all n^{th} scatters. Therefore, instead of drawing scatter energies from a toy spectrum (as was done for single-sited events), we began with unresolved two-scatter events generated by G4DS:

1. Paired scatter energies (E_1, E_2) were drawn from the distribution of scatter energies of unresolved two-scatter events generated by G4DS (Fig. 5.14).

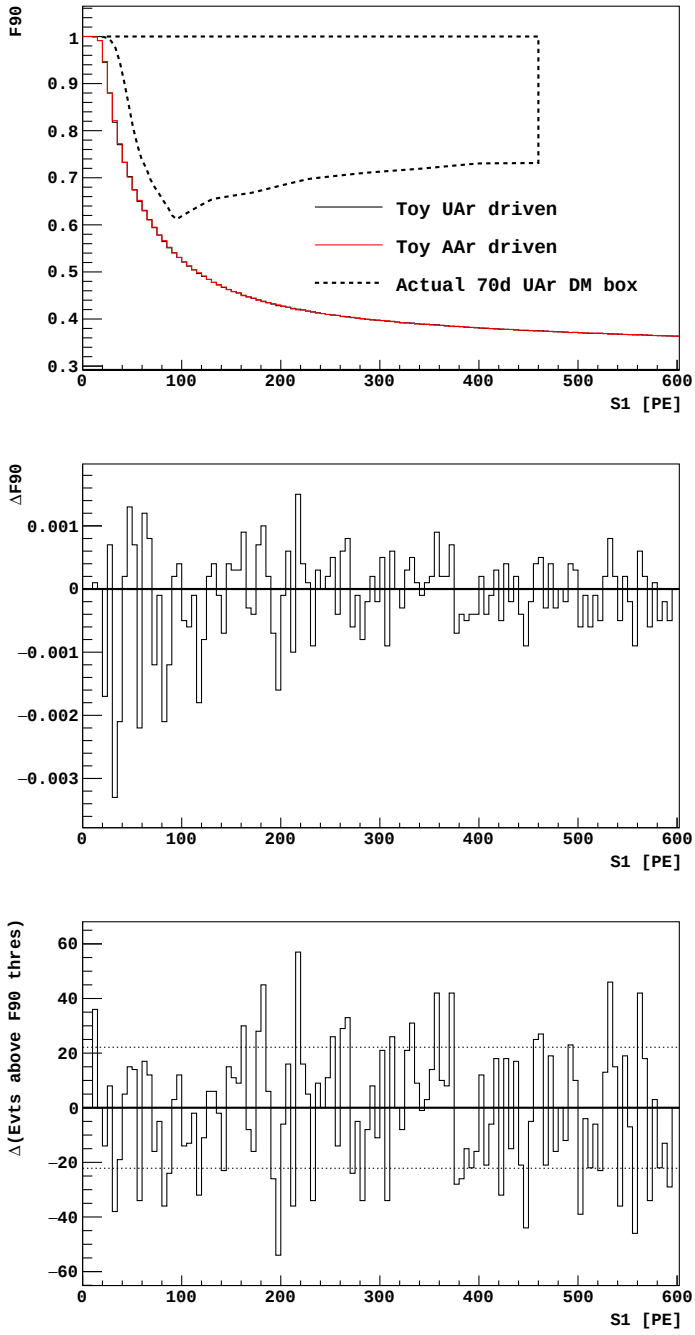

Figure 5.13: **Top:** 0.01 leakage event/[S1 bin] F90 contours, driven by events from the UAr and AAr toy simulations. The actual 70d UAr analysis WIMP search box is also presented for reference. **Middle:** Separation between the UAr and AAr contours (ΔF90) in each S1 bin. **Bottom:** Change in leakage event counts, if the toy AAr-driven contour was applied on the toy UAr events instead of the toy UAr-driven contour. y-axis is in un-normalized toy UAr event counts. Since we expect ∼246 events toy UAr leakage events per S1 bin, the standard deviation on the difference is $\sqrt{2 \times 246} = 22$; a ± 1 standard-deviation band is indicated by the dotted lines.

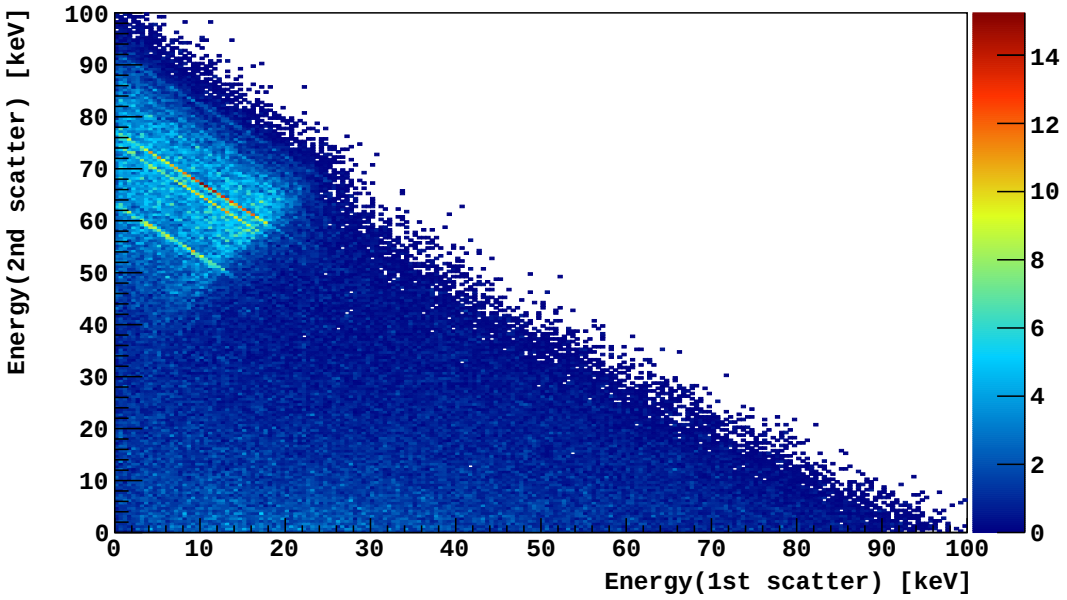

Figure 5.14: Energies of the component scatters in unresolved two-Compton-scatter events (with total energy <100 keV), as generated by G4DS. Notably, the first scatter tends to deposit less energy than the second—this corresponds with smaller scattering angles and further penetration of the γ-ray into the active argon, which presumably increases the probability of a subsequent scatter. γ-lines, *e.g.*, the 77 keV γ-ray from ^{214}Pb decay (part of the lower ^{238}U chain), are visible in the figure.

2. For each scatter i, $\mathrm{S1}^{i}_{\mathrm{smeared}}$ and $\mathrm{F90}_{i}$ were obtained following steps 2 through 5 as described in the case of toy single-sited events.

3. A histogram was filled using $(\mathrm{S1}_{\mathrm{event}}, \mathrm{F90}_{\mathrm{event}})$, where

$$\begin{aligned} \mathrm{S1}_{\mathrm{event}} &= \sum \mathrm{S1}^{i}_{\mathrm{smeared}} \\ \mathrm{F90}_{\mathrm{event}} &= \frac{\sum \left(\mathrm{S1}^{i}_{\mathrm{smeared}} \times \mathrm{F90}_{i}\right)}{\mathrm{S1}_{\mathrm{event}}} \end{aligned} \tag{5.11}$$

These toy two-scatter events were then compared to an S1-driven model for two-scatter events, constructed by referencing the F90 of *toy* AAr events (constructed on pg. 69):

1. Paired scatter energies (E_1, E_2) were drawn from the distribution of scatter energies of unresolved two-scatter events generated by G4DS (Fig. 5.14).

2. For each scatter i, $\mathrm{S1}^i_{\mathrm{smeared}}$ was obtained following steps 2 through 3 as described in the case of toy single-sited events.

3. For each scatter i, $\mathrm{F90}_i$ was drawn using the F90 profile in the corresponding $\mathrm{S1}^i_{\mathrm{smeared}}$ bin of the toy AAr data as a probability distribution.

4. A histogram was filled using ($\mathrm{S1}_{\mathrm{event}}$, $\mathrm{F90}_{\mathrm{event}}$), constructed as described in Eqn. 5.11.

Both sets of toy two-scatter events were then normalized as the toy UAr events were in the previous section. The 0.01 leakage event/[S1 bin] F90 contours, and the separation between these contours, are shown in Fig. 5.15. We observe that for the S1range of interest (>60 PE), the separation between the contours is <0.007.

Figure 5.15 also shows the change in leakage event count when the S1-driven contour was applied on the toy energy-driven two-scatter events instead of the energy-driven contour. Notably, significant fluctuations ($>2\,\sigma$) in Δ(leakage events) were observed; however, a systematic effect was not observed, and the magnitude of the fluctuations were $\lesssim$0.5$\times$ the targeted leakage events per bin. Given that multiple Compton scatter events make up only a small fraction of the UAr events (Fig. 5.6), this was deemed to be acceptable.

5.9 Constructing event S1 and F90

For each cluster/scatter i in a simulated event, we have now obtained a smeared $\mathrm{S1}^i_{\mathrm{smeared}}$ and an $\mathrm{F90}^i$. The S1 and F90 of the event were then constructed as follows:

$$\begin{aligned} \mathrm{S1}_{\mathrm{event}} &= \sum_{i=1}^{n} \mathrm{S1}^i_{\mathrm{smeared}} \\ \mathrm{F90}_{\mathrm{event}} &= \sum_{i=1}^{n} (\mathrm{F90}^i \times \mathrm{S1}^i_{\mathrm{smeared}}) / \mathrm{S1}_{\mathrm{event}} \end{aligned} \tag{5.12}$$

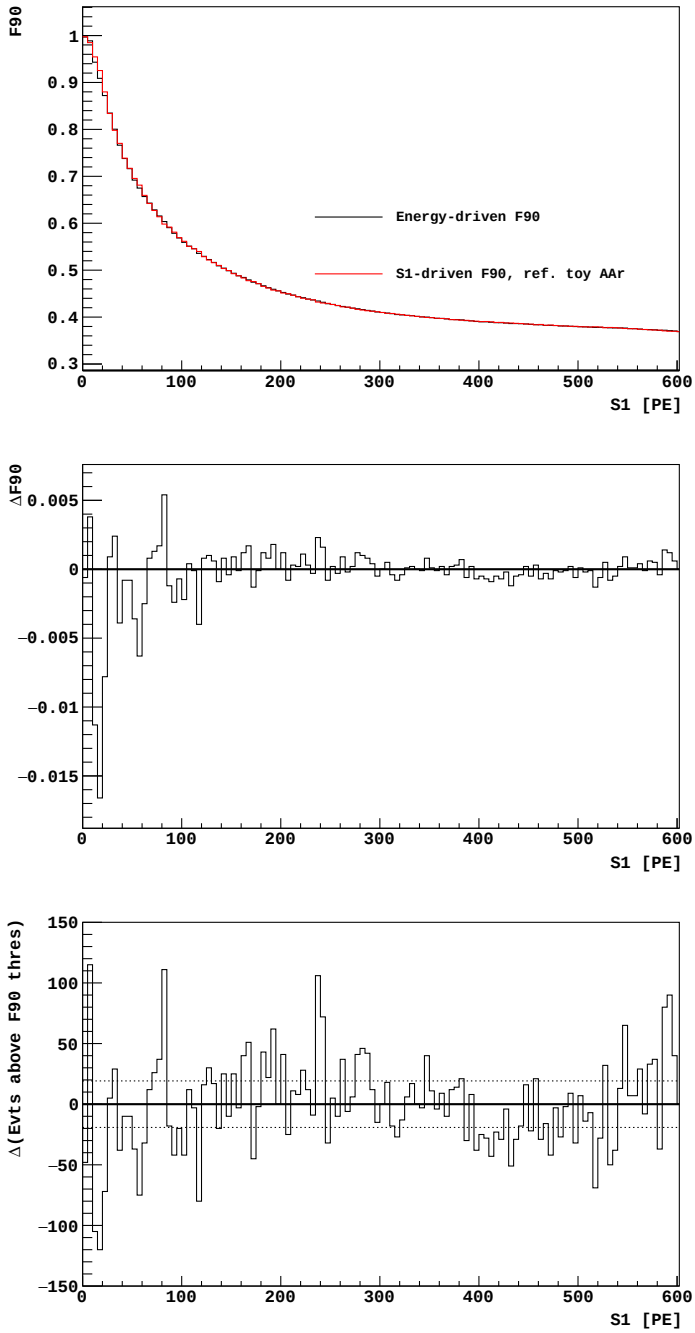

Figure 5.15: **Top:** 0.01 leakage event/[S1 bin] F90 contours, driven by two sets of toy two-scatter events. In one set, F90 for each scatter was driven by that scatter's recoil energy. In the other set, F90 for each scatter was drawn from the toy AAr simulation. **Middle:** Separation (ΔF90) between the two contours in each S1 bin. **Bottom:** Change in leakage event count, if the S1-driven contour was applied on the toy energy-driven two-scatter events instead of the energy-driven contour. The horizontal dotted lines bound a ±1 standard-deviation band for the size of the fluctuations.

where n is the number of clusters/scatters in the event.

5.10 Combining with the Cherenkov model

As mentioned in Sec. 5.2, a model for Cherenkov radiation in the Teflon and fused silica components of the detector was also developed within the G4DS framework (by Xiang). This included optical modeling from the generation of Cherenkov photons, through wavelength shifting by the TPB, to the collection of wavelength-shifted photons by the PMTs, which was finally output as a Cherenkov S1 signal ($\mathrm{S1}_{\mathrm{Cherenkov}}$). If Cherenkov radiation was generated for an event, it was assumed to be entirely prompt (*i.e.*, contained in the first 90 ns); S1 and F90 for the event were thus constructed as such:

$$\begin{aligned} \mathrm{S1}_{\mathrm{event}} &= \sum_{i=1}^{n} \mathrm{S1}^{i}_{\mathrm{smeared}} + \mathrm{S1}_{\mathrm{Cherenkov}} \\ \mathrm{F90}_{\mathrm{event}} &= \frac{\sum_{i=1}^{n} (\mathrm{F90}^{i} \times \mathrm{S1}^{i}_{\mathrm{smeared}}) + \mathrm{S1}_{\mathrm{Cherenkov}}}{\mathrm{S1}_{\mathrm{event}}} \end{aligned} \tag{5.13}$$

5.10.1 S1 light distribution

Since the S1pmf cut was a crucial part of the background mitigation strategy, it was important to also handle the S1 light distribution in our modeling. As mentioned in Sec. 5.2, the simulation's output fell into two classes:

- Events with no Cherenkov radiation component were simulated without photon generation. For such events, we simply assumed that the measured acceptance of the S1pmf cut on uniformly distributed ^{39}Ar events (Sec. 4.6.2) would apply, and accounted for the cut's application by scaling the simulated events with a factor of 0.95.

- Events with Cherenkov radiation were simulated with photon generation and propagation in both the Cherenkov and argon scintillation components—*i.e.*,

$S1^{G4DS}_{Cherenkov}$ and $S1^{G4DS}_{scintillation}$ were generated, along with information about their light distribution among the PMTs. $S1^{G4DS}_{Cherenkov}$ was included in the model without further processing (*i.e.*, it *is* $S1_{Cherenkov}$ in the previous section). Each photoelectron in $S1^{G4DS}_{scintillation}$ was randomly chosen to be a prompt photoelectron with a binomial probability of the scintillation component's F90—*i.e.*, that in Eqn. 5.12. The distribution of these prompt photoelectrons and the Cherenkov photoelectrons across the PMTs was then used to construct S1pmf for the event.

5.11 Model systematics

Since the eventual goal was to make a background prediction in the WIMP search region (*i.e.*, a high F90 region), model systematics were estimated by studying the response of predicted event counts to variations in the following model parameters:

- **Clustering range:** The threshold for clustering simulated deposits into a scatter in the active argon was set at 0.04 cm (Sec. 5.3). The effect of using thresholds of 0.03 cm and 0.2 cm instead were studied.

- **S2 resolution:** The drift time separation for two S2 pulses to be resolved was set at 5 µs (Sec. 5.4.1). The effect of using drift time separations of 4 µs and 6 µs instead were studied.

- **Recombination, light yield, and S1 smearing:** Figure 5.8 shows how various light yield measurements differed from the model's light yield. In particular, the light yield measured by Pagani [40, Tab. 3.3] using the ^{37}Ar S1 peak was ∼12% higher than the value used in the model. This was used as a possible upward variation of the light yield for the study of systematic effects. Since the model's light yield was already on the low end with respect to both measurements made with the ^{37}Ar peak, no systematics were attributed to possible reductions in the light yield.

- **F90 model for LAr scatters with S1<10 PE:** F90 for these events were modeled with a uniform distribution, bound at 0 and 1, which was arbitrarily chosen (Sec. 5.8.2). The effect of assuming all such scatters having F90 of 1 or 0 instead were studied.

Events were counted in a modified version of the 70d UAr WIMP box (with its lower F90 bound translated downward by 0.02 and its upper bound lowered to 0.84, and for $60 < \mathrm{S1} < 300\,\mathrm{PE}$). This region in F90 *vs.* S1 was chosen to ensure sufficient simulation statistics for counting, while staying in the neighborhood of the final WIMP box.

The model's response to the variations are summarized in Tab. 5.2. In particular, the measured systematics ranged from +20% to −3%. The model variations were Monte Carlo simulations of ∼1000 d worth of UAr event statistics, so the statistical error on their respective predictions is ∼13%. With the chosen cuts, 94% of the predicted ER event count in the test region (using the default parameters) had a Teflon Cherenkov component; this was chosen because such events were anticipated to be the most problematic ER background (Sec. 4.7.2). We note that the variations were done separately, *i.e.*, there was no measure of correlations between the model parameters.

5.12 Validation against 70d UAr data

5.12.1 Single-scatter events

F90 profiles of single-scatter—*i.e.*, two-pulse—events with 40 µs drift time fiducialization and passing the S1pmf cut, from 70d UAr data and from the model, are shown in Fig. 5.16. To account for the activity estimates not getting the event rate exactly right (Fig. 3.7)[4], the model was first scaled (by a factor of 1.07) so that its event rate for

[4] Recall that the fitting process only went down to 50 keV, or ∼370 PE.

Table 5.2: Predicted event counts in 500 d of UAr running using different variants of the ER F90 model. Events were counted in a modified version of the 70d UAr WIMP box (with its lower F90 bound translated downward by 0.02 and its upper bound lowered to 0.84, and for $60 < \mathrm{S1} < 300$ PE). Basic event quality and topology cuts, a 40 µs drift time fiducialization, and the S1 prompt maximum fraction cut were applied to the simulated events. Presented statistical errors are derived from the available simulation statistics for each model variant.

Configuration	Event count	Configuration	Event count
Default parameters	$29.1(\pm 0.7)_{\mathrm{stat}}$		
0.03 cm clustering	$32(\pm 4)_{\mathrm{stat}}$	0.2 cm clustering	$33(\pm 4)_{\mathrm{stat}}$
4 µs S2 resolution	$33(\pm 4)_{\mathrm{stat}}$	6 µs S2 resolution	$35(\pm 4)_{\mathrm{stat}}$
1.12 × model LY	$29(\pm 4)_{\mathrm{stat}}$		
F90(S1<10)=0	$28(\pm 3)_{\mathrm{stat}}$	F90(S1<10)=1	$30(\pm 4)_{\mathrm{stat}}$

$60 < \mathrm{S1} < 460$ PE matched that observed in the 70d UAr data. As a goodness-of-fit metric, the Pearson χ^2 was computed over bins i with ≥5 model entries:

$$\chi^2 = \sum_i \frac{(O_i - E_i)^2}{E_i} \tag{5.14}$$

where O_i is the observed number of entries (*i.e.*, from data) in bin i, and E_i is the expected number of entries (*i.e.*, from the model) in bin i. As we are interested in the high F90 region, only bins above the (mean+rms) of the model profile went into the χ^2 calculation. The degrees of freedom (ndf) associated with this χ^2 was the number of bins contributing to the sum. The p-values indicated that the model was consistent with the data on the high side of the F90 profiles.

5.12.2 Three-pulse events

The original motivation for developing the model (*i.e.*, before we realized in the course of the 70d UAr analysis that ERs with a Teflon Cherenkov component would be the main background) was to account for multiple-scatter events. In particular, events consisting of multiple Compton scatters in the active argon were expected to have

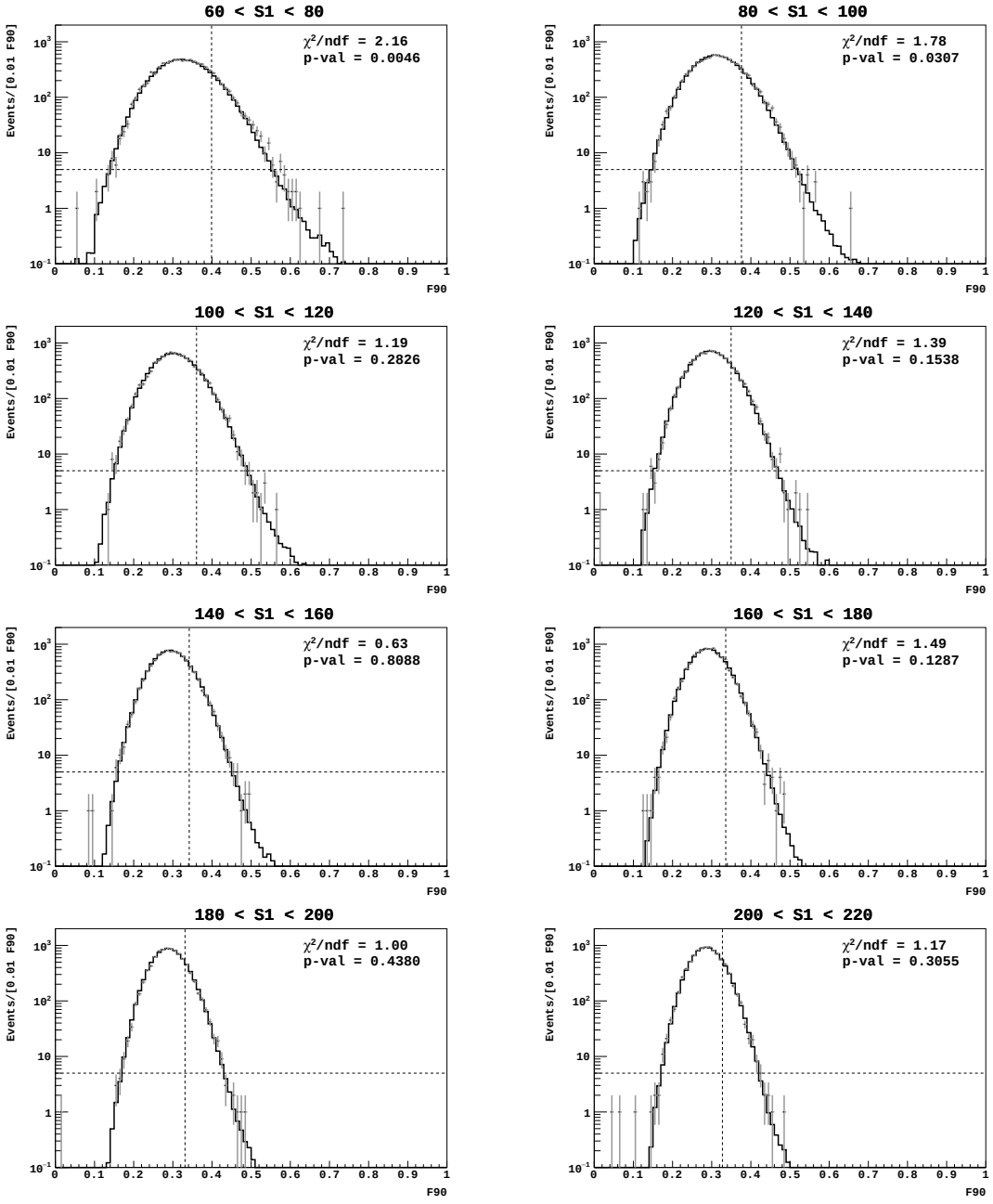

Figure 5.16: F90 profiles of single-scatter—*i.e.*, two-pulse—events with 40 µs fiducialization and passing the S1 prompt maximum fraction cut, from 70d UAr data (gray) and from the model (black). Best fit activities from the energy spectrum fitting were used to normalize among the various detector backgrounds. The model was additionally scaled by a factor of 1.07 so that its event rate for $60 < \mathrm{S1} < 460$ PE matched that observed in the 70d UAr data. χ^2 was computed over bins with $\geq$5 model entries above the (mean+rms) of the model profile (indicated by the dashed lines).

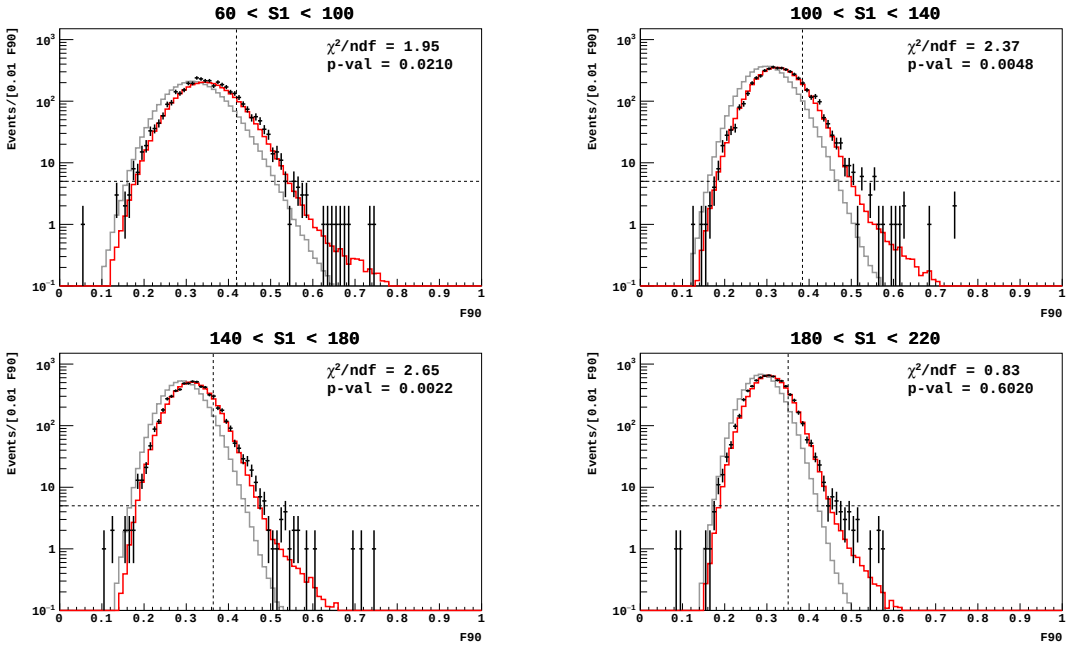

Figure 5.17: F90 profiles of three-pulse events with drift time >10 µs, from 70d UAr data (black), and from the model (red). Best fit activities from the energy spectrum fitting were used to normalize among the various detector backgrounds; the model was additionally scaled by a factor of 1.07. A normalized F90 profile for two-pulse events in the corresponding S1 ranges from the model is also shown (gray) for comparison.

higher F90 than single-scatters with the same S1, as their component scatters would each have the higher F90 observed in single-scatters with lower S1.

F90 profiles of three-pulse events with drift time >10 µs (where drift time was defined as the time separation between the first and second event pulses), from 70d UAr data and from the model, are shown in Fig. 5.17. As motivated in the previous section, the model has been scaled up by a factor of 1.07. These events were expected to be dominated by double Compton scatters from γ-rays emitted by radioactive decay in our detector components. We see that although the χ^2/p-values were not great, the model successfully recreated the systematically higher F90 of such multiple-scatter events by referencing the F90 of single-scatter ^{39}Ar events.

Chapter 6

The blind analysis

Although essentially all observed events were expected to be from background, a blind analysis was done, in which data with NR-like F90 were hidden from analyzers during background studies. This is because developing the background models and cuts while inspecting all available events could have biased the analysis to removing all signal-like events—*i.e.*, the analysis would actually have had no acceptance for WIMP scatters.

6.1 Implementation of blinding

At the start of the 530d UAr analysis, a blinding region defined in F90 *vs.* S1 was applied on the data as it were being acquired, hiding all events falling in this phase-space from analyzers, regardless of their other parameters (*e.g.*, pulse multiplicity, drift time, *etc.*). As shown in Fig. 6.1, this blinding region was defined to be significantly larger than any plausible final WIMP search region; the blinding region was defined as:

$$\texttt{S1 > 20 \&\& S1 < 600 \&\& F90 >} \sum_{i=0}^{6} p_i \texttt{S1}^i \texttt{ \&\& F90 < 1} \tag{6.1}$$

Table 6.1: Coefficients for the polynomial describing the F90 lower bound of the blinding region.

p_0	p_1	p_2	p_3
0.915	-7.56×10^{-2}	5.22×10^{-5}	-2.01×10^{-7}
p_4	p_5	p_6	
4.31×10^{-10}	-4.79×10^{-13}	2.14×10^{-16}	

where the lower bound in F90 was a polynomial with coefficients shown in Tab. 6.1. In particular, this bound was designed to skim the high F90 side of the ER band, allowing $\sim$3 event/yr/[5 PE bin] of ER background leakage, so that there would be sufficient statistics for eventual model testing; by necessity, this was designed with a less developed version of the ER background model than that described in Ch 5.

If an event's S1 and F90 was in the blinding region, all its information except the event ID, its livetime, and timestamp information were initialized to default values. Event livetime was left open to analyzers to facilitate accurate accumulation of total livetime, which is required to normalize the background models; event timestamps were necessary for matching against data acquired in the veto. All non-530d UAr data—*i.e.*, the 70d UAr, AAr, and all source calibration data—were left open to analyzers.

The analysis plan was to develop the various background models without inspection of the 530d UAr data in the blinding region, and when the models were ready, to reveal the blinded data in a number of steps, testing model predictions against these revealed data along the way.

In anticipation of low event counts in the blinding region as more regions for model testing were revealed, events were also picked at random (*i.e.*, regardless of their S1 or F90) with a probability of 2×10^{-5} (which works out to about 1 event per 12 h of data acquisition) to be blinded. The aim of this random blinding was to prevent accidental counting of WIMP signals as both the blinding region and the number of blinded events got progressively smaller.

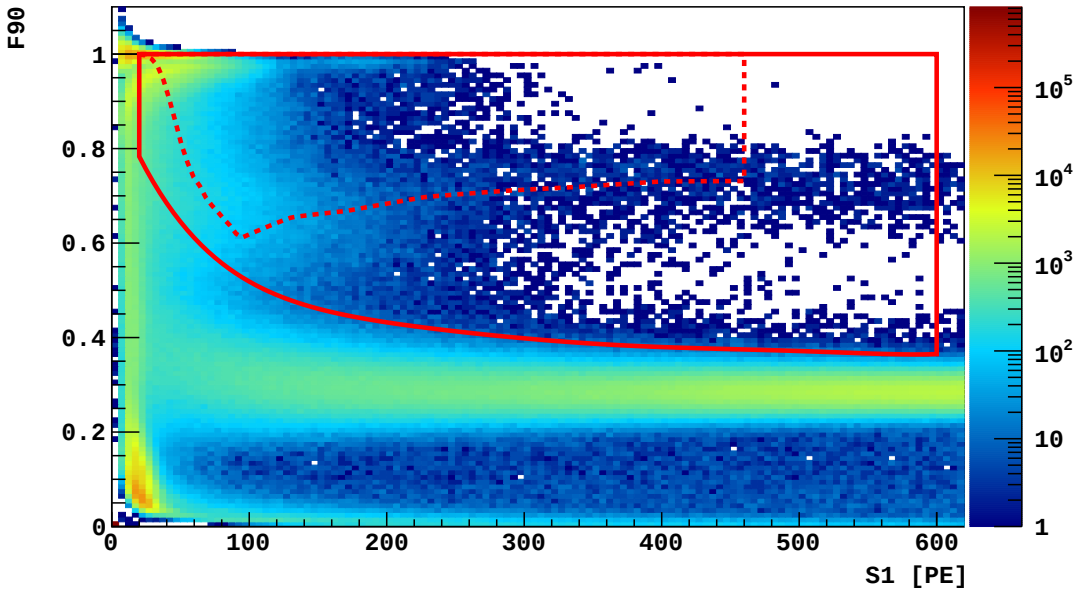

Figure 6.1: 70d UAr data with basic quality cuts, overlaid with the blinding box in solid red; $\sim 3 \times 10^5$ 70d UAr events fell in the blinding box. The 70d UAr WIMP search region is shown in dashed red.

6.2 Sequential unmasking of data for testing

Three tranches of data were revealed for testing and development of the background models before the final opening of the full data set: 1) All events with a prompt veto signal; 2) All non-single-scatter events; and 3) Events in two F90 *vs.* S1 regions within that described in Eqn. 6.1.

6.2.1 Events with a veto prompt signal

Events with a veto prompt signal >1 PE (veto prompt tagged, or "VPT" events) were revealed for the study of the neutron and γ-ray backgrounds. Contamination of these VPT events by WIMP scatters was not anticipated because: 1) A WIMP scatter in both the LSV and the TPC was extremely unlikely; and 2) The accidental coincidence rate of the veto prompt signal had been measured to be low (Sec. 8.5.4).

The VPT data were expected to provide an accurate count of the neutron background actually seen in the detector as the veto prompt signal had been measured using ^{241}Am^{13}C calibration data to tag neutron events with a high efficiency of >0.99 [43, Tab. II]. As mentioned in Sec. 2.1, many γ-rays from our background sources scatter in both the TPC and the LSV, and so the VPT data provided a source of ER events as well. To distinguish between the neutron and γ-ray backgrounds, we looked at the delayed (*i.e.*, >200 ns after the trigger) veto signal of these VPT events, counting as neutrons events with $60 < \mathrm{S1} < 460$ PE satisfying:

```
(clus_charge > 800 && clus_mult >= 100) ||
(200 < clus_charge < 800 && clus_mult > 0.1×clus_charge + 20) ||
(100 < clus_charge < 200 && clus_mult > 0.125×clus_charge + 15)
```
(6.2)

where `clus` refers to the clustered veto signal (photoelectron signals in the LSV are clustered by their time separation), `charge` refers to the magnitude of the cluster signal in PE, and `mult` refers to the PMT multiplicity of the cluster, *i.e.*, how many PMTs contributed to that particular cluster signal. A large delayed cluster signal of >100 PE, equivalent to ∼200 keV deposited in the LSV, was expected from most neutron captures. Since afterpulsing in the LSV PMTs was quite prevalent, the multiplicity conditions were necessary to distinguish between a true delayed signal from neutron capture, and afterpulsing induced by the prompt veto signal of these VPT events (Fig. 6.2). The neutron tagging efficiency for these conditions was estimated to be ∼0.79, with most of the loss coming from the high charge threshold and from avoiding the 200 ns window after the trigger [43].

Single-scatter VPT events after 40 µs fiducialization and passing the S1pmf cut in the 530d UAr data, and the neutrons tagged by the selection conditions described above, are shown in Fig. 6.3.

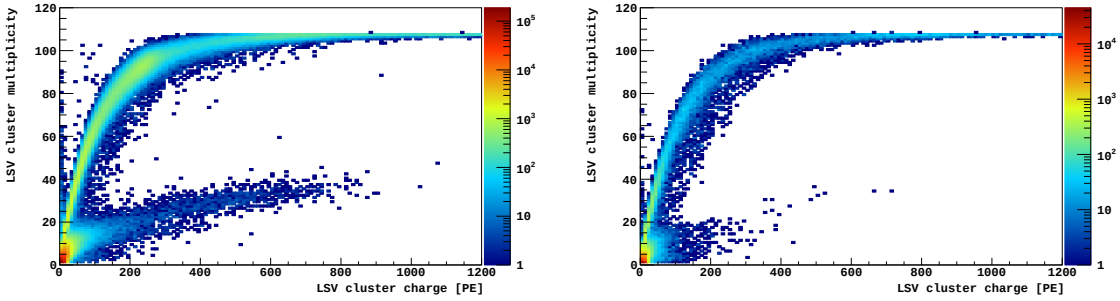

Figure 6.2: Charge *vs.* multiplicity of LSV cluster signals, from ^{241}Am^{13}C neutron source calibration events (left) with and (right) without a veto prompt signal. The band of low multiplicity (<40) clusters, correlated with a veto prompt signal, were afterpulses in the LSV PMTs triggered by the prompt signal.

Neutron counting

For the purposes of neutron counting, we further differentiated between radiogenic (*i.e.*, from radioactive decay in detector materials) and cosmogenic neutrons (*i.e.*, from spallation by passing muons), as their predicted rates came from different models. To do so, we looked for large signals in the LSV and/or WCV consistent with Cherenkov radiation from passing muons or the charged relativistic particles in the accompanying showers (Sec. 4.3.4). Three events falling in the 530d UAr WIMP search region (Ch. 7) were found to satisfy this requirement. Upon inspection of their waveforms, one of these events was found to have a large LSV signal only (<400 PE in the WCV), and contain three neutron capture signals (*i.e.*, three clusters that satisfied condition 6.2), consistent with a fission event. Thus, two cosmogenic neutrons were observed in the 530d UAr data; the remaining neutron in the 530d UAr WIMP box did not have a large veto signal, and was categorized as a radiogenic neutron. These events are shown in Fig. 6.3.

Testing the electron recoil F90 model

Before the VPT data were revealed, the test region shown in Fig. 6.3(middle) was defined. It spanned from 60 PE to 200 PE in S1, and its lower and upper F90 bounds

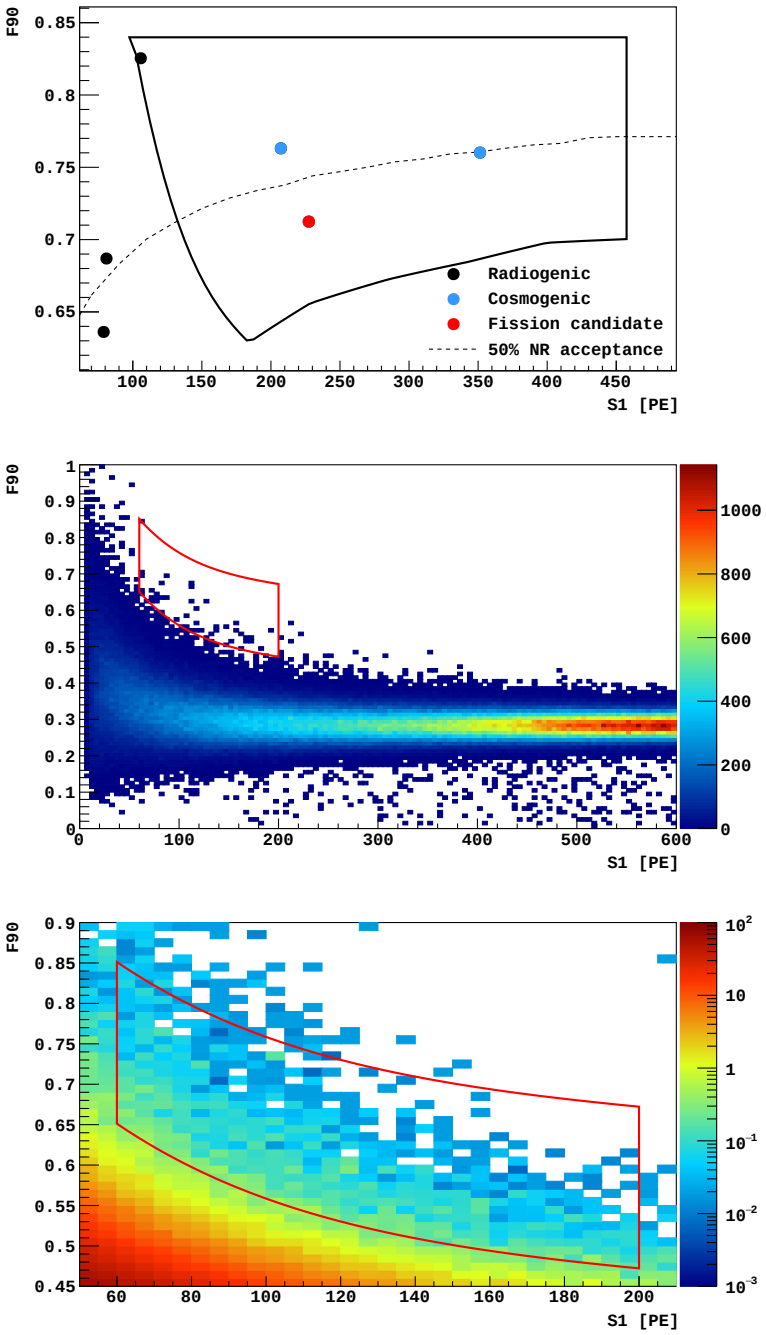

Figure 6.3: **Top:** Neutron candidates near the WIMP search region; the 530d UAr WIMP search region (Ch. 7) is shown in black. **Middle:** Single-scatter veto prompt tagged events after 40 µs fiducialization and passing the S1pmf cut in the 530d UAr data, without neutron candidates. The test region for model testing is overlaid in red. **Bottom:** Single-scatter veto prompt tagged events after 40 µs fiducialization and passing the S1pmf cut from the electron recoil background model.

were the blinding function (the polynomial in Eqn. 6.1) translated vertically upward by 0.04 and 0.24 respectively.

As can be seen in Fig. 6.3, the VPT data provided plenty of ER event statistics for background model testing. Importantly, because the probability of a WIMP event having a veto prompt signal was low, the VPT events were a safe way to study the high F90 tails of the ER F90 *vs.* S1 distribution.

In the test region, we observed 48 VPT events in the 530d UAr data, compared to the model's prediction of 41 events. Since the predicted count agreed with the observed count to within two standard deviations, we concluded that the ER F90 model was in good shape. Note that the model's prediction was based on a Monte Carlo containing $\sim$3000 d worth of simulated UAr background, so the statistical error on the prediction is small.

6.2.2 Non-single-scatter events

The second batch of 530d UAr data to be revealed was non-single-scatter events. Contamination of these events by WIMP scatters was not anticipated because the probability of a WIMP scattering more than once in the active argon, or not producing an ionization signal, was very low. Single-pulse events in particular were used for further testing and development of the Cherenkov model (by Xiang), and for estimating the rate of single-pulse NR-like events (by Monte).

6.2.3 Events with high F90

The final set of 530d UAr data to be revealed for background model testing purposes was a subset of high F90 events without a veto prompt signal. The main aim for revealing these data was to test the ER background model. The F90 *vs.* S1 region that was still hidden after this step is shown in Fig. 6.4; the following categories of events were revealed:

1. Events with $0.84 < \text{F90} < 1$ were revealed. Inspection of the NR F90 profile from ^{241}AmBe source calibration data showed that NR acceptance in this region was low ($\lesssim$1%) [60]; thus, the upper F90 bound for the WIMP search region was lowered to reduce the risk of getting a single-pulse Cherenkov S1 + stray S2 background event. The low NR acceptance of the revealed region also means that the chances of accidentally revealing a WIMP event here were small.

2. Events with F90 below a ∼99% NR acceptance contour (drawn with an earlier NR F90 model) were revealed. Again, the low NR acceptance of the revealed region means that the chances of accidentally revealing a WIMP event here were small.

3. Events with S1 <150 PE and F90 below a ∼90% NR acceptance contour were revealed. The NR acceptance here is not small; however, given the null result observed in the 70d UAr analysis, we estimated an upper bound (90% C.L.) of $< (0.11 \times 2.3 \times 530/70 = 2)$ WIMP events in this revealed region, which was less than the statistical error on the expected number of ER background events (see below).

Before these events were revealed, three test regions were defined for further testing of the ER background model; these regions, A, B, and X, are shown in Fig. 6.4(middle). With 40 µs drift time fiducialization, the S1pmf cut, and the veto prompt cut applied, the model predicted events in these regions to be dominated by single-scatters in the active argon accompanied by Cherenkov radiation in the Teflon. The following cuts were applied on the 530d UAr data for comparison: event quality and topology cuts (Sec. 4.1 and 4.2), drift time fiducialization (cut 4.4.1), the S1pmf cut (cut 4.6.2), the uncorrected S2 and successful xy reconstruction cut (cut 4.4.2), and the LSV prompt signal cut (cut 4.3.1).

530d UAr events in categories 1 and 2 were revealed first, which let us test the model in regions A and X. As summarized in Tab. 6.2, 24 (0) events in the 530d UAr data were observed in region A (X), corresponding with 13.3 (3.0) events predicted by the ER background model. The significant discrepancy ($\sim 3\,\sigma$) between the data and the model in region A was a cause for concern, and motivated the unmasking of events in category 3, which contains region B, to supplement the available data statistics. 9 events were observed in the data in region B, *vs.* 8.7 events predicted by the model.

We chose to interpret the discrepancy between the data and the model in the combined (A+B) regions as a measure of the systematic error of the ER background model; region X was not included in this calculus because of its poor statistics. Consequently, we multiplied the model's predictions by a factor of (24+9)/(13.3+8.7) = 1.5 to correct for the measured systematic.

Test region events with low S2

Scrutiny of the observed events in region A revealed that a significant number of these (10) had $\mathrm{S2_{uncorr}}$ signals smaller than 200 PE, which is a high rate for such occurrences that had not been observed elsewhere in the data (see acceptance of the minimum $\mathrm{S2_{uncorr}}$ cut in Tab. 8.1). To see what mix of scintillation and Cherenkov components such events were compatible with, a quick calculation was done:

$$\mathrm{F90} = \frac{\mathrm{S1_{Cherenkov}} + \mathrm{F90_{scintillation}} \times \mathrm{S1_{scintillation}}}{\mathrm{S1_{Cherenkov}} + \mathrm{S1_{scintillation}}} \tag{6.3}$$

Substituting in average F90 and S1 values for region A—F90 = 0.55 and ($\mathrm{S1_{Cherenkov}}$ + $\mathrm{S1_{scintillation}}$) = 150 PE, we got

$$\begin{aligned} 0.55 &= \frac{150 - \mathrm{S1_{scintillation}} + \mathrm{F90_{scintillation}} \times \mathrm{S1_{scintillation}}}{150} \\ \Rightarrow \mathrm{S1_{scintillation}} &= \frac{0.55 \times 150 - 150}{0.3 - 1} = 96.4\,\mathrm{PE} \end{aligned} \tag{6.4}$$

where $\mathrm{F90_{scintillation}} = 0.3$ was used. Essentially, this meant that the scintillation component would not have been tiny if the event had a scintillation+Cherenkov topology, and should have had a reasonably sized $\mathrm{S2_{uncorr}}$ signal. Thus, we concluded that these events did not originate from the γ-rays in the ER background model, and did not include them in the data count presented in Tab. 6.2 for comparisons against the model.

Similar to region A, a significant number of observed events (9) in region B also had anomalously small $\mathrm{S2_{uncorr}}$, and were thus not counted for the comparison against the ER background model.

Estimating the radial cut's rejection on test region events

Because calibration sources with known locations within the TPC were not available, the resolution of the reconstructed xy-positions of events relative to their absolute position could not be determined. This meant there was no good way to estimate the rejection of the radial cut (cut 4.4.3) using our simulated ER events. As such, the 530d UAr data in the test regions A and B were also used to estimate the rejection of the radial fiducialization (Sec. 4.4.3) on ER background. In particular, we found that 30 events passed all 530d UAr analysis cuts except the veto delayed cut and radial fiducialization (cuts 4.1.1 through 4.3.1, cuts 4.3.3 through 4.4.2, and cuts 4.5.1 through 4.6.3), of which 17 were subsequently removed by the radial fiducialization. From this, we inferred a rejection factor of $30/13 = (2.3 \pm 0.6)$. Accordingly, the model's output was multiplied by a factor of $1.5/2.3 = 0.65$ to get the predicted

Table 6.2: Event counts observed in the data, and predicted by the electron recoil background model, in the test regions A, B, and X (shown in Fig. 6.4(middle)). Major cuts applied were the 40 µs drift time fiducialization, veto prompt cut, and S1 prompt maximum fraction cut (see text for details).

	A	B	X
Data	24	9	0
Model	13.3	8.7	3.0

ER background (where the factor of 1.5 was the systematic error on the model's predictions, derived above).

6.3 Background predictions

To be "background-free", we targeted <0.1 total background events in the final WIMP search region, meaning there would be a >0.9 Poisson probability of observing no background events in the WIMP box for our exposure. In the following sections we document the breakdown of the background budget among the neutron, surface, and electron recoil backgrounds. We note that part of this accounting is necessarily iterative—the ER background budget affects the size of the WIMP search region, which of course feeds back into the predicted neutron and surface background rates.

6.3.1 Radiogenic neutron background

The prompt and delayed veto cuts' (Sec. 4.3.1 and Sec. 4.3.2) high efficiencies for tagging neutron events has been measured using ^{241}Am^{13}C neutron source calibration data (by Qian), which were in agreement with Monte Carlo simulations [25, Ch. 10]. Given the combined neutron vetoing efficiency of 0.9964 [43, Tab. II], and the observation of one radiogenic neutron event in the 530d UAr WIMP search region, we projected a radiogenic neutron background of (0.004 ± 0.004), with Poisson fluctuations on the single counted event being the dominant uncertainty.

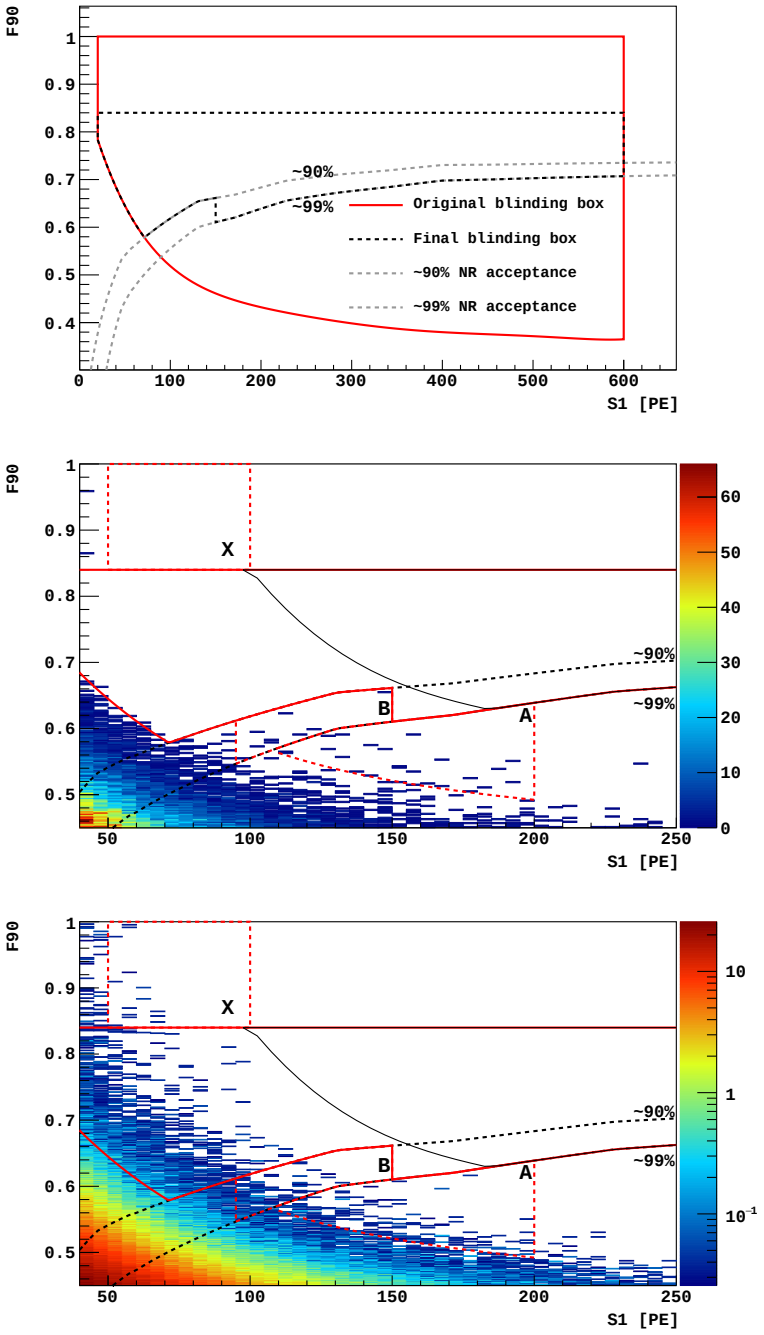

Figure 6.4: **Top:** The original blinding region, implemented at the start of the 530d UAr analysis, and the final blinding region, before full opening of the 530d UAr data. Also shown are the approximate 90% and 99% NR acceptance contours that were used to design the unmasked regions. **Middle:** Events in the 530d UAr data after 40 µs fiducialization, with no veto prompt signal, and passing the S1pmf cut; events in the final blinding region (solid red) are still hidden. Overlaid (in dashed red) are the test regions A and B. Also shown (in solid black) is the final 530d UAr WIMP search region. **Bottom:** Corresponding events as predicted by the ER background model.

We note that the predicted rate of radiogenic neutron background, estimated using the radioisotope activities in Tab. 3.3 and the (α, n) neutron yield calculator described in [25, Ch. 4], was several times that actually observed in the VPT data. The working explanation for this discrepancy was that the (α, n) neutron yield is highly dependent on the local distribution of various target and source elements, which are not uniform in ceramics, such as the one present in the PMTs. Thus, we used the neutron count in the 530d UAr data as the definitive measurement of the radiogenic background rate.

6.3.2 Cosmogenic neutron background

The cosmogenic neutron background rate was estimated using a FLUKA-based Monte Carlo simulation [61] containing 33.4 yr worth of cosmogenic events (by Singh). This simulation predicted that $\sim$2 cosmogenic events per year would result in a neutron scatter in the TPC passing the modeled TPC cuts. In the simulation, all such events resulted in a large signal in the vetos that failed the modeled veto cuts (in particular, cut 4.3.4). The prediction of 2 cosmogenic neutron events per year, tagged by their TPC and veto signals, agreed with our observed count of 3 such events in the 530d UAr data (2 of which were in the WIMP search energy range, Fig. 6.3).

The efficiency of the veto and TPC cuts at tagging cosmogenic neutron events was estimated using a separate FLUKA simulation, this one containing 48.7 yr worth of cosmogenic events, and in which events with a long (>2 m) and high-energy (>4 GeV) muon track in the WCV were not propagated further (as the Cherenkov radiation from these events would produce a large veto signal). In this simulation, 1388 events resulted in any particle reaching the TPC, of which 7 involved a neutron. Despite the track length and muon energy requirements, none of these 7 events passed the modeled veto cuts; their energy deposits within the TPC were also outside the 530d UAr WIMP search range. Thus, we set an upper limit (90% C.L.) on the probability of the TPC

and veto cuts missing cosmogenic events that reach the TPC at $<2.3/1388 = <0.0017$; we then normalized this using the 7 simulated events involving a neutron:

$$\frac{7}{48.7\,\mathrm{yr}} \times \frac{532\,\mathrm{d}}{365\,\mathrm{d/yr}} \times \frac{<2.3}{1388} = <3.5 \times 10^{-4} \tag{6.5}$$

arriving at a predicted cosmogenic neutron background of $<3.5 \times 10^{-4}$.

6.3.3 Surface backgrounds

As mentioned in Sec. 3.1.2, surface backgrounds in DS-50 were the result of α-decay at or near detector surfaces touching the LAr. Because of their short range in the LAr, α-particles emitted from the cathode window and grid were easily removed by the drift time fiducialization, leaving those emitted from the Teflon TPC wall as problematic backgrounds. In DS-50, we observed both single- and two-pulse (S1-only and S1+S2) events with NR-like F90 that had no veto signal. These were consistent with surface background events, with the lack of an S2 signal in some of them perhaps due to the loss of ionization electrons drifting close to the TPC wall.

From the 70d UAr data, the rate of S1-only events was estimated to be $\sim 12\,\mathrm{d}^{-1}$. Such events posed a problem if coupled with a stray S2-only signal. To mitigate these occurrences, cuts were implemented to check that: 1) The S2 pulse in an event was an appropriate size relative to the S1 signal (Sec. 4.2.5 and Sec. 4.6.1); 2) The S2 pulse was not actually an unresolved S1+S2 pulse, which tends to happen to scatters with short drift times (Sec. 4.5.3); and 3) The event's z-position as indicated by its drift time agreed with that indicated by the S1 pulse's top-bottom asymmetry (Sec. 4.5.2). The efficiencies of these cuts at removing S1-only + stray S2-only events was estimated using a simulation that modeled two-pulse events by combining S1-only and S2-only waveforms extracted from the UAr data with different drift time separations. Combined with the measured rate of S1-only events, we predicted a

Table 6.3: Predicted backgrounds in the 530d UAr exposure, surviving all WIMP search analysis cuts.

Background	Events surviving analysis cuts
Radiogenic neutrons	<0.005
Cosmogenic neutrons	$<3.5 \times 10^{-4}$
Surface backgrounds	0.00150 ± 0.00014
Electron recoils	0.08 ± 0.04
Total	0.09 ± 0.04

background of (0.00092 ± 0.00004) for the 530d UAr analysis from this source. All studies of such events were done by Monte.

Two-pulse surface background events observed in DS-50 typically had very large S1 and S2 signals, consistent with the energetic decay α's responsible (*e.g.*, [43, Fig. 1]). We estimated the rate of two-pulse surface background events having S1 and S2 within the WIMP search range to be <0.07 for the 530d UAr exposure; these consist of heavily degraded α-particles, with S1 slightly boosted by scintillation of the TPB excited by the passing α-particle. To remove such events, a cut was designed to look for the long-lived scintillation of TPB between the S1 and S2 pulses (Sec. 4.5.1). We predicted a remaining background of (0.0006 ± 0.0001) after the application of this cut [42].

6.3.4 Electron recoil background

The predicted neutron and surface backgrounds are summarized in Tab. 6.3. With these predictions in hand, we alloted 0.08 of the targeted 0.1 background budget to electron recoils. How this level of ER background was obtained will be discussed in Ch. 7.

Chapter 7

Finalizing the WIMP search region

As described in Ch. 5, the electron recoil background model consisted entirely of simulated events (with data-driven F90), normalized using the estimated radioisotope activities in Tab. 3.3. We note that this way of modeling the ER background was new to the 530d UAr analysis—in the AAr and 70d UAr analyses, an analytic model for ER F90 was fitted to the data, from which the <0.1 event of targeted background was extrapolated.

The use of a simulation driven background model had implications on both the minimum statistics required for the background simulation, and the statistical fluctuations associated with any F90 cut—*i.e.*, the WIMP search region/box.

7.1 Required simulation statistics

7.1.1 A note on previous analysis procedures

In the 70d UAr and AAr analyses, the shape of the WIMP box at low S1—*i.e.*, where it did not trace the approximate 90% NR acceptance contour—was set to be the 0.01 leakage event per [5 PE bin] threshold, spanning ∼10 S1 bins (Fig. 7.1). Attempting to set the same F90 contour using only simulated events would require

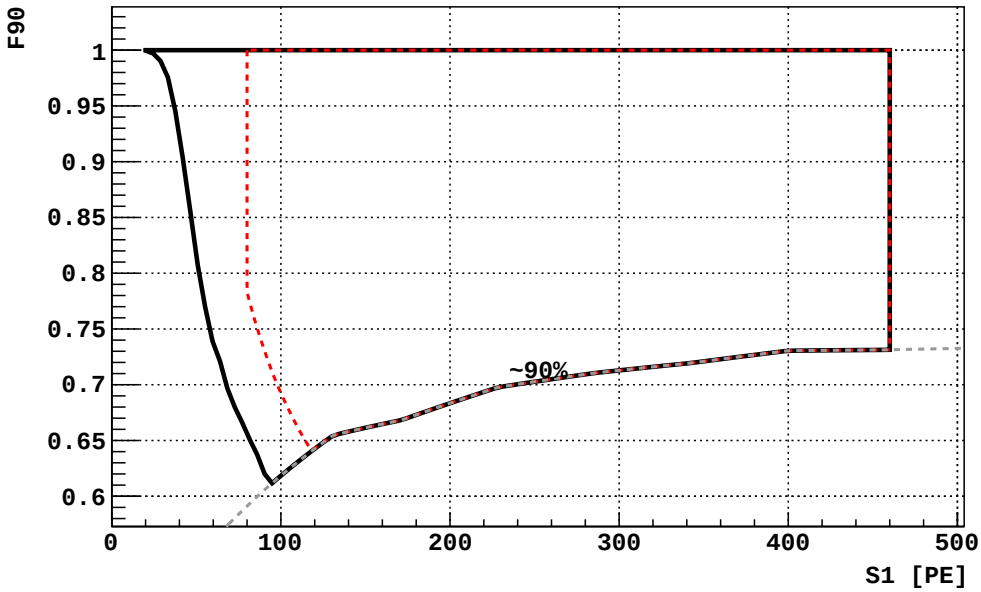

Figure 7.1: WIMP search regions for the 70d UAr (black) and AAr (red) analyses. The ∼90% nuclear recoil acceptance contour driving the lower F90 bounds of both boxes at high S1 is also shown (gray.)

at least $100 \times 500\,\mathrm{d} = 50000\,\mathrm{d}$ worth of simulation statistics. This was untenable given initial estimates that placed the associated time and storage requirements at >500000 CPU-days/>100 TB.

7.1.2 Implications of lower simulation statistics

At least $12.5 \times 500\,\mathrm{d} = 6250\,\mathrm{d}$ worth of simulation statistics are required to set a WIMP search region containing 0.08 event of background; at this bare minimum, one simulated event would be responsible for the total predicted background. Using the construction by Feldman and Cousins [62], we see that an observed event count of 1 is consistent (68% C.L.) with a mean background of up to 2.75 (Tab. 7.1)—*i.e.*, the predicted background could be as high as $2.75 \times 0.08 = 0.22$ with this construction.

The marginal benefit of increased simulation statistics on the uncertainty of the background prediction is shown in Tab. 7.1. Given the low targeted background, we decided that a prediction correct to within a factor of two was acceptable; thus,

Table 7.1: Implications of available simulation statistics (relative to data) on the precision of a background prediction of 0.08 event. 68% C.L. intervals as constructed by Feldman and Cousins ([62, Tab. II]) are presented. We see that for the upper bound on the background prediction to be within a factor of 2 of the target (*i.e.*, <0.16), it has to be driven by at ≥3 simulated events (*i.e.*, the simulations have to contain ≥37.5 times the data statistics).

[Simulation statistics] : [Data statistics] ratio	12.5	25	37.5	50	62.5	87.5	150	300
No. of simulated evts equivalent to 0.08 predicted bkg. evts	1	2	3	4	5	7	10	20
68% C.L. interval on predicted bkg.	0.030 0.22	0.030 0.17	0.030 0.14	0.047 0.14	0.044 0.12	0.049 0.12	0.054 0.11	0.063 0.10

approximately $3 \times 12.5 \times 500\,\mathrm{d} = 18750\,\mathrm{d}$ worth of simulations were required. ∼30000 d of events were generated for our final simulated event set.

7.2 WIMP box setting procedure

Having a WIMP search region driven by only a few simulated events allowed for a large variety of plausible box shapes (as many S1 bins ended up containing no simulated background). For the 530d UAr analysis, we used a two step procedure for generating the WIMP box: 1) The F90 contour at low S1 was shaped where simulation statistics were greater; and 2) The shaped contour was translated to higher F90 to obtain the desired total background in the box. These steps are described in more detail in the following sections. We note that the choice of procedure does not impact the validity of the final analysis results, as a rigorous background estimate and WIMP acceptance could be obtained for any WIMP box.

7.2.1 Shaping the WIMP search region at low S1

A shape for the lower F90 bound at low S1 was obtained with the following steps:

1. Since the ER background in the WIMP box was expected to be driven by events with a significant Teflon Cherenkov component, it was appropriate to shape the F90 contour in a region where Teflon Cherenkov background was also dominant—*i.e.*, at high F90. We chose to first obtain a rough contour by finding the F90 threshold that resulted in 0.07 leakage events per [5 PE bin] of S1. The choice of 0.07 leakage events per S1 bin was a compromise between having the contour be shaped by a background representative of that at the box's final position (at high F90), and having sufficient simulation statistics (at low F90). Ultimately, the contour's shape was set in a region where ∼90% of the predicted background had a Teflon Cherenkov component. Notably, however, the resultant contour was quite jagged because of low simulated event statistics.

2. Since the contour ought to be both smooth and monotonically decreasing with increasing S1, the jaggedness from the previous step was smoothed out by fitting it with a cubic function, the results of which are presented below:

$$\text{F90} = 1.95 - 0.0200 \times \text{S1} + 9.92 \times 10^{-5} \times \text{S1}^2 - 1.72 \times 10^{-7} \times \text{S1}^3 \qquad (7.1)$$

Both the jagged and fitted contours are presented in Fig. 7.2.

7.2.2 Positioning the contour

The smoothed contour was translated vertically until a WIMP box containing the desired amount of background (here <0.08 event) was constructed. The lower F90 bound of the WIMP box was defined to be either the smoothed contour, or the 99% NR acceptance line, whichever was higher in F90. In particular, the choice of using the 99% NR acceptance contour was a departure from previous analyses, which used the 90% acceptance line instead. This change—which increases the WIMP acceptance—was made because the modeling indicated no great risk of background by doing so.

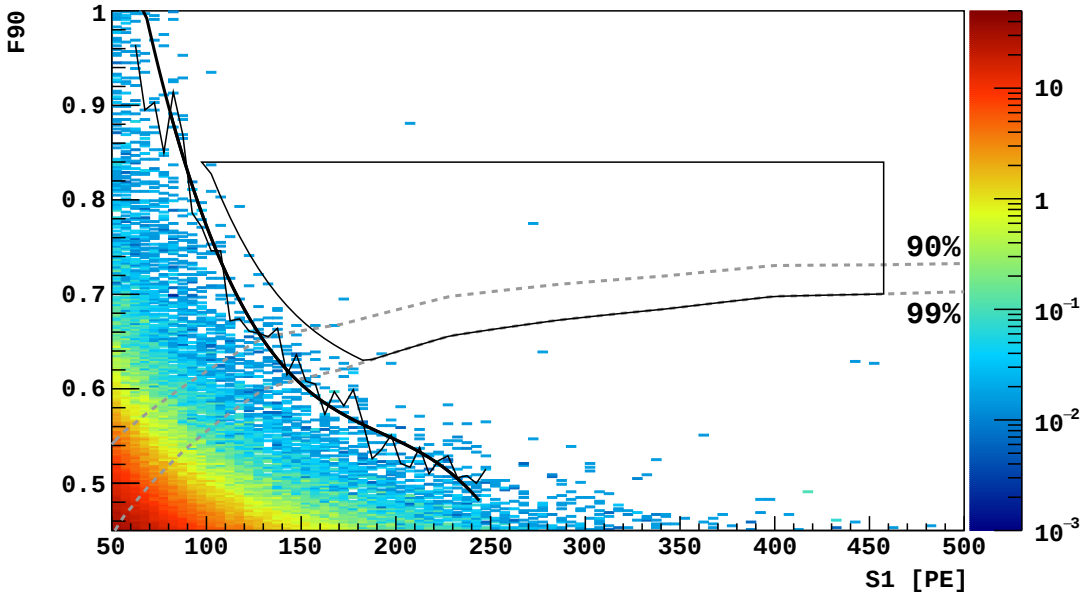

Figure 7.2: Modeled 530d UAr ER background, with 40 µs fiducialization, passing the S1 prompt maximum fraction cut, and passing the veto prompt cut; acceptance loss due to the delayed veto cut has also been accounted for using a scale factor of 0.84 (Sec. 4.3.2). The jagged 0.07 leakage event per [5 PE bin] contour, fit of a cubic function to it, and 530d UAr WIMP search region containing 0.08 event of ER background, are overlaid. The 90% and 99% nuclear recoil acceptance contours are also shown (dashed gray).

We note as well that the upper F90 bound of the WIMP box was lowered to F90 = 0.84 from F90 = 1 in previous analyses. From studies of the NR F90 distribution seen in ^{241}AmBe source calibration data [60], the consequent loss of acceptance from this change was estimated to be <1%. This was done to guard against background due to a Cherenkov-only S1 + stray S2 coincidence event.

The upper S1 bound of the WIMP search region was left at 460 PE, the same bound used for the 70d UAr and AAr analyses.

The resultant WIMP box, driven by 7 simulated events, and containing 0.08 events of predicted background for the 530d UAr exposure, is shown in Fig. 7.2.

7.3 Discussion

7.3.1 Contour shapes

As mentioned in Sec. 7.2, we could have plausibly chosen other ways of setting the shape of the WIMP search region at low S1. This is reflected in Fig. 7.2: at low S1, the WIMP box is not anchored in every bin by simulated events either immediately above or below it.

To estimate the impact of plausible variations in the WIMP box on WIMP acceptance, the shape of the contour designed in Sec. 7.2.1 was varied by adding a linear term $(Ax+B)$ to the fitted cubic function, before the translation step. These variants are shown in Fig. 7.3 (with $(A, B) = (-0.003, 125)$ for the red curve, and $(0.0005, 125)$ for the blue curve); a variant constructed by translating the original fitted contour horizontally (instead of vertically) is also presented (in green).

Limits on the WIMP-nucleon scattering cross-section set by these box variants are summarized in Tab. 7.2 (see Ch. 9). We see that the various boxes containing <0.08 events of ER background have limits ranging from $1.15 \times 10^{-44}\,\mathrm{cm}^2$ to $1.33 \times 10^{-44}\,\mathrm{cm}^2$.

7.3.2 Impact of low simulation statistics in the WIMP search region

As we noted earlier, our targeted ER background of 0.08 events ended up being represented by 7 simulated events; this meant that the predicted ER background was (0.08 ± 0.04), with the uncertainty dominated by the low simulation statistics (Tab. 7.1). With a 50% uncertainty on the predicted background, it was perhaps unsurprising that there were many candidate boxes to choose from.

To investigate the relation between simulation statistics and variability of the WIMP search region, we repeated the exercise of exploring WIMP box variations

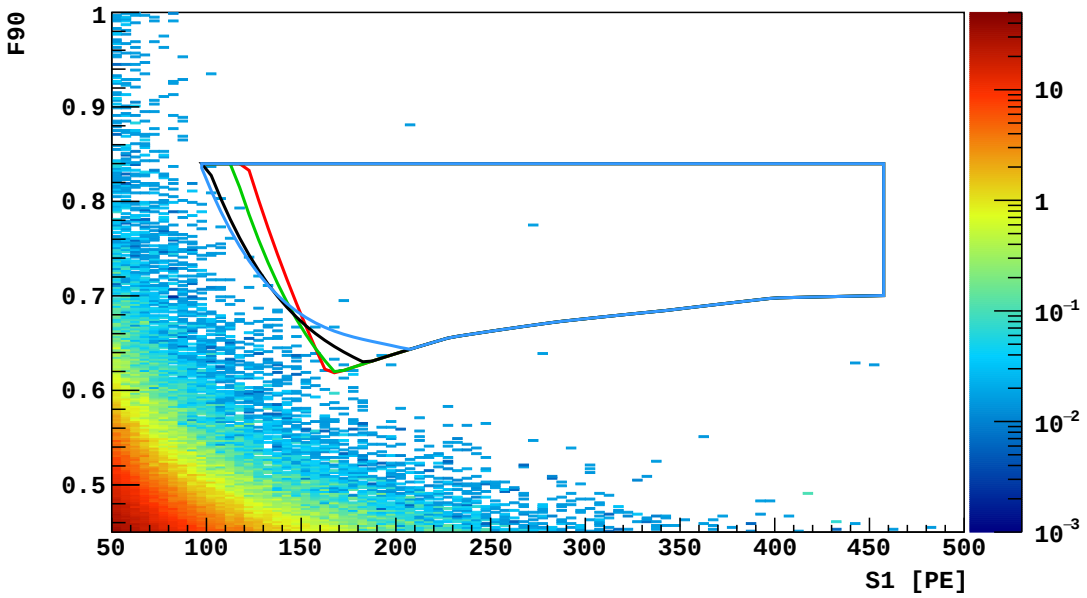

Figure 7.3: Variations of the WIMP box designed in Fig. 7.2 (black), made by adding different linear terms ($Ax + B$) to the fitted cubic function (red and blue), and by translating the original fitted contour horizontally instead of vertically (green).

Table 7.2: WIMP-nucleon scattering cross-section limits (for a WIMP mass of $100\,\mathrm{GeV/c^2}$) set by WIMP boxes admitting various amounts of total electron recoil background, and drawn with various procedures. **Normal:** with the chosen procedure described in Sec. 7.2; **Gentler/Steeper:** with a linear term ($Ax + B$) added to the contour, as described in Sec. 7.3.1; **LR:** with the contour translated horizontally instead of vertically, as described in Sec. 7.3.1.

	Limits from box variants [$\times 10^{-44}$ cm^2]				
Total ER bkg.	Normal	Gentler	Steeper	LR	No. of simulated evts
0.52	0.90	0.96	0.88	0.93	46
0.17	1.06	1.14	1.05	1.14	16
0.13	1.09	1.20	1.08	1.14	12
0.10	1.14	1.28	1.14	1.23	10
0.08	1.15	1.33	1.16	1.23	7
0.07	1.20	1.48	1.19	1.43	6
0.05	1.26	1.54	1.27	1.43	4
0.03	1.30	1.66	1.40	1.66	3

while targeting different amounts of background in the box. Table 7.2 shows that boxes driven by a higher target background—*i.e.*, more simulated events—do indeed span a narrower range of WIMP acceptances, as indicated by their respective limits on the WIMP-nucleon scattering cross-section.

Since the freedom in shaping the WIMP search region was a consequence of statistical fluctuations in the simulated events, we decided to not modify the procedure described in Sec. 7.2 (*e.g.*, by varying the gradient of the contour as described in Sec. 7.3.1). We stress that having limited simulation statistics only impacted the uncertainty on the predicted ER background, which we were willing to accept; there was no consequent uncertainty on WIMP acceptance because the WIMP search region was rigorously defined (Fig. 7.2).

Chapter 8

Cut acceptances

To draw a conclusion about the WIMP-nucleon scattering cross-section based on our results, the WIMP acceptance of the analysis cuts had to be accounted for. Although the impact of all cuts could be interpreted as a loss of acceptance, we chose to account for the impact of some cuts as a reduction in livetime instead, because they enforced no WIMP acceptance whatsoever in certain time windows. In this chapter, we review the impact of the WIMP search analysis cuts on livetime or WIMP acceptance.

We note that some cuts logically had no impact on the livetime or acceptance; for the sake of clarity, however, all analysis cuts are considered in the following sections and this is mentioned explicitly where applicable.

Although we refer to the "residual livetime" after the application of cuts to give an idea of their impact, the livetime accounting after the application of cuts is always cumulative—*i.e.*, we sum from 0 for each suite of cuts, instead of removing livetime from some total as more cuts are applied. Uncertainties on the accumulated livetime will not be quoted since the uncertainty from the trigger board (CAEN V1495) was on the ppm level, and the uncertainties on the estimated WIMP acceptance were expected to be dominant.

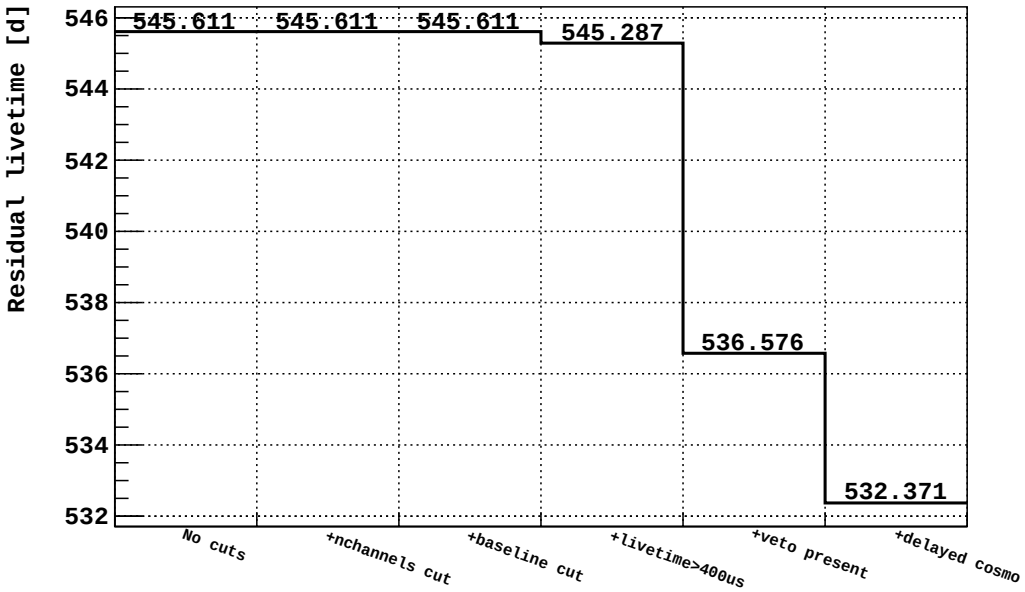

Figure 8.1: Residual livetime after various cuts with relevant impact.

8.1 Trigger type

Impact: None (see below).

Evaluation of residual livetime after cut: `livetime` of events passing and failing this cut was accumulated. The livetime associated with an event was the duration between its trigger, and the closing of the previous inhibit window, during which the detector was live to an intervening trigger.

Events failing this cut were pulser triggers. Such events were still considered for the purposes of livetime accumulation because the pulser trigger was set up to always be superseded by a TPC trigger (*i.e.*, livetime associated with a pulser trigger was live to a potential intervening WIMP event).

The analysis was not set up to look for WIMP events within a pulser-triggered acquisition window (which were not precluded from happening), so `acqui_window` for pulser-triggered events was not included in the accumulated livetime.

Residual livetime after cut: 545.6 d (Fig. 8.1)

8.2 Number of channels

Impact: Loss of livetime.

Evaluation of residual livetime after cut: `livetime` of events passing (*i.e.*, selected by) the cut was accumulated.

A WIMP event could conceivably be observed in the post-trigger acquisition window without being the cause of the trigger; however, the analysis (in particular, cut 8.8) was set up to reject all such events. Thus, for simplicity, we excluded any consideration of the acquisition window from the livetime accumulation from the outset.

Residual livetime after cut: 545.6 d (Fig. 8.1)

8.3 Baseline

Impact: None (see below).

Evaluation of residual livetime after cut: When running with UAr, we observed many bipolar events that triggered the DAQ, but failed this cut (Fig. 8.2). There was no reason to believe that a normal event (including a WIMP event) in the live window prior to such a bipolar signal would have failed to trigger. Thus, the livetime of events failing the cut was accumulated along with that of those passing.

Residual livetime after cut: 545.6 d (Fig. 8.1)

8.4 Livetime

Impact: Loss of livetime.

Evaluation of residual livetime after cut: Since this cut removed events (including potential WIMP events) that triggered within 400 µs of the opening of their

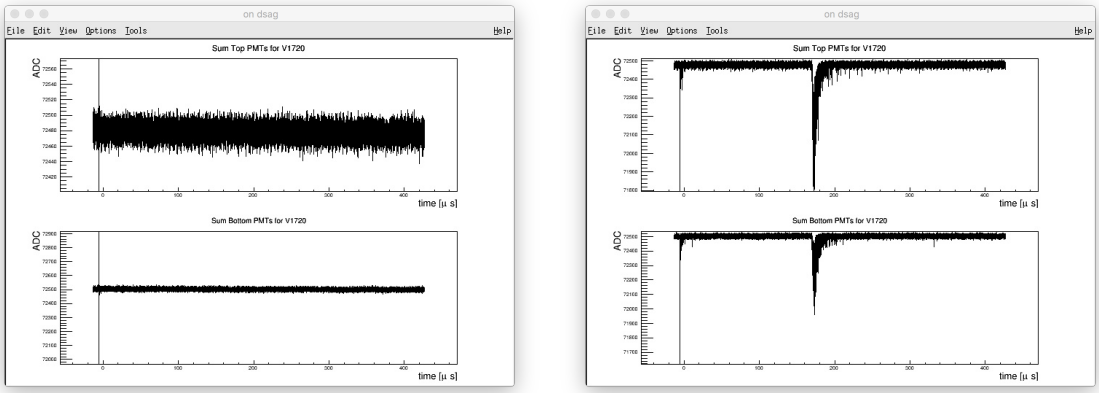

Figure 8.2: Example waveforms, summed over the top and bottom PMT arrays, for a (left) bipolar noise event, and (right) normal scintillation + ionization event.

corresponding live window, (`livetime -` 400 µs) of each event passing this cut, and cut 8.2, was accumulated.

Residual livetime after cut: 545.3 d (Fig. 8.1)

8.5 Veto cuts

8.5.1 Veto present

Impact: Loss of livetime.

Evaluation of residual livetime after cut: (`livetime -` 400μs) of each event passing this cut, cut 8.2, and cut 8.4, was accumulated.

Residual livetime after cut: 536.6 d (Fig. 8.1)

8.5.2 Muon signal

Impact: Loss of acceptance.

Cuts implemented before evaluating acceptance: Cuts 8.1 through 8.4, and cut 8.5.1.

Evaluation of WIMP acceptance: Interpreted all events in regular UAr running vetoed by this cut as an upper bound on loss of acceptance. In the 530d UAr data (SLAD v_3), 556977 events out of 5.42×10^7 failed this cut. This was assumed to be an accidental loss of acceptance.

Evaluation of uncertainty on WIMP acceptance: A statistical uncertainty was derived by interpreting the estimated acceptance loss as a binomial process.

The only assumption made for the estimate was to treat all vetoed events as an acceptance loss—there were no systematics that would have lowered the estimated acceptance.

WIMP acceptance: $0.98972 \pm 0.00001_{\text{stat}}$

8.5.3 Delayed neutrons from cosmogenic activation

Impact: Loss of livetime.

Evaluation of residual livetime after cut: Cuts 8.2, 8.4, and 8.5.1 were applied before this (cuts 8.1 and 8.3 do not impact the livetime, and thus were not applied for the livetime accumulation). Recall that an event's livetime is added to the `muon_dt` counter before this cut is checked. Then an event could fall into several categories (Fig. 8.3):

1. It failed this cut because it failed cut 8.5.2, which reset `muon_dt` to 0. In this case `(livetime -` 400 µs`)` was accumulated, where the 400 µs loss was imposed because the events passed cut 8.4.

2. It failed this cut because it occurred during the 0.6 s cut window. In this case its livetime was not accumulated.

3. It passed this cut, but its `livetime` bridges the 0.6 s cut window. In this case `(livetime - max(`0.6 s `- (muon_dt - livetime),` 400 µs`))` was accumulated. The analysis was not live to events <0.6 s from the start of previous

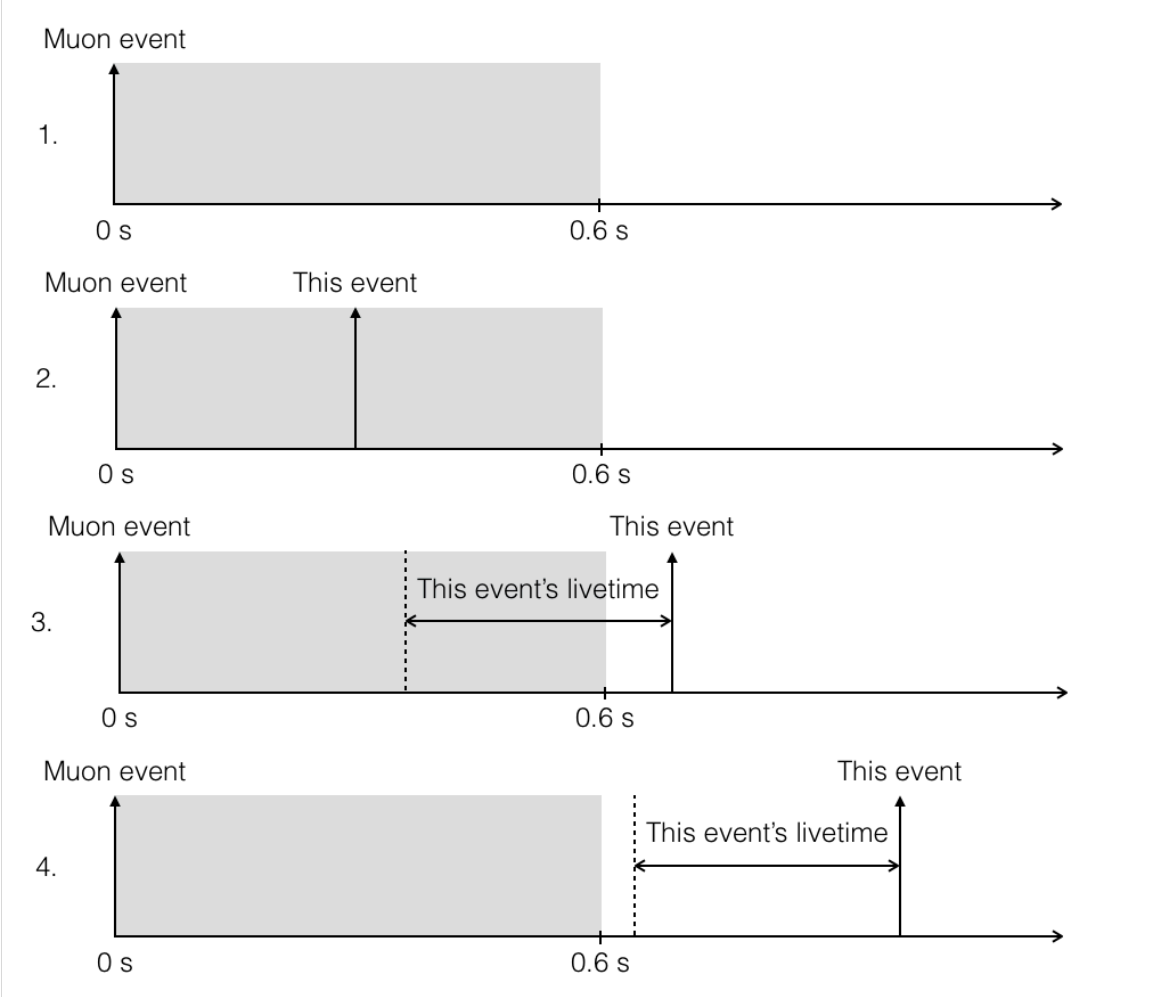

Figure 8.3: When events may occur relative to the 0.6 s window of the cut against delayed neutrons from cosmogenic activation. See text for details on how the total livetime was accumulated in each case.

muon event because of this cut, or to events <400 µs from the end of the previous event because of cut 8.4; the impact on livetime is the union of these two windows.

4. It passed this cut, and it did not matter if its `livetime` was added to `muon_dt`. In this case `(livetime -` 400 µs`)` was accumulated.

Residual livetime after cut: 532.4 d (Fig. 8.1)

8.5.4 Prompt LSV signal

Impact: Loss of acceptance.

Cuts implemented before evaluating acceptance: Cuts 8.1 through 8.4, and 8.5.1 through 8.5.3.

Evaluation of WIMP acceptance: The acceptance loss was estimated as the probability of there being an uncorrelated signal in the LSV prompt window that accidentally vetoed the TPC event. In particular, 275252 of 5.32×10^7 events in the 530d UAr data satisfied

$$\texttt{veto\_roi\_lsv\_charge\_vec[1]} > 1\ \text{PE}$$

where `veto_roi_lsv_charge_vec[1]` was a 300 ns window (the same width as that used for the actual cut) 2 µs before the prompt time. This was assumed to be an accidental loss of acceptance.

Evaluation of uncertainty on WIMP acceptance: A statistical uncertainty was derived by interpreting the estimated acceptance loss as a binomial process.

The only assumption made for the estimate was to treat all vetoed events as an acceptance loss—there were no systematics that would have lowered the estimated acceptance.

WIMP acceptance: $0.99482 \pm 0.00001_{\text{stat}}$

8.5.5 Delayed LSV signal

Impact: Loss of acceptance.

Cuts implemented before evaluating acceptance: Cuts 8.1 through 8.4, and 8.5.1 through 8.5.4. We note that the delayed slider scanned over a window that overlapped with the 300 ns prompt window; thus it was important for this acceptance measurement that the prompt LSV cut (cut 8.5.4) was applied.

Evaluation of WIMP acceptance: Since the neutron rate in regular UAr running was low, we interpreted all events vetoed by this cut as a loss of acceptance. In the 530d UAr data, 6.35×10^6 of 3.84×10^7 events failed this cut. This was assumed to be an accidental loss of acceptance.

Evaluation of uncertainty on WIMP acceptance: A statistical uncertainty was derived by interpreting the estimated acceptance loss as a binomial process.

The only assumption made for the estimate was to treat all vetoed events as an acceptance loss—there were no systematics that would have lowered the estimated acceptance.

WIMP acceptance: $0.83479 \pm 0.00006_{\text{stat}}$

8.5.6 Pre-prompt LSV signal

Impact: Loss of acceptance.

Cuts implemented before evaluating acceptance: Cuts 8.1 through 8.4, 8.5.1 through 8.5.5.

Evaluation of WIMP acceptance: Since the neutron rate in regular UAr running was low, we interpreted all events vetoed by this cut as a loss of acceptance. In the 530d UAr data, 292362 of 3.84×10^7 events failed this cut. This was assumed to be an accidental loss of acceptance.

Evaluation of uncertainty on WIMP acceptance: A statistical uncertainty was derived by interpreting the estimated acceptance loss as a binomial process.

The only assumption made for the estimate was to treat all vetoed events as an acceptance loss—there were no systematics that would have lowered the estimated acceptance.

WIMP acceptance: $0.99239 \pm 0.00001_{\text{stat}}$

8.6 S1 range

Purpose: The WIMP box (Ch. 7) enforced an S1 range of interest. Because some analysis cuts either involved an S1-dependent threshold, or had an S1-dependent acceptance, we imposed a selection on event S1 for the purposes of calculating cut acceptances.

We note that cut acceptances will be reported as a single value if there is no strong S1-dependence (*e.g.*, for the veto cuts above); if there is a strong S1-dependence, readers will be directed to the accompanying acceptance *vs.* S1 plots.

Cut definition: Selected events with

$$60 < \texttt{total\_s1\_corr} < 460 \text{ PE}$$

Impact: Loss of acceptance.

Cuts implemented before evaluating acceptance: None.

Evaluation of WIMP acceptance: The S1-dependent acceptance loss is obvious.

8.7 Drift time

Impact: We treated the impact of this cut as a loss of fiducial volume/exposure, from an active mass of (46.4 ± 0.7) kg to a fiducial mass of (36.9 ± 0.6) kg [23]. The fiducial volume was derived using the value of the drift time cut, and the estimated electron drift velocity in the LAr (which is different above and below the extraction grid); the uncertainty on the fiducial volume is dominated by the uncertainty on the contraction of TPC (*i.e.*, Teflon) at LAr temperature.

8.8 Number of pulses

Impact: Loss of acceptance.

Cuts implemented before evaluating acceptance: Cuts 8.1 through 8.4, 8.6, and 8.7. There were several aspects to this acceptance estimate; cuts unique to each will be introduced as necessary.

Evaluation of WIMP acceptance: Acceptance was lost via mechanisms that alter the number of pulses.

By creating simulated event waveforms and passing them through the pulse-finding algorithm, Fan reported a 100% pulse-finding efficiency for events in our S1, S2, and drift time range [34, p83].

A WIMP event could gain a pulse from an S1-echo (similar to an S2-echo/S3, but induced by S1). The acceptance loss from this was estimated by counting the number of: 1) Three-pulse events (`n_phys_pulses==3 && has_s3==false`) for which the first and third pulses were separated by 372-400 µs (S1+ S2+ S1-echo); and 2) Four-pulse events (`n_phys_pulses==4`) for which the first and third pulses were separated by 372-400 µs, and the second and fourth pulses were separated by 372-400 µs (S1+ S2+ S1-echo + S2-echo). As can be seen in Fig. 8.4(top), the acceptance loss from this was S1-dependent. This was the main contributor to acceptance loss from this cut.

The S3 pulse could fall outside of the S3 tagging window, hence counting as a disqualifying third pulse in the event. The acceptance loss due to this was estimated on UAr data, by counting the number of three-pulse events (`n_phys_pulses==3 && has_s3==false`) for which the second and third pulses were separated by 367-372 µs, or 400-405 µs. We report an upper bound of 2×10^{-5} for this acceptance loss.

A single-scatter event could pick up extra pulses via random coincidence in the acquisition window. The acceptance loss from this was estimated using pulser-triggered UAr data, implementing only cuts 8.1 through 8.3. 878 events out of 712306 had at least one pulse in the 440 µs acquisition window, for a stray pulse rate of $878/(712306 \times 440\,\mu s) = 2.8\,Hz$. Accordingly, the probability of stray pulses occurring in the window spanning `s1_start_time` to the end of the acquisition win-

dow follows a Poisson distribution with mean $\lambda = 2.8\,\mathrm{Hz} \times 436.05\,\mu\mathrm{s} = 0.001$, for a consequent acceptance loss of 0.001.

The presence of single-pulse events with ER-like S1/F90 in AAr, UAr, and ^{83m}Kr source calibration data, indicated that single-scatter events could sometimes lose their S2 pulse via an unknown mechanism. Two hypotheses were floated for this: 1) This could be scintillation from LAr scatters in various cut-outs in the TPC, for which the ionization electrons could not be collected. In this case, no acceptance corrections had to be made because such irregularities in the active argon volume were already absent from considerations of the fiducial volume/exposure. 2) This could be scintillation from LAr scatters very close to the TPC wall, for which the ionization electrons could occasionally drift into the wall instead of making it to the gas interface for extraction. In this case, acceptance corrections also did not have to be made because of the implementation of radial fiducialization (cut 8.16).

For completeness, an acceptance loss because of S2-loss was nevertheless estimated by comparing the number of single-pulse events (selected using cuts 8.1 through 8.4, and 8.6 through 8.10) with $0.2 < \mathrm{F90} < 0.5$ against the corresponding two-pulse events. This was done using AAr events, which had a uniform spatial distribution within the TPC (Fig. 8.4). Since drift time fiducialization (cut 8.7) could not be implemented on single-pulse events, the events were scaled down by a factor of $36.9/46.4 = 0.795$ to account for the reduced fiducial volume instead. The estimated S1-dependent acceptance is shown in Fig. 8.4(bottom). For the reasons listed above, it is not included in the overall WIMP acceptance estimate. We note that if the loss of drifting ionization electrons into the TPC wall was indeed responsible, correlations between this acceptance, and `total_s2_corr`, ought to be examined.

Evaluation of uncertainty on WIMP acceptance: A statistical uncertainty was derived by interpreting the estimated acceptance loss as a binomial process.

WIMP acceptance: See Fig. 8.4. Notably, the measured acceptance was consistent with that in [34, Fig. 6.7]. The correlation between S1 size and the S1-echo rate was consistent with this being the result of photoionization.

8.9 Start time of S1

Impact: Loss of acceptance.

Cuts implemented before evaluating acceptance: Cuts 8.1 through 8.4, and 8.6 through 8.8; Cuts 8.19.1 and 8.19.2 were used to select NRs from ^{241}AmBe source calibration data.

Evaluation of WIMP acceptance: Since the pulse shape of S1 could conceivably affect where the pulse finding algorithm reconstructed the start time of S1, acceptance was estimated using NRs from ^{241}AmBe source calibration data.

Evaluation of uncertainty on WIMP acceptance: A statistical uncertainty was derived by interpreting the estimated acceptance loss as a binomial process; a consequence of this approach was that an estimated acceptance of 1 came with an uncertainty of 0.

The validity of the acceptance estimate hinged on how representative the selected sample of NRs was of WIMP events. Thus, systematic uncertainties were estimated by varying cut 8.19.2 as described therein; 8.19.1 was necessary as a safeguard against potential biasing of the acceptance estimate by γ-ray-induced Cherenkov radiation in the fused silica or Teflon volumes.

WIMP acceptance: Consistent with 1 ($>$0.999) (Fig. 8.5)

8.10 S1 saturation

Impact: Loss of acceptance.

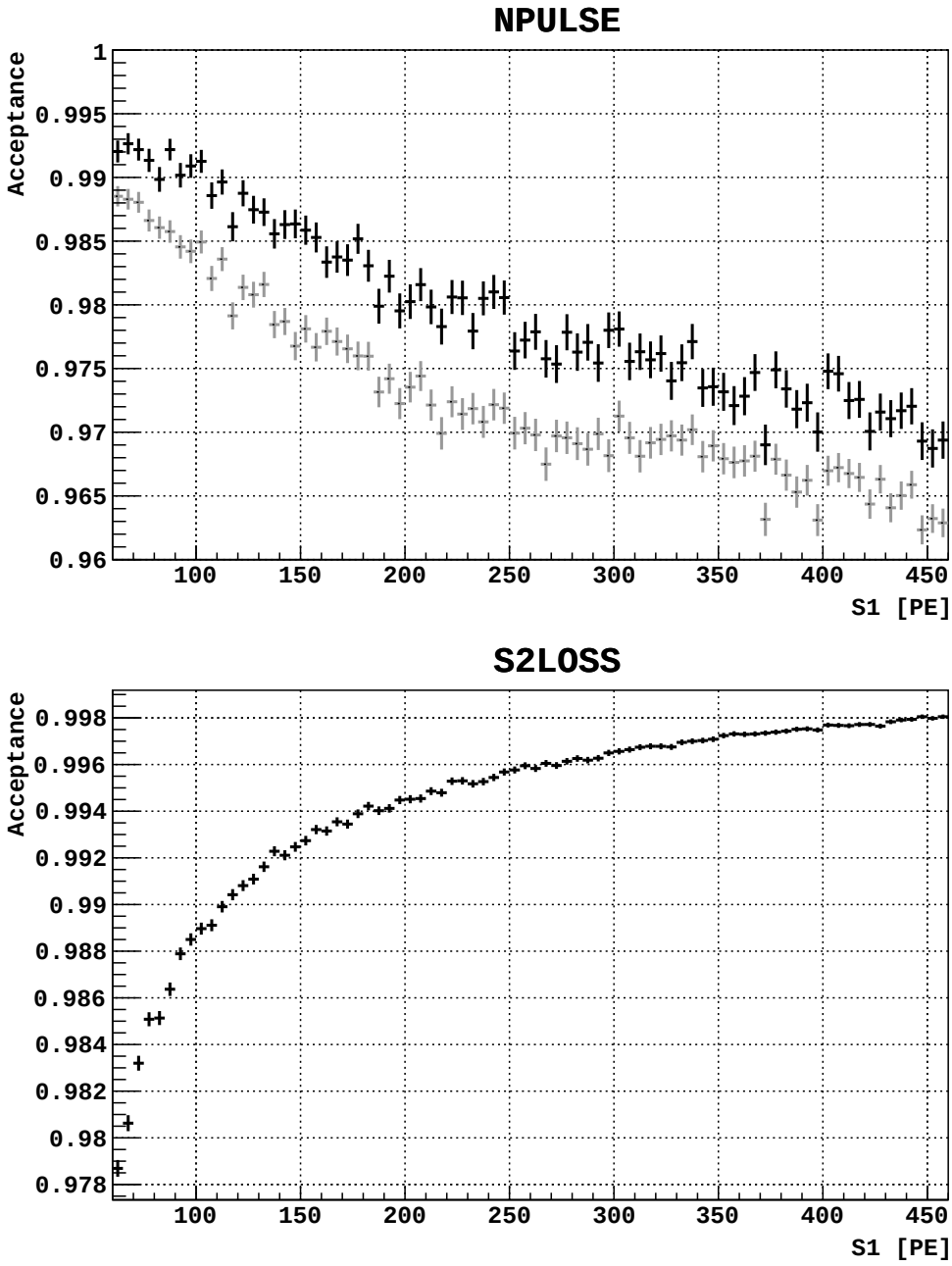

Figure 8.4: WIMP acceptance of the number of pulses/single-scatter cut, estimated on UAr data. **Top:** From gaining a pulse due to an S1-echo; systematics are presented in gray. **Bottom:** From losing a pulse, possibly due to loss of the S2 pulse; this is not included in the overall WIMP acceptance estimate (see text for details).

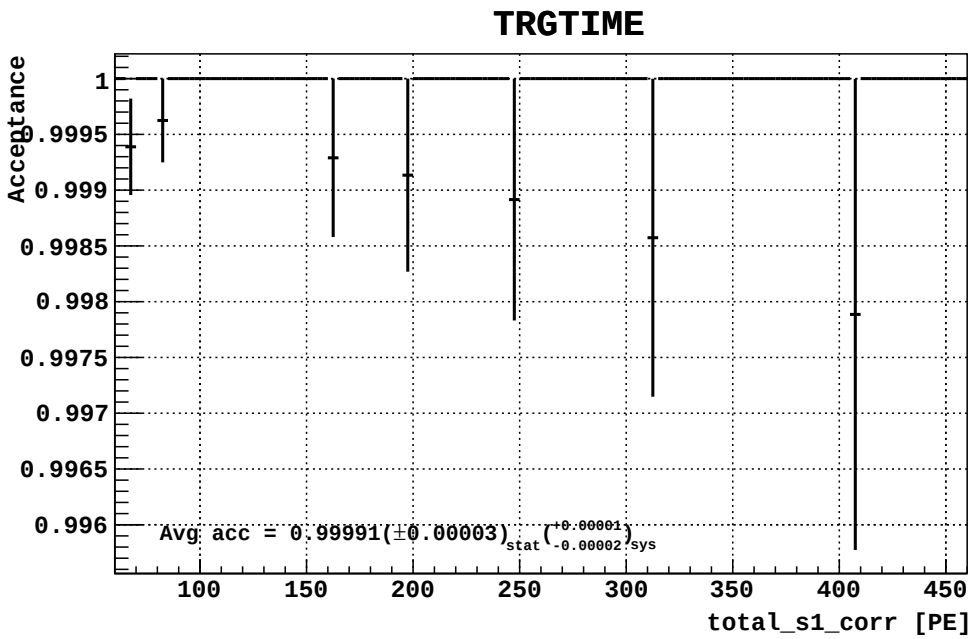

Figure 8.5: WIMP acceptance of the S1 start time cut, estimated on ^{241}AmBe nuclear recoil data. Presented error bars are the binomial statistical error per S1 bin.

Cuts implemented before evaluating acceptance: Cuts 8.1 through 8.4, and 8.6 through 8.9; Cuts 8.19.1 and 8.19.2 were used to select NRs from ^{241}AmBe source calibration data.

Evaluation of WIMP acceptance: Since a sharper pulse shape (as indicated by higher F90) could conceivably be more susceptible to saturation, acceptance was estimated using NRs from ^{241}AmBe source calibration data.

Evaluation of uncertainty on WIMP acceptance: A statistical uncertainty was derived by interpreting the estimated acceptance loss as a binomial process.

Systematic uncertainties were estimated by varying cut 8.19.2 as described therein.

WIMP acceptance: 1 (Fig. 8.6)

8.11 Uncorrected S2

Impact: Loss of acceptance.

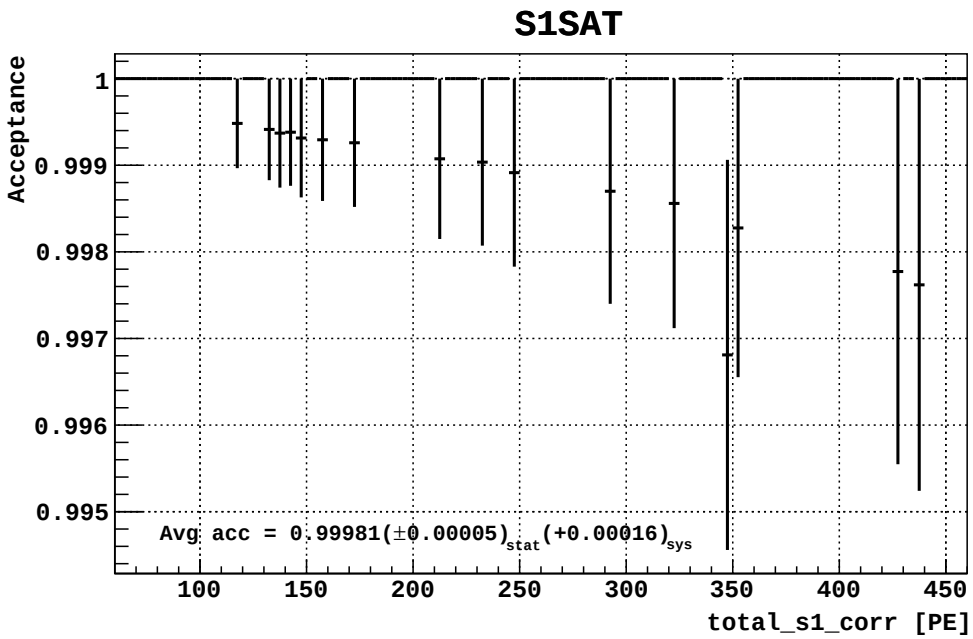

Figure 8.6: WIMP acceptance of the S1 saturation cut, estimated on ^{241}AmBe nuclear recoil data. Presented error bars are the binomial statistical error per S1 bin.

Cuts implemented before evaluating acceptance: Cuts 8.1 through 8.4, and 8.6 through 8.10; Cuts 8.19.1 and 8.19.2 were used to select NRs from ^{241}AmBe source calibration data.

Evaluation of WIMP acceptance: Acceptance was estimated using NRs from ^{241}AmBe source calibration data. Because the AmBe events tended to occur closer to the TPC wall—where the S2 light yield was known to be lower than it was closer to the center of the TPC—the estimated acceptance was conservative.

Evaluation of uncertainty on WIMP acceptance: A statistical uncertainty was derived by interpreting the estimated acceptance loss as a binomial process.

Systematic uncertainties were estimated by varying cut 8.19.2 as described therein.

WIMP acceptance: $0.9963 \pm 0.00020_{\text{stat}} - 0.00007_{\text{sys}}$ (Fig. 8.7). The impact on the xy-reconstruction efficiency is shown in Fig. 8.8.

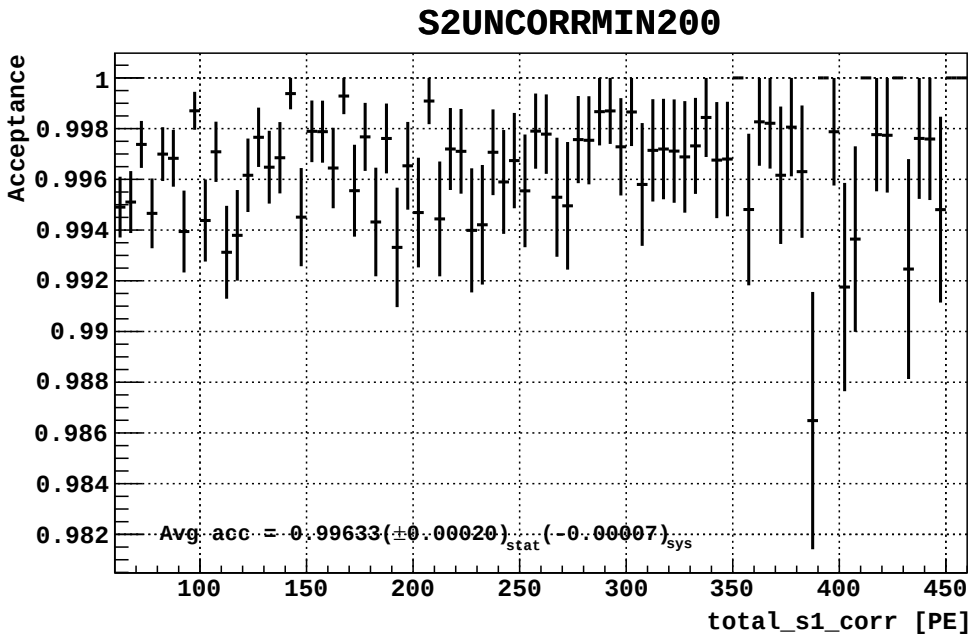

Figure 8.7: WIMP acceptance of the minimum uncorrected S2 cut, estimated on ^{241}AmBe nuclear recoil data. Presented error bars are the binomial statistical error per S1 bin.

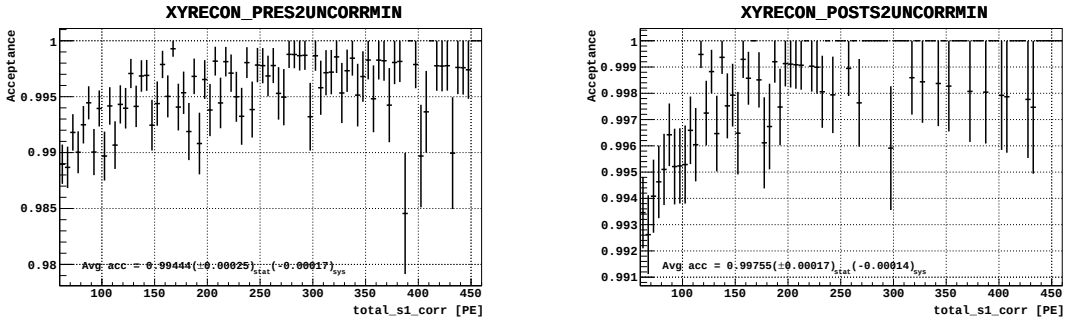

Figure 8.8: Efficiency of the xy-algorithm at reconstructing ^{241}AmBe nuclear recoil events (left) before, and (right) after, the application of a minimum uncorrected S2 cut.

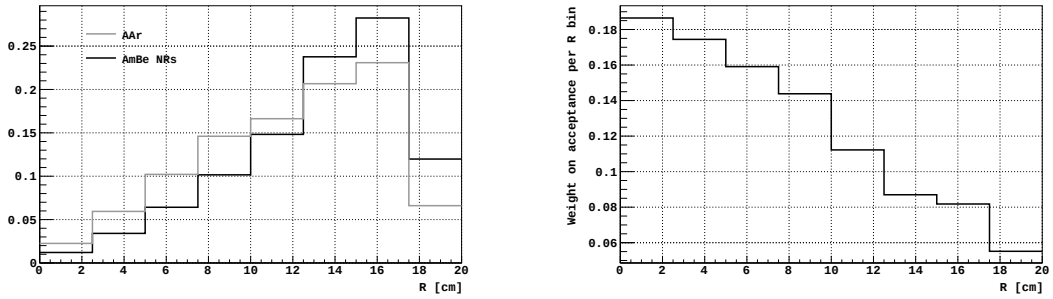

Figure 8.9: **Left:** Distribution of AAr and ^{241}AmBe NR events across various radial bins; **Right:** Weighting per radial bin used on acceptances calculated using ^{241}AmBe NRs.

8.12 S2 cuts

Acceptance estimates for S2 cuts were done on NRs from ^{241}AmBe source calibration data, since $^{S2}/_{S1}$ is lower for NRs than for ERs. However, ^{241}AmBe neutrons tend to scatter at larger TPC radii, as they came from an external source (Fig. 8.9). Since S2 varied with radius, this spatial non-uniformity had to be accounted for. This was done by weighting the contribution of different radial bins to the overall acceptance estimate, using the radial distribution of AAr events as a target profile. The net effect was that in each S1 bin, the acceptance of events at smaller radii were weighted more heavily in the acceptance estimate. A rather coarse radial binning of 2.5 cm was used so that there were no empty (radius, S1) bins.

8.12.1 S2 F90

Impact: Loss of acceptance.

Cuts implemented before evaluating acceptance: Cuts 8.1 through 8.4, and 8.6 through 8.11; Cuts 8.19.1 and 8.19.2 were used to select NRs from ^{241}AmBe source calibration data.

Evaluation of WIMP acceptance: Acceptance was estimated using NRs from ^{241}AmBe source calibration data.

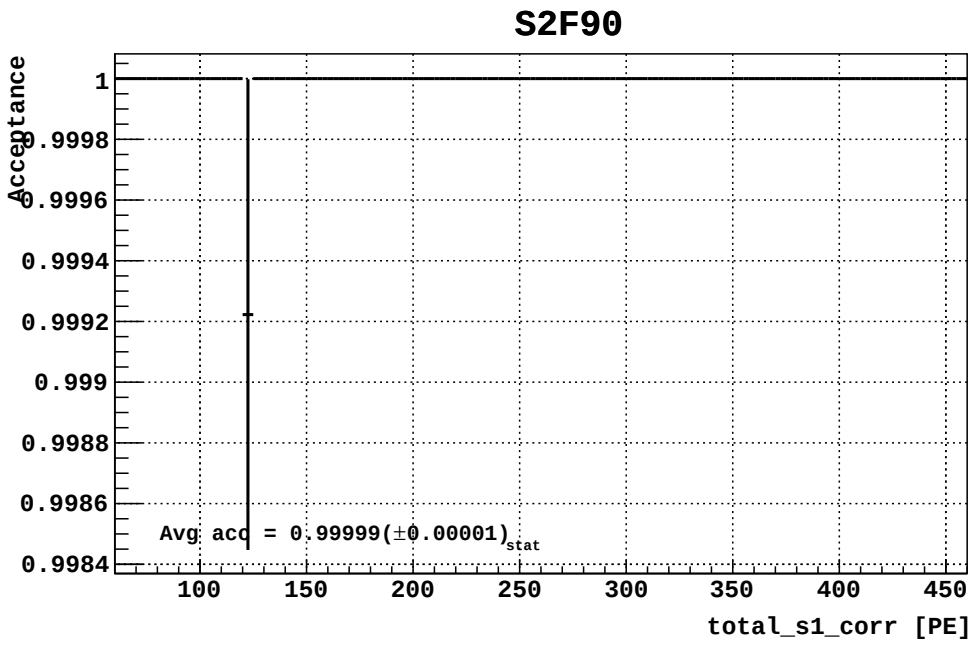

Figure 8.10: WIMP acceptance of the S2 F90 cut, estimated on ^{241}AmBe nuclear recoil data. Presented error bars are the binomial statistical error per S1 bin.

Evaluation of uncertainty on WIMP acceptance: A statistical uncertainty was derived by interpreting the estimated acceptance loss as a binomial process.

Systematic uncertainties were estimated by varying cut 8.19.2 as described therein.

WIMP acceptance: 1 (Fig. 8.10)

8.12.2 Minimum corrected S2/S1

Impact: Loss of acceptance.

Cuts implemented before evaluating acceptance: Cuts 8.1 through 8.4, and 8.6 through 8.12.1; Cuts 8.19.1 and 8.19.2 were used to select NRs from ^{241}AmBe source calibration data.

Evaluation of WIMP acceptance: Acceptance was estimated using NRs from ^{241}AmBe source calibration data.

Evaluation of uncertainty on WIMP acceptance: A statistical uncertainty was derived by interpreting the estimated acceptance loss as a binomial process.

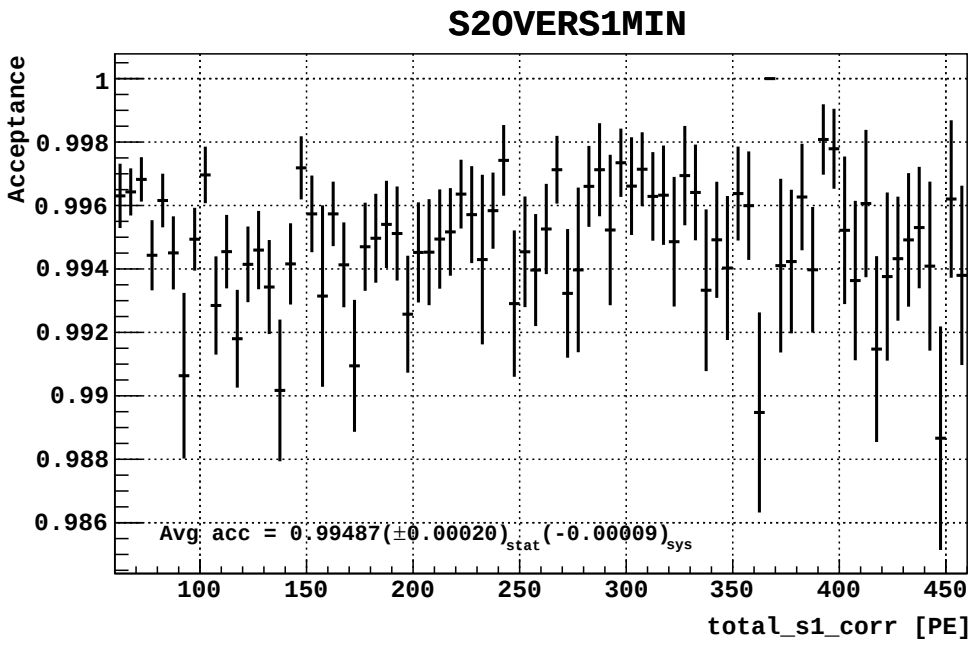

Figure 8.11: WIMP acceptance of the minimum corrected S2/S1cut, estimated on ^{241}AmBe nuclear recoil data. Presented error bars are the binomial statistical error per S1 bin.

Systematic uncertainties were estimated by varying 8.19.2 as described therein.

WIMP acceptance: $0.99487 \pm 0.00020_{\text{stat}} - 0.00009_{\text{sys}}$ (Fig. 8.11). This is consistent with the cut thresholds having been set to have an acceptance of 0.99 using ^{241}AmBe calibration data.

8.12.3 Maximum corrected S2/S1

Impact: Loss of acceptance.

Cuts implemented before evaluating acceptance: Cuts 8.1 through 8.4, and 8.6 through 8.12.2; Cuts 8.19.1 and 8.19.2 were used to select NRs from ^{241}AmBe source calibration data.

Evaluation of WIMP acceptance: Acceptance was estimated using NRs from ^{241}AmBe source calibration data.

Evaluation of uncertainty on WIMP acceptance: A statistical uncertainty was derived by interpreting the estimated acceptance loss as a binomial process.

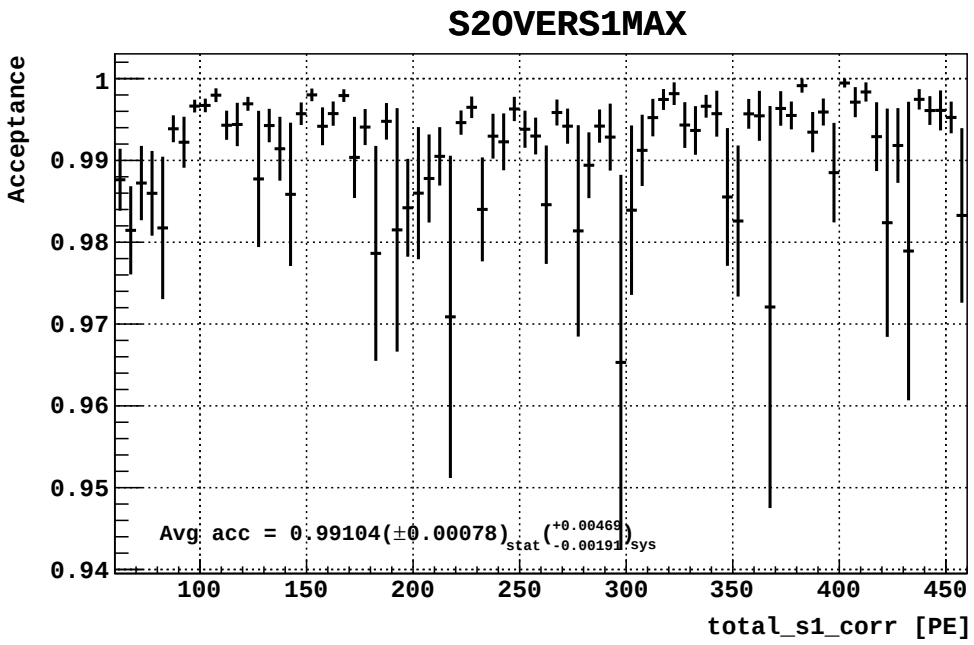

Figure 8.12: WIMP acceptance of the maximum S2/S1 cut, estimated on ^{241}AmBe nuclear recoil data. Presented error bars are the binomial statistical error per S1 bin.

Systematic uncertainties were estimated by varying cut 8.19.2 as described therein.

WIMP acceptance: $0.9910 \pm 0.0008_{\text{stat}}{}^{+0.0047}_{-0.0019_{\text{sys}}}$ (Fig. 8.12)

8.12.4 Early S2 pulse shape

Impact: Loss of acceptance.

Cuts implemented before evaluating acceptance: Cuts 8.1 through 8.4, and 8.6 through 8.12.3; Cuts 8.19.1 and 8.19.2 were used to select NRs from ^{241}AmBe source calibration data.

Evaluation of WIMP acceptance: Acceptance was estimated using NRs from ^{241}AmBe source calibration data.

Evaluation of uncertainty on WIMP acceptance: A statistical uncertainty was derived by interpreting the estimated acceptance loss as a binomial process.

Systematic uncertainties were estimated by varying cut 8.19.2 as described therein.

WIMP acceptance: $0.99969 \pm 0.00019_{\text{stat}}{}^{+0.00001}_{-0.00011_{\text{sys}}}$ (Fig. 8.13); consistent with 1.

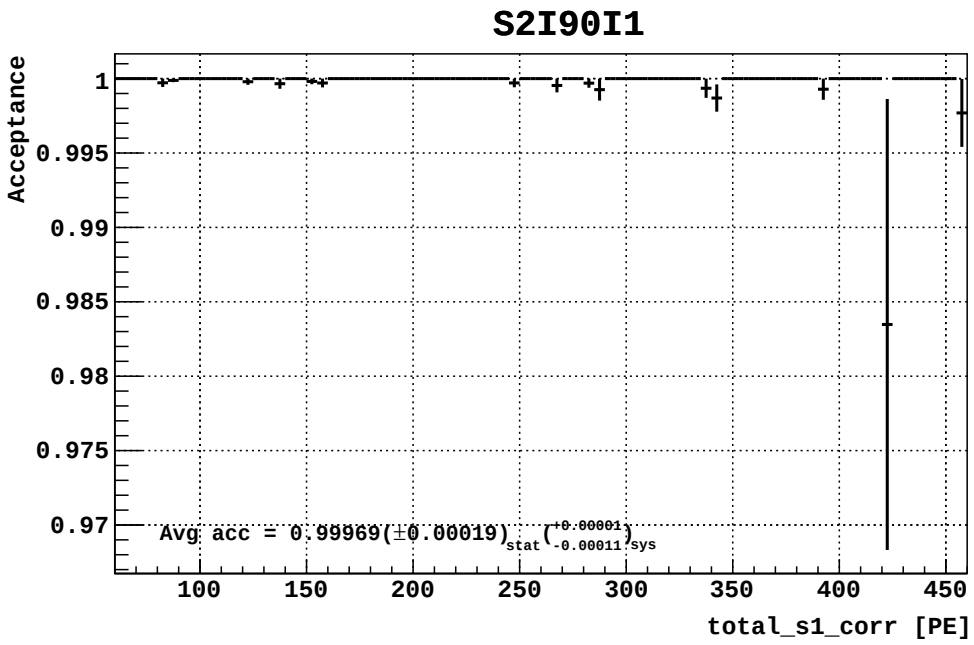

Figure 8.13: WIMP acceptance of the early S2 pulse shape cut, estimated on ^{241}AmBe nuclear recoil data. Presented error bars are the binomial statistical error per S1 bin.

8.13 S1 prompt maximum fraction

Impact: Loss of acceptance.

Cuts implemented before evaluating acceptance: Cuts 8.1 through 8.4, and 8.6 through 8.12.4; Cuts 8.19.1 and 8.19.2 were used to select NRs from ^{241}AmBe source calibration data.

Evaluation of WIMP acceptance: Since the cut thresholds were set by looking at AAr data, we checked the acceptance estimate on NRs from ^{241}AmBe source calibration data. It was necessary to implement cut 8.7 because the cut threshold involved a lookup using both S1 and drift time.

Evaluation of uncertainty on WIMP acceptance: A statistical uncertainty was derived by interpreting the estimated acceptance loss as a binomial process.

Systematic uncertainties were estimated by varying cut 8.19.2 as described therein. Since the distribution of S1 light—and hence S1 prompt maximum fraction—could be affected by the radial position of an event, a systematic uncertainty was also

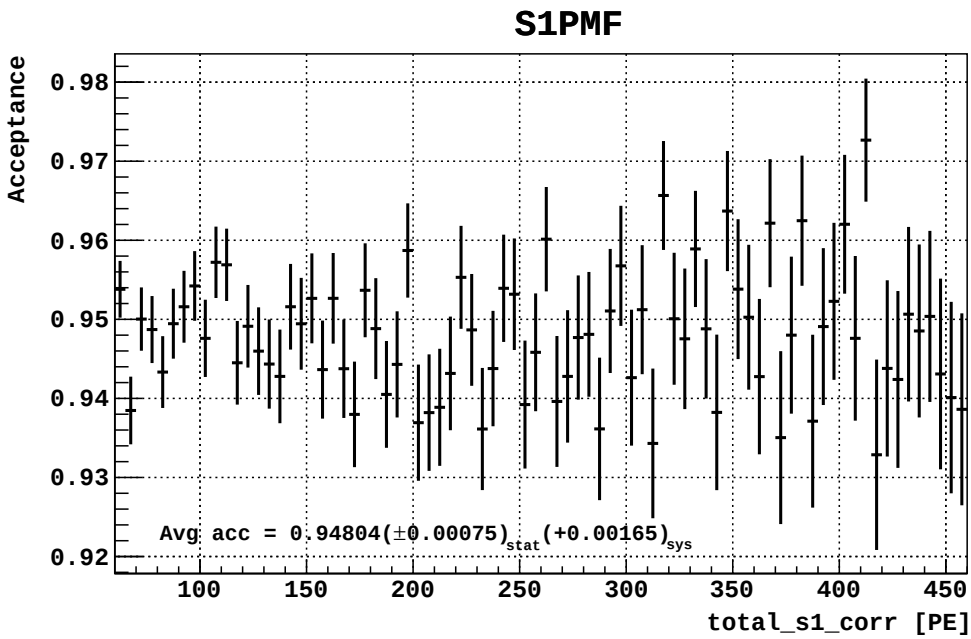

Figure 8.14: WIMP acceptance of the S1prompt maximum fraction cut, estimated on ^{241}AmBe nuclear recoil data. Presented error bars are the binomial statistical error per S1 bin.

estimated by weighting the contribution of different radial bins to the overall acceptance estimate, to account for the spatial non-uniformity of the ^{241}AmBe data (see Sec. 8.12).

WIMP acceptance: $0.9480 \pm 0.0008_{\text{stat}} + 0.0016_{\text{sys}}$ (Fig. 8.14). This was consistent with the designed acceptance on AAr data of 0.95. The reported systematic comes from using the radial bin weighting on the tighter version of cut 8.19.2.

8.14 S1 top bottom asymmetry

Impact: Loss of acceptance.

Cuts implemented before evaluating acceptance: Cuts 8.1 through 8.4, and 8.6 through 8.13; Cuts 8.19.1 and 8.19.2 were used to select NRs from ^{241}AmBe source calibration data.

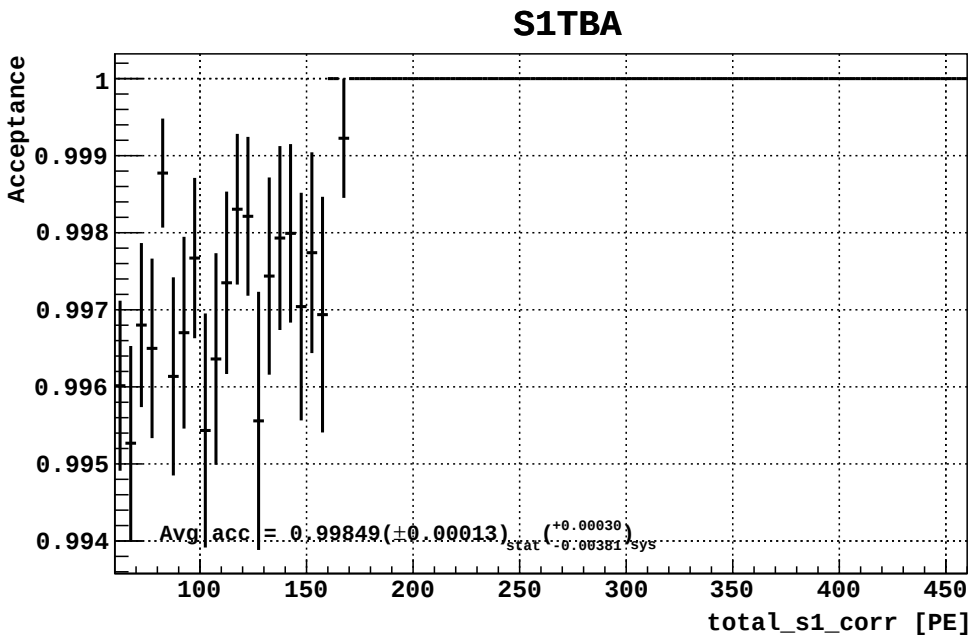

Figure 8.15: WIMP acceptance of the S1 top bottom asymmetry cut, estimated on ^{241}AmBe nuclear recoil data. Presented error bars are the binomial statistical error per S1 bin.

Evaluation of WIMP acceptance: Since the cut was designed using AAr data, we checked the acceptance estimate on NRs from ^{241}AmBe source calibration data. It was necessary to implement cut 8.13 because events with high S1pmf also had skewed TBA. Cut 8.7 was necessary because the cut threshold was varied with both S1 and drift time.

Evaluation of uncertainty on WIMP acceptance: A statistical uncertainty was derived by interpreting the estimated acceptance loss as a binomial process.

Systematic uncertainties were estimated by varying 8.19.2 as described therein. Since the cut looked at how the S1 light was distributed, a systematic uncertainty was also estimated by weighting the contribution of different radial bins to the overall acceptance estimate, to account for the spatial non-uniformity of the ^{241}AmBe data (see 8.12).

WIMP acceptance: $0.9985 \pm 0.0001_{\mathrm{stat}}{}^{+0.0003}_{-0.0038_{\mathrm{sys}}}$ (Fig. 8.15). We note that the acceptance loss measured appeared to be concentrated in the lower S1 bins.

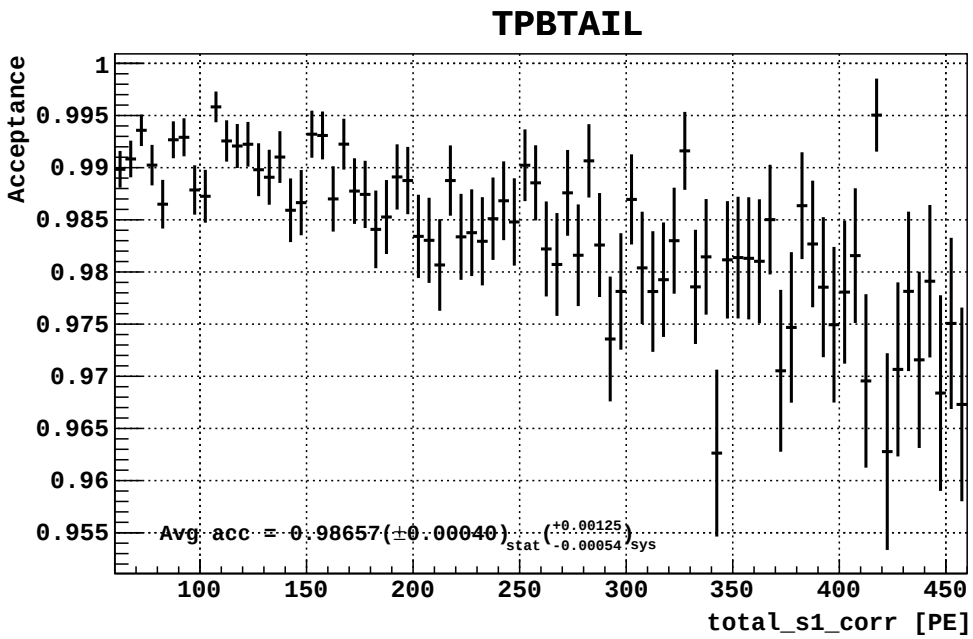

Figure 8.16: WIMP acceptance of the long S1 tail cut, estimated on ^{241}AmBe nuclear recoil data. Presented error bars are the binomial statistical error per S1 bin.

8.15 Long S1 tail

Impact: Loss of acceptance.

Cuts implemented before evaluating acceptance: Cuts 8.1 through 8.4, and 8.6 through 8.14; Cuts 8.19.1 and 8.19.2 were used to select NRs from ^{241}AmBe source calibration data.

Evaluation of WIMP acceptance: Acceptance was estimated using NRs from ^{241}AmBe source calibration data to account for the possibility of normal NRs in the LAr generating a similar long-lived signal.

Evaluation of uncertainty on WIMP acceptance: A statistical uncertainty was derived by interpreting the estimated acceptance loss as a binomial process.

Systematic uncertainties were estimated by varying cut 8.19.2 as described therein.

WIMP acceptance: $0.98657 \pm 0.0004_{\text{stat}}{}^{+0.0013}_{-0.0005_{\text{sys}}}$ (Fig. 8.16). This is consistent with the cut thresholds having been set to have an acceptance of 0.99 using ^{241}AmBe calibration data. There appeared to be a slight S1 dependence.

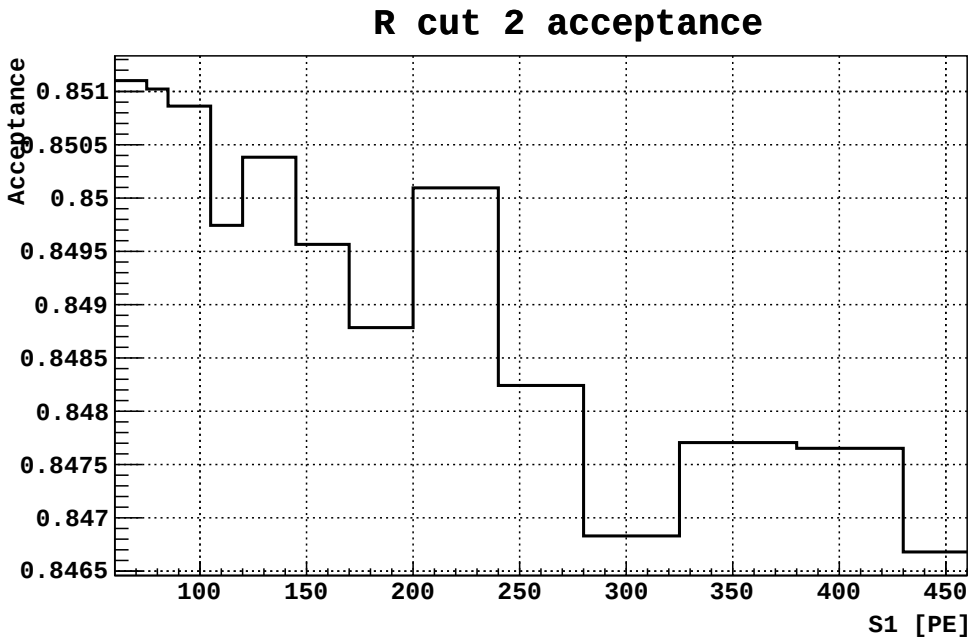

Figure 8.17: WIMP acceptance of the radial cut *vs.* S1, estimated using AAr and ^{241}AmBe data.

8.16 Radial fiducialization

Impact: Loss of acceptance.

Evaluation of WIMP acceptance: The acceptance was estimated using both the AAr and ^{241}AmBe source calibration data to leverage the former's uniform distribution in the TPC and the latter's NR $^{S2}/_{S1}$ response. The cut's acceptance *vs.* S2 was first estimated using uniformly distributed ^{39}Ar events in the AAr data; then, the acceptance *vs.* NR S1 was estimated by using $^{S2}/_{S1}$ from NRs in ^{241}AmBe data to look up the acceptance in the appropriate AAr S2 bin. This scheme was developed by Granato, Wada, and Zhu.

WIMP acceptance: See Fig. 8.17.

8.17 Negative log-likelihood of S1 light distribution

Impact: Loss of acceptance.

Cuts implemented before evaluating acceptance: Cuts 8.1 through 8.4, and 8.6 through 8.16; Cuts 8.19.1 and 8.19.2 were used to select NRs from ^{241}AmBe source calibration data.

Evaluation of WIMP acceptance: Acceptance was estimated using NRs from ^{241}AmBe source calibration data.

Evaluation of uncertainty on WIMP acceptance: A statistical uncertainty was derived by interpreting the estimated acceptance loss as a binomial processs.

Systematic uncertainties were estimated by varying cut 8.19.2 as described therein.

WIMP acceptance: >0.99. The cut thresholds were set to accept 0.99 of ^{241}AmBe NRs where there was voxel coverage. Since it passed events not under a voxel, 0.99 was a lower limit on the cut's acceptance (Fig. 8.18).

8.18 Summary

The cut acceptances derived in this chapter are summarized in Tab. 8.1. The combined cut acceptances *vs.* S1 is shown in Fig. 8.19; the acceptance of the WIMP search region, estimated using the simulation used for setting the limit on the WIMP-nucleon scattering cross-section (Ch. 9), is also shown.

8.19 Selecting neutrons from calibration data

Here we summarize the cuts applied to select NR events from the ^{241}AmBe source calibration data, which were used for estimating the WIMP acceptance of some analysis cuts. These were necessary because the ^{241}AmBe source also emitted γ-rays at

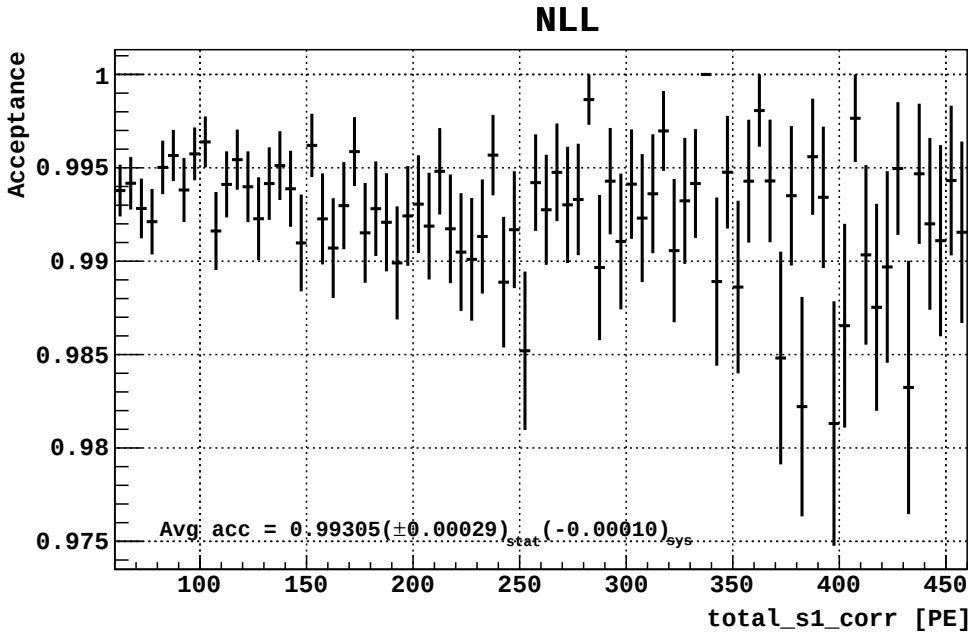

Figure 8.18: WIMP acceptance of the S1 light distribution negative log-likelihood cut, estimated on ^{241}AmBe nuclear recoil data. Presented error bars are the binomial statistical error per S1 bin.

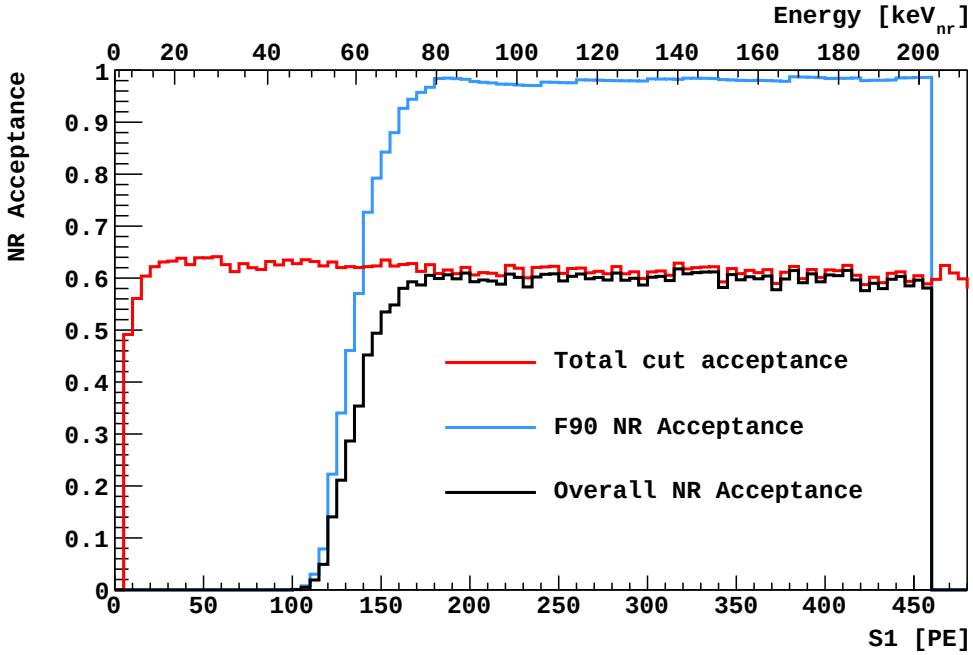

Figure 8.19: Combined WIMP acceptance of cuts, including that of the WIMP search region for the 530d UAr analysis ("F90 NR acceptance").

Table 8.1: Summary of cuts, and their respective impact on livetime and WIMP acceptance. The average acceptance of S1-dependent cuts are presented; acceptances >0.999 are shown as 1.

Cut	Livetime / Acceptance	Stat.	Syst.	S1-dep?
Trigger type (8.1)	545.6 d	-	-	-
Number of channels (8.2)	545.6 d	-	-	-
Baseline (8.3)	545.6 d	-	-	-
Livetime (8.4)	545.3 d	-	-	-
Veto present (8.5.1)	536.6 d	-	-	-
Cosmogenic activation (8.5.3)	532.4 d	-	-	-
Muon signal (8.5.2)	0.990	0.00001	-	No
Prompt LSV signal (8.5.4)	0.995	0.00001	-	No
Delayed LSV signal (8.5.5)	0.835	0.00006	-	No
Preprompt LSV signal (8.5.6)	0.992	0.00001	-	No
Number of pulses (8.8)	0.978	-	-	Yes
S1 start time (8.9)	1	-	-	No
S1 saturation (8.10)	1	-	-	No
Minimum uncorrected S2 (8.11)	0.996	0.00020	-0.00007	No
xy-reconstruction efficiency (8.11)	0.997	0.00017	-0.00005	Yes
S2 F90 (8.12.1)	1	-	-	No
Minimum corrected S2S1 (8.12.2)	0.995	0.00020	-0.00009	No
Maximum corrected S2S1 (8.12.3)	0.991	0.0008	$^{+0.0047}_{-0.0019}$	No
Early S2 pulse shape (8.12.4)	1	-	-	No
S1 prompt maximum fraction (8.13)	0.948	0.0008	0.0016	No
S1 top bottom asymmetry (8.14)	0.998	0.0001	$^{+0.0003}_{-0.0038}$	Yes
Long S1 tail (8.15)	0.987	0.0004	$^{+0.0013}_{-0.0005}$	Yes
Radial cut (8.16)	$\sim$0.85	-	-	Yes
S1 light distribution NLL (8.17)	0.99	0.0003	-	No
Combined	0.620 (Fig. 8.19)	0.001	$^{+0.005}_{-0.004}$	-

a high rate. Note that these were not standard WIMP search cuts; as such, WIMP acceptance will not be estimated.

8.19.1 Prompt LSV signal

Purpose: In the LSV, we tagged the signal of the 4.4 MeV γ-ray from the decay of ^{13}C* to ^{12}C that produces the neutrons:

$$^{9}\mathrm{Be} + \alpha \rightarrow^{13} \mathrm{C}^{*} \rightarrow^{12} \mathrm{C} + \mathrm{n} + \gamma \tag{8.1}$$

(often abbreviated to ^{9}Be(α, n)^{12}C in nuclear physics literature) where the instigating α-particle is from ^{241}Am decay.

Cut definition: Selected events with

$$2400 < \texttt{veto\_roi\_lsv\_charge\_vec[0]} < 3800 \text{ PE}$$

8.19.2 F90

Purpose: The LSV signal selection (cut 8.19.1) allowed for the γ-ray to deposit some of its energy in the TPC. To clean the data of mixed (Compton scatter + nuclear recoil) events, an additional selection on F90 was implemented.

Cut definition: Selected events with

$$\texttt{total\_f90} > \texttt{total\_f90\_thres(NR 99\% acceptance)}$$

where `total_f90_thres(NR 99% acceptance)` was the F90 contour denoting 99% NR acceptance made for the 70d UAr analysis. For estimating systematic uncertainties, tighter and looser versions of this contour were used, where events were selected with

$$\texttt{total\_f90\_thres(NR median - 1}\,\sigma\texttt{)} < \texttt{total\_f90} < \texttt{total\_f90\_thres(NR median + 1}\,\sigma\texttt{)}$$

and

$$\texttt{total\_f90} > \texttt{total\_f90\_thres(NR 99\% acceptance)} - 0.1$$

respectively.

Discussion: We note that the 530d UAr WIMP box was fully contained within the F90 region above the 99% NR acceptance contour.

8.20 70d UAr analysis WIMP box

Purpose: For completeness, we estimated the acceptance of the 70d UAr WIMP box on ^{241}AmBe NR data, as a function of S1.

Cut definition: Selected events with

$$\texttt{total\_f90} > \texttt{total\_f90\_thres(70d WIMP box)}$$

Cuts implemented before evaluating acceptance: Cuts 8.1 through 8.4, 8.8, 8.6, 8.19.1, and 8.19.2.

Evaluation of uncertainty on WIMP acceptance: A statistical uncertainty was derived by interpreting the estimated acceptance loss as a binomial process.

WIMP acceptance: See Fig. 8.20.

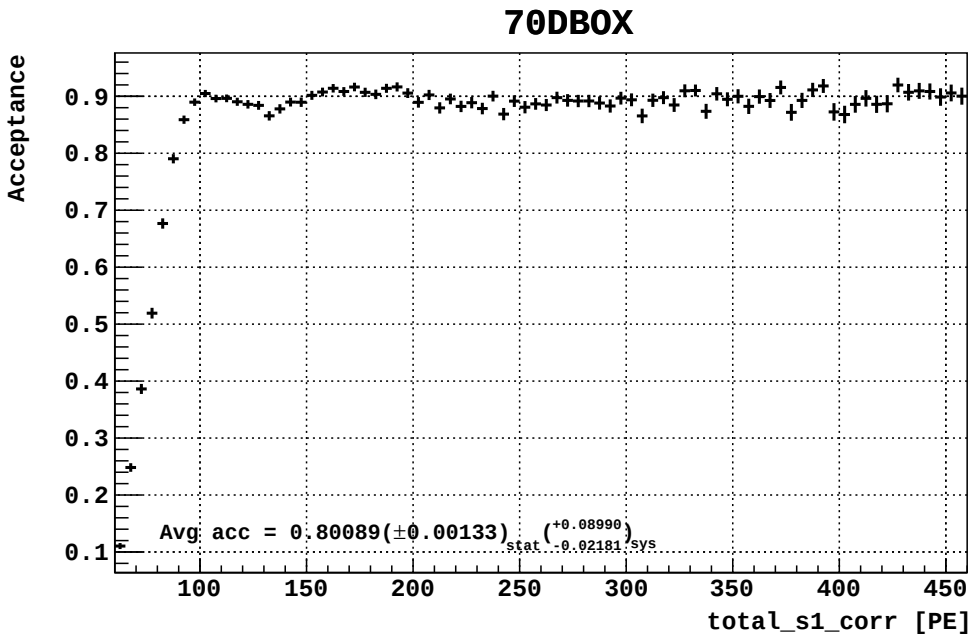

Figure 8.20: WIMP acceptance of the 70d UAr WIMP box, estimated on ^{241}AmBe nuclear recoil data.

Chapter 9

Setting the limit on the WIMP-nucleon scattering cross-section

With the analysis cuts (including the WIMP search region) finalized, and their WIMP acceptances estimated, the pieces were in place to calculate the limit on the WIMP-nucleon scattering cross-section (assuming a background- and signal- free result). In this chapter we describe the procedure used to do this.

9.1 Method overview

1. A WIMP mass $M_\chi \in [10, 10000]$ GeV/c^2 was picked.

2. The differential energy spectrum $\frac{dR}{dE_R}$ *vs.* nuclear recoil energy E_R was generated using M_χ and a reference WIMP-nucleon cross-section σ_n as input.

3. The number of WIMP-argon recoils N to simulate for this M_χ was chosen.

4. For each scatter:

- E_R was randomly drawn using $\frac{dR}{dE_R}$ as a probability distribution.
- An expected S1 signal for this E_R was derived.
- The WIMP acceptance of our analysis cuts was applied, *i.e.*, each simulated event passed or failed the cuts with a binomial probability equal to the WIMP acceptance.
- S1 was smeared to account for photoelectron counting statistics.
- F90 was drawn from an analytic model fitted to the ^{241}AmBe source calibration data.

5. The number of simulated WIMP-argon scatter events passing the analysis cuts and with (S1, F90) in the WIMP box was counted (N_{box}). From this count, the scattering cross-section that would have given 2.3 events in the box instead was derived:

$$\sigma_{90\%\ \text{UL}}(M_\chi) = \frac{2.3}{N_{\text{box}}} \times \sigma_n \tag{9.1}$$

6. The process was repeated with other WIMP masses.

9.2 Simulated WIMP masses

60 WIMP masses $M_\chi \in [10, 10000]$ GeV/c^2 were simulated; $M_{\chi,i}$ of the i-th step was $10^{1+0.05i}$ GeV/c^2.

9.3 Differential WIMP-argon recoil rate

The canonical reference for this derivation is [63]; here, we follow the work of Loer [21], done for DarkSide-10.

Table 9.1: Summary of constant inputs for modeling the differential WIMP-argon recoil rate. For backward-compatibility, we have assumed values used in previous DS-50 analyses.

	Description	Value [ref.]	Dimension
N_0	Avogadro's number	6.02×10^{23}	mol^{-1}
A	Atomic mass of target nucleus (Ar)	39.948	$\mathrm{g\,mol}^{-1}$
M_T	Mass of target nuclear (Ar)	$A \times 0.93149$	$\mathrm{GeV/c}^2$
ρ_χ	WIMP mass density	0.3 [64]	$\mathrm{GeVc}^{-2}\mathrm{cm}^{-3}$
v_E	Earth's velocity relative to the WIMP halo	232 [65]	$\mathrm{km\,s}^{-1}$
v_{esc}	Galactic escape velocity	544 [66]	$\mathrm{km\,s}^{-1}$
v_0	WIMP dispersion velocity in the halo frame	220 [66]	$\mathrm{km\,s}^{-1}$
s	Nuclear skin thickness	0.9 [63, Sec. 4]	fm
r_n	Nuclear radius	3.9 [63, Sec. 4]	fm

The functional form used for the differential recoil rate $\frac{dR}{dE_R}$, conventionally expressed in [event $\mathrm{keV}^{-1}\mathrm{kg}^{-1}_{\mathrm{target}}\mathrm{d}^{-1}$], was [21, Eqn. 1.25]

$$\frac{dR}{dE_R} = \frac{N_0}{A}\sigma\rho_\chi\frac{M_T}{2M_\chi\mu^2}\int\frac{f(v_\chi, v_E, v_{\mathrm{esc}})}{v_\chi}dv_\chi \times 86400\,\mathrm{s\,d}^{-1} \times 10^{-4} \times c^2 \tag{9.2}$$

where σ was the WIMP-target nucleus scattering cross-section, $\mu = M_T M_\chi/(M_T + M_\chi)$ was the reduced mass of the WIMP-target nucleus system, f was the WIMP velocity distribution, and v_χ was the WIMP velocity in the lab frame. Constants and their assumed values are summarized in Tab. 9.1. The extra factor of c^2 was included to account for the use of natural units in the mass terms.

To get the WIMP-target nucleus scattering cross-section, the WIMP-nucleon scattering cross-section σ_n was corrected with a form factor [21, Eqn. 1.29]

$$\sigma = \sigma_n[A\frac{\mu}{\mu_n}F(q)]^2 \tag{9.3}$$

where μ_n was the reduced mass of the WIMP-nucleon system, $q = \sqrt{2M_T E_R}$ was the momentum transfer in the nuclear recoil, and $F(q)$ was the nuclear form factor [21,

Eqn. 1.28]

$$F(q) = 3\frac{j_1(qr_n)}{qr_n}e^{-\frac{1}{2}(qs)^2} \tag{9.4}$$

where $j_1(x) = (\sin x - x\cos x)/x^2$ was a spherical Bessel function of the first kind, and

$$\begin{aligned} r_n^2 &= (1.23A^{1/3} - 0.6)^2 + 7\pi^2 0.52^2/3 - 5s^2 \\ r_n &\approx 3.90\,\text{fm} \end{aligned} \tag{9.5}$$

was the nuclear radius [63, Eqn. 4.11]; the constants A and s are summarized in Tab. 9.1.

Finally, the integral $\int f(v_\chi, v_E, v_{\text{esc}})/v_\chi dv_\chi$ had the form [21, Eqn. 1.40]

$$\int \frac{f}{v_\chi}dv_\chi = \begin{cases} C[\text{erf}(x) - \text{erf}(y) - \frac{2(x-y)}{v_0\sqrt{\pi}}e^{-z^2}] & \text{for } (v_{\text{min}} - v_{\text{esc}}) < -v_E \\ C[\text{erf}(z) - \text{erf}(y) - \frac{2(z-y)}{\sqrt{\pi}}e^{-z^2}] & \text{for } -v_E < (v_{\text{min}} - v_{\text{esc}}) < v_E \end{cases} \tag{9.6}$$

where

$$\begin{aligned} x &= \frac{v_{\text{min}} + v_E}{v_0} \\ y &= \frac{v_{\text{min}} - v_E}{v_0} \\ z &= \frac{v_{\text{esc}}}{v_0} \end{aligned} \tag{9.7}$$

C was a normalization factor

$$\frac{1}{C} = 2v_E(\text{erf}(z) - 2\frac{z}{\sqrt{\pi}}e^{z^2}) \tag{9.8}$$

and

$$v_{\text{min}} = \sqrt{\frac{E_R(M_T + M_\chi)^2}{2M_T M_\chi^2}} \tag{9.9}$$

was the minimum WIMP velocity required for a scatter with recoil energy E_R (derived in A).

We note that three variables have not yet been specified—M_χ, σ_n, and E_R. As mentioned in Sec. 9.2, various values of M_χ were used; separately, a high value for σ_n of $1 \times 10^{-38}\,\mathrm{cm}^2$ was also assumed to obtain large statistics of simulated recoils. With these variables defined, Eqn. 9.2 gave the differential recoil rate as a function of recoil energy—*i.e.*, it was the recoil energy spectrum—, and was used as the probability distribution from which recoil energies were drawn.

9.4 Generating scatter S1 and F90, and accounting for analysis cut acceptances

To get the S1 of an event from its nuclear recoil energy E_R, a light yield for nuclear recoils was required. As there was no good anchor point for nuclear recoil energy (unlike in the case of γ-rays or $^{83\mathrm{m}}$Kr), there was no way to perform such a calibration in DS-50. Thus, a cross-calibration with the SCENE experiment was done, using their measurement of the scintillation efficiency of NRs with known energy relative to that of $^{83\mathrm{m}}$Kr ERs at zero drift field, $\mathcal{L}_{\mathrm{eff}}$ [67, 31]:

$$\mathrm{S1} = E_R \times \mathcal{L}_{\mathrm{eff}}(E_R) \times \mathrm{LY} \tag{9.10}$$

where $\mathrm{LY} = 8.03\,\mathrm{PE/keV}$ was the measured light yield of $^{83\mathrm{m}}$Kr in DS-50 with a $0\,\mathrm{V\,cm^{-1}}$ drift field [37].

With an event S1, the combined acceptance of our analysis cuts (Fig. 8.19) was applied. This was done by using the combined cut acceptance for events in that S1 bin (without applying the WIMP box) as a binomial probability for passing or failing the event.

S1 resolution was accounted for with a Poisson smearing[1], *i.e.*,

$$\mathrm{S1}_{\mathrm{smeared}} = \mathrm{Poisson}(\mathrm{Mean} = \mathrm{S1}) \tag{9.11}$$

F90 for the event was drawn from an analytic NR F90 model for the corresponding E_R bin, obtained from fits done on our ^{241}AmBe source calibration data [60].

With the event $\mathrm{S1}_{\mathrm{smeared}}$ and F90 constructed, and all other cut acceptances accounted for, the WIMP box simply had an acceptance of 1 for events that fell within it, and 0 for those that did not.

9.5 Obtaining a limit on the WIMP-nucleon scattering cross-section

For the chosen values of M_χ and σ_n, we thus had a prediction for the number of observed WIMP events after application of the analysis cuts. In particular, this was an inflated count because of the high σ_n assumed earlier.

To obtain an upper limit on σ_n in the event of a signal-free observation, we first interpret the observed count of zero WIMP events as being consistent (90% C.L.) with a Poisson distributed signal with mean <2.3. Then, since $\frac{dR}{dE_R} \propto \sigma_n$, we simply scale using Eqn. 9.1:

$$\sigma_{n\ \mathrm{UL}} = \frac{2.3}{\text{Count with } \sigma_n} \times \sigma_n \tag{9.12}$$

[1] It is perhaps more intuitive to perform the smearing of S1 first, before accounting for cut acceptance using $\mathrm{S1}_{\mathrm{smeared}}$. The sequence reported here is what was actually done for the blind analysis. Upon repeating the procedure with these steps reversed, we observed that their ordering did not have an impact on the final result.

Chapter 10

Results and conclusion

With the various background models determined to be in good shape, and an acceptable amount of predicted background in the WIMP search region, the 530d UAr data were fully opened. With the application of all analysis cuts (Ch. 4), no events were observed in the WIMP search region (Fig. 10.1). As mentioned in Sec. 9.5 this background- and signal- free result was consistent (90% C.L.) with a Poisson distributed WIMP signal with mean <2.3. The corresponding limit on the spin-independent WIMP-nucleon scattering cross-section for various WIMP masses is shown in Fig. 10.2. We were able to set a limit on the spin-independent WIMP-nucleon scattering cross-section of $1.1 \times 10^{-44}\,\mathrm{cm}^2$ ($3.8 \times 10^{-44}\,\mathrm{cm}^2$, $3.4 \times 10^{-43}\,\mathrm{cm}^2$) for a WIMP mass of $100\,\mathrm{GeV/c}^2$ ($1\,\mathrm{TeV/c}^2$, $10\,\mathrm{TeV/c}^2$) [43].

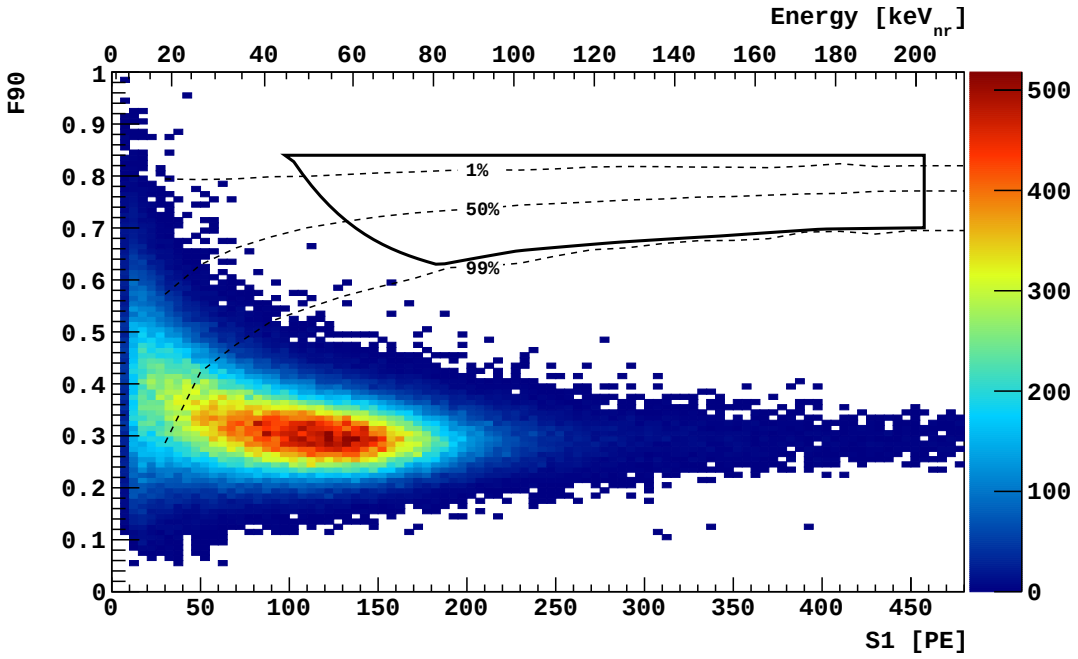

Figure 10.1: F90 *vs.* S1 of events in 530d UAr data, after application of all analysis cuts. The 1%, 50%, and 99% nuclear recoil acceptance contours, from fits to our ^{241}AmBe source calibration data, are also shown.

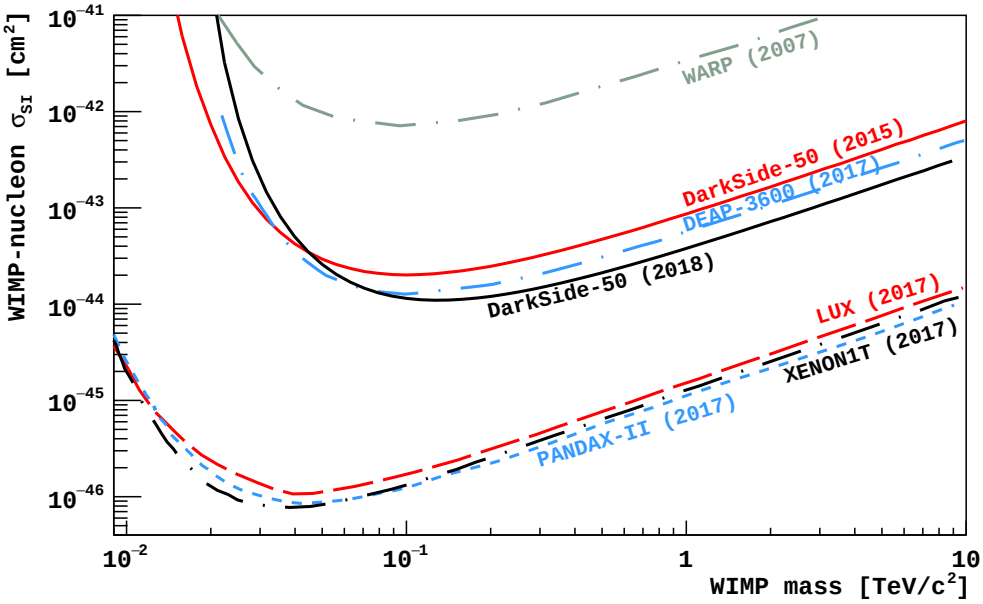

Figure 10.2: Limit on the spin-independent WIMP-nucleon scattering cross-section for various WIMP masses, based on the background- and signal- free result observed in the 530d UAr analysis.

Appendix A

Recoil energy and angle

We wish to relate the recoil energy E_R of the target nucleus (T) in the lab frame (L) to its recoil angle $\cos\theta$ in the center-of-mass (CM) frame:

$$E_R = \frac{1}{2} M_T v_L'^2 = \frac{1}{2} M_T (v_{Lx}'^2 + v_{Ly}'^2) \tag{A.1}$$

where M_T is the mass of the target nucleus, and v' is its recoil velocity with components denoted by x and y.

The target's recoil velocity in the CM frame is denoted by v'_{CM}, so

$$\begin{aligned} v'_{CMx} &= v'_{CM} \cos\theta \\ v'_{CMy} &= v'_{CM} \sin\theta \end{aligned} \tag{A.2}$$

In addition,

$$\begin{aligned} v'_{Lx} &= v'_{CMx} + V_{CM} \\ v'_{Ly} &= v'_{CMy} \end{aligned} \tag{A.3}$$

where the relative speed of the CM frame from the lab frame is

$$V_{CM} = \frac{M_\chi v_{L\chi}}{M_T + M_\chi} \tag{A.4}$$

where χ denotes variables relating to the dark matter particle. Substituting these into Eqn. A.1, we have

$$\begin{aligned} E_R &= \frac{1}{2} M_T [(V_{CM} + v'_{CM}\cos\theta)^2 + v'^2_{CM}\sin^2\theta] \\ &= \frac{1}{2} M_T (v'^2_{CM} + V^2_{CM} + 2v'_{CM} V_{CM}\cos\theta) \end{aligned} \tag{A.5}$$

Since there is no net momentum in the CM frame, $M^2_\chi v'^2_{CM\chi} = M^2_T v'^2_{CM}$, and

$$E_R = \frac{1}{2} M_T (\frac{M^2_\chi v'^2_{CM\chi}}{M^2_T} + V^2_{CM} + 2\frac{M_\chi v'_{CM\chi}}{M_T} V_{CM}\cos\theta) \tag{A.6}$$

Consider the kinetic energy in the CM frame:

$$\frac{1}{2} M_\chi v^2_{CM\chi} + \frac{1}{2} M_T v^2_{CM} = \frac{1}{2} M_\chi v'^2_{CM\chi} + \frac{1}{2} M_T v'^2_{CM} \tag{A.7}$$

Since

$$\begin{aligned} v_{L\chi} &= v_{CM\chi} + V_{CM} \\ &= v_{CM\chi} + \frac{M_\chi v_{L\chi}}{M_T + M_\chi} \\ \Rightarrow v_{CM\chi} &= \frac{M_T v_{L\chi}}{M_T + M_\chi} \end{aligned} \tag{A.8}$$

and

$$\begin{aligned} M_\chi v_{CM\chi} &= -M_T v_{CM} \\ \Rightarrow v_{CM} &= -\frac{M_\chi}{M_T} v_{CM\chi} \\ &= -\frac{M_\chi}{M_T}\frac{M_T v_{L\chi}}{M_T + M_\chi} \\ &= -\frac{M_\chi v_{L\chi}}{M_T + M_\chi} \end{aligned} \tag{A.9}$$

we have

$$\begin{aligned} \frac{1}{2}M_\chi \frac{M_T^2 v_{L\chi}^2}{(M_T + M_\chi)^2} + \frac{1}{2}M_T \frac{M_\chi^2 v_{L\chi}^2}{(M_T + M_\chi)^2} &= \frac{1}{2}M_\chi v'^2_{CM\chi} + \frac{1}{2}M_T \frac{M_\chi^2 v'^2_{CM\chi}}{M_T^2} \\ \frac{M_T M_\chi (M_T + M_\chi) v_{Lx}^2}{(M_T + M_\chi)^2} &= M_T M_\chi (\frac{1}{M_T} + \frac{M_\chi}{M_T^2}) v'^2_{CM\chi} \\ v'^2_{CM\chi} &= \frac{M_T^2 v_{Lx}^2}{(M_T + M_\chi)^2} \end{aligned} \tag{A.10}$$

and so

$$\begin{aligned} E_R &= \frac{1}{2}M_T (\frac{M_\chi^2 v_{L\chi}^2}{(M_T + M_\chi)^2} + \frac{M_\chi^2 v_{L\chi}^2}{(M_T + M_\chi)^2} + 2\frac{M_\chi v_{L\chi}}{M_T + M_\chi}\frac{M_\chi v_{L\chi}}{M_T + M_\chi}\cos\theta) \\ &= \frac{2E M_T M_\chi}{(M_T + M_\chi)^2}(1 + \cos\theta) \end{aligned} \tag{A.11}$$

where $E = M_\chi v_{L\chi}^2/2$ is the WIMP's kinetic energy in the lab frame. Thus,

$$\frac{d\cos\theta}{dE_R} = \frac{(M_T + M\chi)^2}{2E M_T M_\chi} \tag{A.12}$$

For any recoil energy, the kinetic energy of the incoming WIMP is minimized when $\theta = 0$ ($\cos\theta = 1$), *i.e.*,

$$E_{\min} = \frac{E_R (M_T + M_\chi)^2}{4 M_T M_\chi} \tag{A.13}$$

$$v_{\min} = \sqrt{\frac{E_R (M_T + M_\chi)^2}{2 M_T M_\chi^2}} \tag{A.14}$$

Bibliography

[1] J. H. Oort, *The force exerted by the stellar system in the direction perpendicular to the galactic plane and some related problems*, Bull. Astron. Inst. Netherlands **6**, 249 (1932).

[2] F. Zwicky, *Republication of: The redshift of extragalactic nebulae*, General Relativity and Gravitation **41**, 207 (2009).

[3] V. C. Rubin, N. Thonnard, and W. K. Ford, Jr., *Extended rotation curves of high-luminosity spiral galaxies. IV - Systematic dynamical properties, SA through SC*, Astrophysical Journal **225**, L107 (1978).

[4] K. G. Begeman, A. H. Broeils, and R. H. Sanders, *Extended rotation curves of spiral galaxies - Dark haloes and modified dynamics*, Monthly Notices of the Royal Astronomical Society **249**, 523 (1991).

[5] D. Walsh, R. F. Carswell, and R. J. Weymann, *0957 + 561 A, B: Twin quasistellar objects or gravitational lens*, Nature **279**, 381 (1979).

[6] R. Lynds and V. Petrosian, *Luminous arcs in clusters of galaxies*, Astrophysical Journal **336**, 1 (1989).

[7] D. Clowe et al., *A Direct Empirical Proof of the Existence of Dark Matter*, Ap. J. **648**, L109 (2006).

[8] Planck Collaboration et al. (The Planck Collaboration), *Planck 2015 results. XIII. Cosmological parameters*, Astro. & Ap. **594**, A13 (2016).

[9] G. B. Gelmini, *The Hunt for Dark Matter*, Presentation at TASI 2014 (2014).

[10] J. M. Gaskins, *A review of indirect searches for particle dark matter*, Contemporary Physics **0**, 1 (2016).

[11] M. G. Aartsen et al., *Search for annihilating dark matter in the Sun with 3 years of IceCube data*, Contemporary Physics **C77**, 146 (2007).

[12] F. Kahlhoefer, *Review of LHC dark matter searches*, Int. J. Mod. Phys. A **32**, 1730006 (2017).

[13] R. Bernabei et al. (The DAMA/LIBRA Collaboration), *DAMA/LIBRA results and perspectives*, EPJ Web Conf. **136**, 05001 (2017).

[14] R. Agnese et al., *Results from the Super Cryogenic Dark Matter Search Experiment at Soudan*, Phys. Rev. Lett. **120**, 061802 (2018).

[15] A. Aguilar-Arevalo et al. (The DAMIC Collaboration), *Search for low-mass WIMPs in a 0.6 kg day exposure of the DAMIC experiment at SNOLAB*, Phys. Rev. D **94**, 082006 (2016).

[16] D. S. Akerib et al. (The LUX Collaboration), *Results from a Search for Dark Matter in the Complete LUX Exposure*, Phys. Rev. Lett. **118**, 021303 (2017).

[17] E. Aprile et al. (The XENON Collaboration), *First Dark Matter Search Results from the XENON1T Experiment*, Phys. Rev. Lett. **119**, 181301 (2017).

[18] X. Cui et al. (The PandaX-II Collaboration), *Dark Matter Results From 54-Ton-Day Exposure of PandaX-II Experiment*, arXiv:1708.06917v2 (2017).

[19] P. A. Amaudruz et al. (The DEAP-3600 Collaboration), *First results from the DEAP-3600 dark matter search with argon at SNOLAB*, arXiv:1707.08042v2 (2017).

[20] P. Agnes et al. (The DarkSide Collaboration), *Results from the first use of low radioactivity argon in a dark matter search*, Phys. Rev. D **93**, 081101 (2016).

[21] B. Loer, *Towards a Depleted Argon Time Projection Chamber WIMP Search : DarkSide Prototype Analysis and Predicted Sensitivity*, Ph.D. thesis, Princeton University (2011).

[22] D. S. Akerib et al. (The LUX Collaboration), *Limits on spin-dependent WIMP-nucleon cross section obtained from the complete LUX exposure*, arXiv:1705.03380v1 (2017).

[23] P. Agnes et al. (The DarkSide Collaboration), *First results from the DarkSide-50 dark matter experiment at Laboratori Nazionali del Gran Sasso*, Phys. Lett. B **743**, 456 (2015).

[24] P. Agnes et al. (The DarkSide collaboration), *The veto system of the DarkSide-50 experiment*, JINST **11**, P03016 (2016).

[25] S. Westerdale, *A study of nuclear recoil backgrounds in dark matter detectors*, Ph.D. thesis, Princeton University (2016).

[26] P. Agnes et al. (The DarkSide Collaboration), *The electronics, trigger and data acquisition system for the liquid argon time projection chamber of the DarkSide-50 search for dark matter*, JINST **12**, P12011 (2017).

[27] V. M. Gehman et al., *Fluorescence efficiency and visible re-emission spectrum of tetraphenyl butadiene films at extreme ultraviolet wavelengths*, Nucl. Inst. Meth. A **654**, 116 (2011).

[28] D. Mei, Z. B. Yin, L. C. Stonehill, and A. Hime, *A model of nuclear recoil scintillation efficiency in noble liquids*, Astropart. Phys. **30**, 12 (2008).

[29] A. Hitachi et al., *Effect of ionization density on the time dependence of luminescence from liquid argon and xenon*, Phys. Rev. B **27**, 5279 (1983).

[30] T. Doke et al., *Absolute Scintillation Yields in Liquid Argon and Xenon for Various Particles*, Jpn. J. Appl. Phys. **41**, 1538 (2002).

[31] H. Cao et al. (The SCENE Collaboration), *Measurement of scintillation and ionization yield and scintillation pulse shape from nuclear recoils in liquid argon*, Phys. Rev. D **91**, 092007 (2015).

[32] J. Brodsky, *xy position reconstruction in DarkSide-50*, Ph.D. thesis, Princeton University (2015).

[33] A. Watson, *Transverse Position Reconstruction in a Liquid Argon Time Projection Chamber using Principal Component Analysis and Multi-Dimensional Fitting*, Ph.D. thesis, Temple University (2017).

[34] A. Fan, *Results from the darkside-50 dark matter experiment*, Ph.D. thesis, University of California Los Angeles (2016).

[35] L. W. Kastens, S. B. Cahn, A. Manzur, and D. N. McKinsey, *Calibration of a liquid xenon detector with* $^{83}Kr^{m}$, Phys. Rev. C **80**, 045809 (2009).

[36] N. Canci, *DarkSide-50 Operation Summary, DS Winter General Meeting* (2017), docDB 1714.

[37] P. Meyers, *Light yield value and stability in 540-d analysis* (2018), docdb 2508.

[38] P. Agnes et al. (The DarkSide Collaboration), *CALIS—A CALibration Insertion System for the DarkSide-50 dark matter search experiment*, JINST **12**, T12004 (2017).

[39] B. R. Hackett, *The DarkSide-50 Experiment: Electron Recoil Calibrations and A Global Energy Variable*, Ph.D. thesis, University of Hawaii at Mānoa (2017).

[40] L. Pagani, *Direct dark matter detection with the darkside-50 experiment*, Ph.D. thesis, University of Genoa (2017).

[41] R. Acciarri et al. (The WArP Collaboration), *Oxygen contamination in liquid Argon: combined effects on ionization electron charge and scintillation light*, JINST **5**, P05003 (2010).

[42] C. Stanford, *Alphas and Surface Backgrounds in Liquid Argon Dark Matter Detectors*, Ph.D. thesis, Princeton University (2017).

[43] P. Agnes et al. (The DarkSide Collaboration), *DarkSide-50 532-day Dark Matter Search with Low-Radioactivity Argon*, arXiv:1802.07198v1 (2018).

[44] National Nuclear Data Center, *Information extracted from the Chart of Nuclides database* (2018).

[45] United Nations Scientific Committee on the Effects of Atomic Radiation (UNSCEAR), *Sources and effects of ionizing radiation*, UNSCEAR 2000 Report to the General Assembly **1** (2000).

[46] D. Acosta-Kane et al., *Discovery of underground argon with low level of radioactive ^{39}Ar and possible applications to WIMP dark matter detectors*, Nucl. Inst. Meth. A **587**, 46 (2008).

[47] H. O. Back et al., *Depleted Argon from Underground Sources*, Phys. Procedia **37**, 1105 (2012).

[48] P. Benetti et al. (The WArP Collaboration), *Measurement of the specific activity of ^{39}Ar in natural argon*, Nucl. Inst. Meth. A **574**, 83 (2007).

[49] P. Meyers, *Why do we think the PMT radioactivity is in the stem? And is it?* (2017), docDB 2231.

[50] P. Agnes et al., *Electroluminescence pulse shape and electron diffusion in liquid argon measured in a dual-phase TPC*, Submitted to: Nucl. Instrum. Meth. A:1802.01427 (2018).

[51] A. Empl and E. V. Hungerford, *A FLUKA Study of β-delayed Neutron Emission for the Ton-size DarkSide Dark Matter Detector*, arXiv:1407.6628v2 (2014).

[52] A. Monte, *S1-Only + S2-Only Pileup Background* (2017), docDB 2105.

[53] T. Johnson, *Negative Log Likelihood S1 Pattern Rejector* (2017), docDB 2105.

[54] P. Agnes et al. (The DarkSide Collaboration), *Simulation of argon response and light detection in the DarkSide-50 dual phase TPC*, JINST **12**, P10015 (2017).

[55] M. Berger, J. Coursey, M. Zucker, and J. Chang, *ESTAR, PSTAR, and ASTAR: Computer Programs for Calculating Stopping-Power and Range Tables for Electrons, Protons, and Helium Ions (version 2.0.1)* (2018).

[56] M. Szydagis et al., *NEST: a comprehensive model for scintillation yield in liquid xenon*, JINST **6**, P10002 (2011).

[57] P. Agnes, *Direct search for dark matter with the darkside experiment*, Ph.D. thesis, Université Paris Diderot (2016).

[58] M. Wada, *Kr campaign summary* (2016), docDB 1505.

[59] R. Fitzpatrick, *Toward an energy model for electronic recoils in DarkSide-50*, Senior thesis, Princeton University (2016).

[60] E. E. Ludert, *Detailed characterization of nuclear recoil pulse shape discrimination in the darkside-50 direct dark matter experiment*, Ph.D. thesis, University of Hawaii at Mānoa (2017).

[61] A. Empl, E. V. Hungerford, R. Jasim, and P. Mosteiro, *A Fluka study of underground cosmogenic neutron production*, JCAP **1408**, 064 (2014).

[62] G. J. Feldman and R. D. Cousins, *Unified approach to the classical statistical analysis of small signals*, Phys. Rev. D **57**, 3873 (1998).

[63] J. D. Lewin and P. F. Smith, *Review of mathematics, numerical factors, and corrections for dark matter experiments based on elastic nuclear recoil*, Astropart. Phys. **6**, 87 (1996).

[64] C. Savage, K. Freese, and P. Gondolo, *Annual Modulation of Dark Matter in the Presence of Streams*, Phys. Rev. D **74**, 043531 (2006).

[65] C. Savage, G. Gelmini, P. Gondolo, and K. Freese, *Compatibility of DAMA/LIBRA dark matter detection with other searches*, JCAP **2009**, 010 (2009).

[66] M. C. Smith et al., *The RAVE survey: constraining the local Galactic escape speed*, Month. Not. Royal Astron. Soc. **379**, 755 (2007).

[67] H. Cao, *A study of nuclear recoils in liquid argon time projection chamber for the direct detection of wimp dark matter*, Ph.D. thesis, Princeton University (2014).